

A new vibrational technique for measurement of stress variations in thin films

A thesis submitted

by

Sreten Askraba B.Sc.(Elec. Eng.)

for the degree of

Doctor of Philosophy



Optical Technology Research Laboratory
School of Communications and Informatics
Victoria University
Melbourne
May, 1999

FTS THESIS

530.4275 ASK

30001005536844

Askraba, Sreten

A new vibrational technique
for measurement of stress
variations in thin films

This PhD thesis is dedicated to my parents

Declaration

I, **Sreten Askraba**, declare that the thesis titled,

“A new vibrational technique for measurement of stress variations in thin films”

is my own work and has not been submitted previously, in whole or in part, in respect of any other academic award.

Sreten Askraba



dated the 17th May, 1999

Acknowledgments

There are a number of people to whom I wish to thank for assistance throughout my PhD study. Firstly I would like to thank my PhD supervisor Professor David Booth for giving me the opportunity and having confidence in my ability, his guidance, invaluable advice and assistance given throughout my course of study.

I am very grateful to Dr Tranxuan Danh from Department of Mechanical Engineering, Victoria University, for helpful assistance in using ANSYS 5.3 Finite Element Modeling software. I would like to thank my fellow post-graduate students for their friendship and help when it was required.

Without the help of the technical staff my project would have not been a success. Therefore I would like to thank Mr. Alex Shelamoff for his assistance with the design of electronic detection circuit. From the mechanical workshop I would like to thank Mr. Mark Kivienen, and Mr. Donald Ermel for their helpful consultation, designing and construction of necessary parts for the vacuum system. In addition I would like to thank all the other academic, technical and administrative staff from the Department of Applied Physics, Victoria University.

Abstract

A survey of thin films deposited by standard techniques (electrodeposition, chemical deposition, sputtering, physical deposition, *etc.*) shows that internal stress is a common problem, particularly in industrial applications. The presence of stress influences the properties of the film and when severe may cause the film to buckle or crack. There is a significant technological and industrial interest in measurements that determine the magnitude of the internal stress. Stress measurement represents a highly sensitive tool for the study of thin film structure in a non-destructive manner.

Accurate measurements of the internal stress in thin films is rather difficult and a number of methods have been described in the literature. This thesis describes a simple all-optical technique for measurement of internal stress in thin films deposited in a vacuum system. The technique is based on a measurement of changes in the modal resonant vibrational frequencies of the substrate/film structure which are caused by stress-induced changes in curvature. The modal vibrations are induced by photothermoelastic bending produced using low-power modulated laser diode light. The vibrational resonant frequency changes are monitored by a sensitive fibre optic interferometer system. A feedback system can allow direct readout of stress-related frequency variations with time as films are deposited or

modified by processes such as exposure to the atmosphere. The technique provides very sensitive measurements of the substantial changes in resonant frequency with fractional errors of one part in 10^4 possible with high-Q resonances and constant temperatures. The technique was tested using chromium and magnesium fluoride thin films deposited on glass substrates.

Table of Contents

	Page
DECLARATION	iii
ACKNOWLEDGMENTS	iv
ABSTRACT	v
TABLE OF CONTENTS	vii
 CHAPTER 1. Introduction	
1.1 Introduction	1-1
1.2 Scope of the thesis	1-4
1.3 Preview of the thesis	1-5
 CHAPTER 2. General overview of the previous work on stress in thin films	
2.1 Introduction	2-1
2.2 The nucleation and growth of thin films	2-2
2.2.1 Thermodynamical consideration	2-2
2.2.2 The role of kinetic parameters on thin film growth ...	2-4
2.3 Structure and properties of thin films	2-5
2.4 Definition of residual stress	2-8

2.5	Experimental methods for measuring the stress in thin films	2-13
	2.5.1 Circular membranes and bending plate methods	2-14
	2.5.2 Bending-beam methods	2-18
	2.5.3 Electron-diffraction and X-ray method	2-20
	2.5.4 Other techniques	2-20
2.6	Vibrations of thin plates and shells	2-22
	2.6.1 Mechanical vibrations of circular plates	2-23
	2.6.2 Vibrations of shallow spherical shells	2-24
2.7	Summary	2-26

**CHAPTER 3. Theoretical basis of the technique for stress determination
in thin films**

3.1	Introduction	3-1
3.2	The general solution for vibration of uniform thin flat plates	3-3
3.3	Symmetrical oscillations of a circular plate clamped at the center	3-5
3.4	3D plots of solution for circular plate clamped at the center	3-12
3.5	Calculated and measured resonant mechanical vibration of substrate used for stress measurement in thin films	3-12
3.6	Mechanical vibrations of shallow spherical shells	3-19
3.7	Stress and strain relationships	3-24
	3.7.1 Definition of stress and types of stress	3-24
	3.7.2 Definition of strain	3-27
	3.7.3 Elastic stress-strain relations	3-29

3.8	Relationship between stress in thin films and substrate deflection	3-30
	3.8.1 Determination of the stress in thin films.....	3-32
	3.8.2 Relationship between the stress in a film and measured resonant frequency of the curved substrate/film combination	3-39
3.8.3	The effect of the coating material on resonant vibration frequencies of a flat glass/film composite structure	3-40
3.9	Summary	3-43

CHAPTER 4. Experimental methods

4.1	Introduction	4-1
4.2	Coating thin films	4-2
	4.2.1 Description of vacuum system	4-3
	4.2.2 Chamber cleaning techniques	4-6
4.3	Sample preparation	4-7
	4.3.1 Cleaning of substrate surface	4-7
	4.3.2 The evaporants	4-9
	4.3.3 Actual coating procedure	4-10
4.4	Curvature measurement	4-11
4.5	Calibration of the film thickness monitor	4-13
4.6	Modal resonant vibrational frequency measurements of the substrate/film system	4-16
	4.6.1 Homodyne optical fibre interferometric sensors	4-19

4.6.2	Practical description of the interferometric sensor	4-28
	a) Optical layout	4-28
	b).Detector and feedback circuitry	4-32
	c) Calibration of the interferometer	4-33
4.7	Physical principle of the photothermal excitation mechanism	4-35
4.8	Description of modified vacuum system	4-37
4.9	Summary	4-39

CHAPTER 5. Experimental results and discussion

5.1	Introduction	5-1
5.2	Auger Nanoprobe Analysis and depth profiles	5-3
5.3	Initial results with chromium films (measured in air)	5-6
5.4	Measurements of stress when the rear surface of the sample was coated with a thin titanium film	5-13
5.5	Experimental results for <i>in situ</i> measurements	5-19
5.6	Summary	5-33

CHAPTER 6. Conclusion

6.1	Conclusion	6-1
6.2	Future work	6-4

REFERENCES

APPENDICES

A.1	Technical data for the glass substrate used in experiments	A-2
A.2	Spectrographic analysis of the evaporants according to the manufacturer specification.	A-3
A.3	List of figures	A-5
A.4	List of tables	A-10
A.5	List of symbols used in this thesis	A-12

PUBLICATIONS

1.1 Introduction

Thin films of many different materials (metals, semiconductors, inorganic and dielectric materials) are used in an extremely wide range of modern technological applications. Such applications include dielectric and metallic coating of components for laser and other optical systems, thin films of semiconductor and other materials for the production of electronic components and VLSI chips and decorative and protective coating on a wide range of items. These films frequently have high intrinsic mechanical stress and the presence of this stress influences the mechanical, optical, electro-transport, magnetic and superconductive properties of thin films (Bromley *et al.*, 1983; Leusink *et al.*, 1992; Beck *et al.*, 1998). In extreme cases, such stress can even result in failure of the thin film by cracking or by delamination from its substrate. This failure can be immediate or, more seriously, delayed. Thus there is significant technological interest in measurements that determine the magnitude of the internal stress during or at the end of deposition process. Stress measurements prove to be a highly sensitive tool for the study of morphology and growth mode of thin films in a non-destructive manner (Winau *et al.*, 1992; Malhotra *et al.*, 1997). Such investigations may eventually lead to a better

understanding of the mechanical stress in the film and consequently increase the reliability of thin film applications (Aberman, 1990; Kylner and Mattsson, 1997). These investigations are interesting scientifically, since measurements of stress in thin film should lead to information about which deposition parameters primarily influence thin film properties. Accurate measurement of the stress in thin films is rather difficult and a number of methods have been devised (Maissel and Glang, 1970; Vandrienuizen *et al.*, 1993; Martin *et al.*, 1998). The present work is concerned with the development of a new sensitive technique for indirect measurement of stress variations in thin films which involves the remote measurement of modal vibrational frequencies when the sample is excited thermoelastically.

When modulated laser light of appropriate power density illuminates the sample, the absorbed energy is converted to heat through a non-ablative process (Opsal and Rosencwaig 1982). Thermoelastic bending (the drum effect) produced by transient thermal expansion of the irradiated area causes mechanical vibrations of the sample (Charpentier and Lepoutre 1982; Crosbie *et al.*, 1986). This thermal bending process can be produced using low-power modulated laser diode light. When combined with remote fibre optic vibration sensing, an integrated optical system can be produced for excitation and measurement of the changes in modal vibration frequencies of the substrate/film structure. Such measurements can be easily automated and used routinely in industrial laboratories for determination of stress changes in thin films. This work reports the first use of an all-optical technique based

on an optical fibre interferometer for such an application. The optical fibre interferometer offers considerable advantages in ease of use and robustness compared to existing methods for stress measurements in thin films. It uses light scattered from the rear surface of the target structure (not necessary highly reflective) and coupled back into the fibre to produce interference with the reference beam. In such an arrangement there is no need for bulky and difficult-to-align mirror systems in the interferometer as in the case in a conventional bulk optic device. However the use of a fibre interferometer can offer challenging detection problems due to the reduced signal-to-noise ratios which accompany the reduced light intensities in the interfering beams. These reduced intensities are due to losses in coupling into and out of the optical fibres both from the laser source and the beam scattered from the target. In this work it is shown that with careful design of the fibre interferometer, excellent signal-to-noise ratios can be obtained using the scattered light from a thin Ti film applied to the rear surface of the target.

The indirect method for stress determination in thin films, described in this thesis, relies on measuring the variation of transverse modal vibrational frequencies of a thin circular substrate on which the thin film is deposited. These frequencies are a very sensitive function of the curvature of the substrate which is a function of the stress at the film/substrate boundary. The method was initially developed using coated substrates which were removed from a vacuum deposition system in order to perform measurements of vibration frequency and curvature. For real-time measurements under controlled conditions inside the vacuum system the previous technique was easily adapted as it only required two optical fibre

feedthroughs into the vacuum chamber. A totally remote system for exciting the vibrational resonances of the substrate/coating and for measuring the resonant frequency was used. The excitation is via square-wave-modulated low power laser diode light which is delivered to the substrate in the vacuum chamber via an optical fibre. The vibration sensing system uses a fibre optic interferometer which requires only one sensing fibre to be passed through a feedthrough into the coating region. Using feedback from the interferometer to the laser diode drive electronics, one can lock the system to track the resonance and obtain a direct readout of stress-related resonant frequency variations with time as films are deposited or modified by processes such as exposure to the atmosphere. The technique provides very sensitive measurements of the substantial changes in resonant frequency with standard errors of one part in 10^4 possible with high-Q resonances and constant temperatures.

1.2 Scope of the thesis

This thesis aims to describe the development and evaluation of a new optical technique for accurate non-contact measurements of residual stress-dependent modal frequency shifts in thin films coated onto thin glass substrates that could be easily automated and used routinely in industrial laboratories. This involves:

- (i) The design, construction and characterisation of a laser-diode-based system for producing thermoelastically-induced mechanical vibrations in

substrates and a two beam fibre optic interferometer which can remotely detect these vibrations.

- (ii) Derivation of analytical expressions for the relationship between modal resonant frequencies and curvature/stress which are appropriate to the geometry chosen for the experimental measurements.
- (iii) Modification and adaptation of a vacuum deposition system to allow it to be used to test the stress measurement technique.
- (iv) Assessment of the effectiveness of the new optically-excited vibrational resonance technique for stress measurement using metallic and dielectric films.

1.3 Preview of the thesis

Chapter 2 introduces the concept of stress in thin films and gives an overview of previous methods for making measurements of residual stress. Since the stress measurement method developed in this thesis relies on changes in mechanical resonances of thin plates and shells, this chapter also introduces the essential features of vibrations in these structures.

Chapter 3 presents a detailed derivation of the modal resonant frequencies of a uniform flat circular plate supported at the centre. This derivation is included as no such treatment covering all modes with these boundary conditions is to be found in the literature. The modal resonant frequencies predicted by these expressions are then compared to those deduced from finite element analysis and measurements made with experimental substrates which have been coated only with very thin films on front and rear surfaces (just enough to be able to use the excitation and measurement methods developed in this work). The theoretical results obtained for a flat plate are then extended to cover the case of a thin spherical shell – the shape assumed by a substrate which bends under the influence of stress. Chapter 3 also includes a discussion of the stress and strain relationships as they apply to the substrate/film structures which are studied in this thesis. Equations are derived for curvature of the substrate as a function of film stress and these equations are combined with equations for resonant frequency as a function of spherical shell curvature to obtain expressions which relate both curvature and stress to resonant frequency. These equations form the basis for analysis of the experimentally-measured modal frequency shifts in terms of stress and curvature. The final section of this chapter discusses the effect of the thickness variations and changes of other physical properties as a result of coating (without any stress) on the resonant frequencies of the structure.

Chapter 4 contains a description of the experimental arrangements and equipment in sufficient detail for one to properly interpret the experimental results presented in Chapter 5. Chapter 4 includes details of the vacuum evaporation system

and techniques used for sample preparation and coating. It also includes a detailed description of the optical equipment used for photothermoelastic excitation of the samples and particularly the interferometer used for resonant frequency measurement. The discussion of the interferometer includes sufficient theory to understand its operation as well as techniques used for calibration, locking the interferometer at the quadrature point and determination of noise limitations on measurement sensitivity.

Chapter 5 presents results of measurement made using the new technique with metallic (Cr) and dielectric (MgF_2) films. These results clearly demonstrate that the technique is effective and show that the stress-induced frequency shifts which arise with these films are substantial. Experimental results are presented for measurements made in the atmosphere after coatings have been applied in vacuum and for *in-situ* measurements made inside the vacuum system including measurements made while coating is in progress. The effect of temperature changes during coating is also investigated as is the effect on film stress of exposure of coatings to the atmosphere.

Chapter 6 is a conclusion chapter which summarises the major achievements of the work described in this thesis and the advantages of the new technique for indirect stress determination in thin films. This chapter also make some brief observations about future extensions of this work and practical applications.

General overview of the previous work on stress in thin films

2.1 Introduction

In this chapter a brief description of structure and properties of thin films will be presented and the intrinsic stress in a film will be defined. Then an overview of previous methods of measuring the stress in thin films will be given. As the technique for stress measurements in thin films described in this work is based on a measurement of the modal resonant vibrational frequencies of thin plates and shells, a brief introduction of dynamics of these structures will also be given.

2.2 The nucleation and growth of thin films

The growth of thin films has studied intensively in the past by employing the entire spectrum of experimental tools ranging from transmission, scanning and low -energy electron microscopy (Pashley and Stowell, 1966; Venables *et al.*, 1980), reflection high-, medium- and spot profile analysis low-energy electron diffraction (Egelhoff and Jacob, 1989; Schneider *et al.*, 1990), Auger electron spectroscopy (Bauer and Popa, 1984), scanning tunnelling microscopy (Neddermeyer, 1990). In addition, advanced theoretical film growth simulations were performed with high-speed supercomputer systems (Gilmore and Sprague, 1991; Luedtke and Landman, 1991). It appears, however, that despite these efforts the all processes involved are not completely understood (Koch, 1994). In this section a short summary of the present knowledge on nucleation and growth of thin films will be presented.

2.2.1 Thermodynamical consideration

A decisive period of film growth is the nucleation stage at the very beginning of the film deposition. Thermodynamical theory is applicable only to macroscopic systems and it may provide useful first insights of the film growth. For the initially formed nuclei the ratio between the number of surface and/or interface atoms and the atoms of the bulk is high and their equilibrium shape will depend on the magnitude of

the respective free surface and interface energies. The size of equilibrium nuclei (equilibrium polyhedron) can be calculated from the equation (Koch, 1994):

$$\frac{\Phi_i}{h_i} = \frac{\Phi^* - \Phi_B}{h_{AB}} = \frac{\Phi_A - \beta}{h_{AB}} = \frac{\Delta\mu}{2\vartheta} = \frac{kT}{2\vartheta} \ln \frac{P}{P_\infty}, \quad (2.1)$$

where Φ_i is free surface energy, $\Delta\mu$ is chemical potential, k is Boltzmann's constant, T is substrate temperature, v is the volume of a single film atom, P and P_∞ are the respective vapour pressures of the nuclei and the bulk phase. As illustrated in Figure 2.1 the interface is created between surface A of the nuclei and substrate surface B. The specific free interface energy Φ^* is then calculated as $\Phi^* = \Phi_A + \Phi_B - \beta$ with β being the corresponding free energy of adhesion which is realised when the surfaces A and B are brought into contact. As pointed out by Koch (1994) Φ^* is assumed to be independent of the size and shape of the interface.

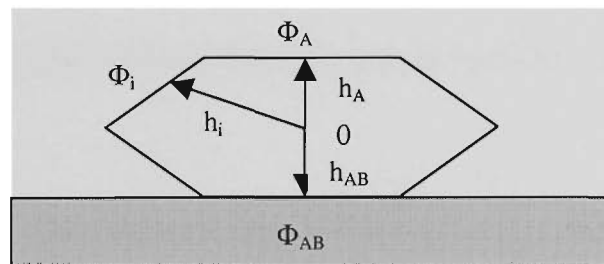


Figure 2.1 The equilibrium shape of a deposit A on a substrate B; Φ_i and h_i are the free surface energies and central distance of the crystal facets i formed at equilibrium; Φ_{AB} and h_{AB} are the free surface energies of the deposit and substrate and central distance of the crystal facets of the interface AB.

The equation 2.1 shows that three-dimensional shape of the initial formed nuclei is determined by the central distance of the interface h_{AB} which in turn is

determined by the relative magnitude of the free energy of adhesion β with respect to the free energy of the crystal nuclei Φ_A which forms the top of equilibrium nuclei.

Unfortunately two major obstacles are encountered upon applying thermodynamical theory to real film/substrate systems:

- a) There is a lack of experimental data on the free surface and interface energies for the numerous possible combinations of thin film and substrate surfaces so that the predictational value of thermodynamics for the growth of thin films remains unsatisfied.
- b) Usually film growth does not proceed in thermodynamical equilibrium but it is controlled by kinetic parameters as well.

2.2.2 The role of kinetic parameters on thin film growth

The thermodynamical theory for thin film growth relies on the assumption of a homogeneous substrate surface which is characterised by an uniform Φ^* over a large distance. In practice such a surface is hardly ever available. Real substrate surfaces usually exhibit many different defects such as vacancies, ad-atoms, stacking faults, dislocations and impurity atoms or molecules which have either diffused out of the bulk or absorbed from the residual gas in vacuum chamber. As a consequence of the inhomogeneous Φ^* , nuclei of various equilibrium shapes are formed at the initial stages of film growth. The presence of defects on surfaces may have substantial influence on the nucleation rate leading to a drastically increased

density of nuclei (Shimaoka and Komoriya, 1970). In addition, defects usually affect strongly diffusion controlled processes of the growing film.

The second parameter that counteracts the influence of defects on the kinetics of film growth is the substrate temperature which determines the thermal energy of the diffusing atoms. It was shown (Koch, 1994) that the influence of certain type of defect is overcome when the substrate temperature is raised. The influence of deposition parameters on structure and properties of thin films is discussed in the following sections.

2.3 Structure and properties of thin films

The properties and structure of thin films are strongly affected by its composition and thickness. The behavior of the film is also affected by the substrate type, deposition parameters, density of the film and any chemical reactions at the substrate/film interface.

The substrate type influences the microstructure of the thin film. Amorphous substrates such as glasses often contain surface irregularities which can lead to a non-uniform distribution and orientation of deposited crystallites. For a film to adhere well it is important that the substrate surface is clean. Good adhesion to glass substrates is obtained with chemically reactive metals such as chromium or aluminum (Thun, 1964). Coatings involving atoms of noble metals are usually

weakly bonded to a glass surface and hence thick films of such metal are relatively easily stripped from the substrate.

Deposition parameters also affect the properties of thin films. The three most important deposition parameters are vacuum pressure, deposition rate and substrate temperature. The presence of residual gases in the vacuum chamber can result in structural modifications to the film. Gas trapping tends to result in films with a highly disordered microstructure. Absorbed gas atoms lead to a decrease of surface mobility and smaller grain size of the film. The deposition of a thin film with a 'bulk' structure generally requires a vacuum better than 10^{-5} Pa.

Atomic surface mobility is a function of surface temperature (Neugebauer, 1964), therefore the substrate temperature has a strong influence on adhesion and the structure of thin films. At low substrate temperatures, the resulting film structure depends on the interatomic bond character of the film and substrate material. With increasing substrate temperature the size of the crystallites increases and the number of lattice dislocations decreases.

At very low rates of deposition the resulting thin films exhibit roughness and relatively porous packing (Hoffman, 1966; Tanaka, *et al.*, 1998). With higher rates the film density increases and roughness decreases. The average crystal size also decreases while the density of lattice faults in the crystallographic film structure increases as there is less time available for atomic rearrangement during deposition. For example, a 100 nm thick chromium films deposited on a substrate at a

temperature of 340°C, had an average grain diameter of about 250 Å at deposition rates below 20 Å/sec. With a deposition rate of 40 Å/sec the average grain diameter is about 150 Å at the same substrate temperature (Neugebauer, 1959).

Thin films usually exhibit the same crystallographic structure as the bulk material. However, deviations from the properties of the bulk materials can be caused by small film thickness, large surface to volume ratios and high structural disorder. Small film thickness affects the electric, magnetic and mechanical properties. The high surface-to-volume ratio of a film increases the influence of gas adsorption, diffusion and chemical reactions at the film surface or film-substrate interface. High structural disorder of materials (for instance amorphous structure) can lead to mechanical, electrical and magnetic properties which differ from those in bulk crystals by orders of magnitude (Hoffman, 1966; Vinci and Vlassak, 1996). Annealing has often been used to improve the structure and properties of thin films (Sinha *et al.*, 1978; Flinn, 1989; Scardi, *et al.*, 1994).

Increasing interest in fundamental solid state physics and many areas of technology including the semiconductor, optics, decorative and protective coating industries require better understanding of the influence of the deposition parameters on one hand and on the correlation between structure and physical film properties on the other.

2.4 Definition of residual stress

When a body is constrained, a system of forces applied to the body will in general produce a change in its dimensions. The fractional change in dimension is called the strain. The force per unit area required to produce the strain is called the stress. Stresses in real materials may be external or internal. When a metal bar is extended by a force the applied stress is external. When the same metal bar is heated it becomes stressed internally.

The residual stress (or lock-up stress, internal stress) in a mechanical system is the stress that is locked into a part or assembly even though the part or assembly is free from external forces or thermal gradients. It is important to consider this stress in design and failure analysis.

A model for the generation of residual stress during deposition of films is illustrated schematically in Figure 2.1. Regardless of the stress distribution (isotropic or anisotropic), mechanical equilibrium requires that the net force F and bending moment M vanish on the film-substrate boundary. For a cross section of the film/substrate combination in equilibrium,

$$F = \int \sigma dA = 0 \quad \text{and} \quad (2.2)$$

$$M = \int \sigma z dA = 0. \quad (2.3)$$

Here σ is residual stress, dA is the element of cross-sectional area and z is the distance from the chosen neutral axis as shown in Figure 3.10(c). These basic equations will be used in deriving the formula for stress in thin films (section 3.8).

In the first type of behaviour shown schematically in Figure 2.1(a), the growing film initially shrinks relative to a substrate. Surface tension forces and misfit of atomic spacing could be the reasons why this might happen. However, both the film and substrate must have the same length and the film stretches while the substrate contracts. Therefore, the tensile forces developed in the film are balanced by the compressive forces in the substrate. The film/substrate system is still not in mechanical equilibrium because of the uncompensated end moments. If the substrate is not rigidly held it will elastically deform to counteract the unbalanced moments. Thus, thin films with tensile residual stresses bend the substrate concavely. In an entirely similar fashion a film which develops residual compressive stresses will contract relative to substrates, as shown in Figure 2.1(b). Therefore, residual compressive film stresses bend the substrate convexly. By convention, the radius of curvature, R , of the substrate/film structure is positive for concave curvature (tensile stress) and negative for convex curvature (compressive stress).

Thermal effects provide significant contributions to film stress (Flinn, 1989). Films prepared at elevated temperatures and then cooled to room temperature or films which are thermally cycled, will be thermally stressed due to differential thermal effects. Therefore, the total mechanical stress σ_{tot} has two components, the thermal stress σ_{therm} and the intrinsic stress σ_{intr} . Hence,

$$\sigma_{tot.} = \sigma_{therm.} + \sigma_{intr.} \quad (2.4)$$

The thermal stress for the film, $\sigma_{therm.}$, results from a difference between the coefficient of thermal expansion of the film α_f and that of the substrate α_s .

Quantitatively, $\sigma_{therm.}$ is given by (Milton, 1992)

$$\sigma_{therm.} = \frac{E_f}{1-\nu_f} \int_{T_1}^{T_2} (\alpha_s - \alpha_f) dT, \quad (2.5)$$

where E_f is the Young's modulus of the film, ν_f is the Poisson's ratio of the film, T_1 and T_2 are the temperature during deposition and at the time of measurement.

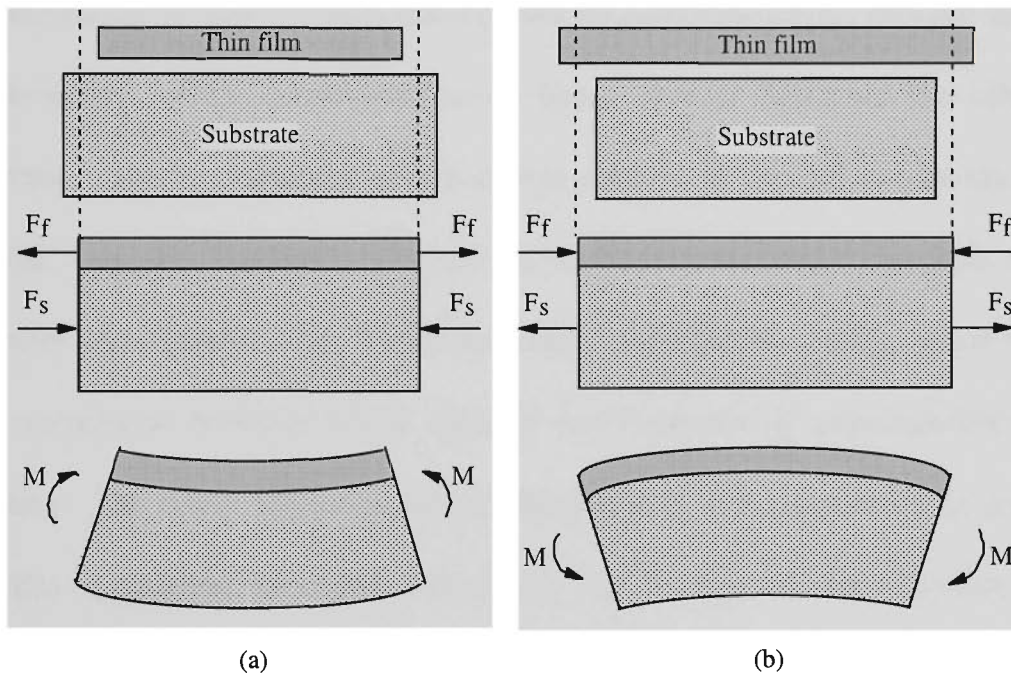


Figure 2.2 (a) Residual tensile stress in a thin film. (b) Residual compressive stress in a thin film. F_i are stress-induced forces and M is the induced bending moment.

Normally, the dominant part of the total stress is the intrinsic or residual stress in the film which originates during deposition (Neugebauer, 1959; Cornella, *et al.*, 1997). Significant mechanical stress is even present in the islands of a partially-

formed film produced during the initial stages of deposition on the substrate. During the network stage of film growth, bridges between the islands are observed and finally a continuous film is formed. Often the maximum stress is reached when the first layer of the film is formed.

The residual stress strongly depends on lattice defects produced during the condensation process. Even in single-crystal films, dislocation concentrations are of the order of 10^{10} to $10^{11}/\text{cm}^2$ (Neugebauer *et al.*, 1959). Such concentration of dislocations in a metal would result in a heavily deformed structure (Kittel, 1976). At film thicknesses of 100 nm and below, these dislocations extend through the entire film thickness. High concentrations of lattice defects influence the other film properties. Due to scattering of the charge carriers at the lattice defects, higher electrical resistance has been observed in metal films compared to bulk material (Horikoshi and Tamura, 1963; Vandamme and Vankemenade, 1997). There is also a strong correlation between lattice disorder and magnetic or superconducting film properties. The stress caused by lattice imperfections can be relieved by annealing after film deposition or, more effectively, by heating of the substrate during deposition. Since higher substrate temperatures can increase the thermal stress the optimum deposition temperature must be found by experiment (Neugebauer *et al.*, 1959; Koch, 1994; Honda, *et al.*, 1997).

Intrinsic stress can also be generated by trapped gas and impurity atoms. There has been no comprehensive study reported in the literature on the influence of residual gas incorporation during deposition on thin film stress. The approach has

been generally to improve the vacuum until the film is pure enough to show no appreciable degradation. Nevertheless the effects of gas contamination can be significant. Oxides or other chemically bonded surface layers can contribute to the residual stress. Significant effects on the intrinsic stress were observed even at low oxygen partial pressure (10^{-7} Pa) in metallic thin films (Winau, 1992). In another study, it was observed that small amount of oxygen incorporated in thin aluminium film can change the sign of the stress (Turner and Aberman, 1990).

Water absorbed by dielectric optical thin films causes (in a multilayer thin film structure) the central wavelength of narrow band optical filters to shift to a longer wavelength (Macleod and Richmond, 1976). The stress reduction in a thin film of MgF_2 due to the water vapour absorption, when the film is exposed to the atmosphere, is between 40% and 100% (Pulker, 1982; Martin, *et al.*, 1998).

Thin film coatings are amongst the most problematic and easily damaged components in any high power laser system due to the residual optical power absorbed in the film. They can be considered the prime constraint to improved system performance. The interaction process between laser beam and thin film is very complex but often the laser beam energy is absorbed by defects in thin films (Glass and Guenter, 1978). This produces breakdown heating in the film and when the temperature rise exceeds some critical value, the induced thermal stress can cause failure of the film. It is well established that the film's internal stress is one of the parameters that affect not only laser induced pulsed damage but also the durability of thin films (Glass and Guenter, 1978). Coatings with minimum possible internal

stress are needed for high power laser applications and this is one of the motivations for the development of the new stress measurement technique described in this thesis.

There is significant interest in measurement techniques which allow accurate measurement of internal stress at the end of deposition process and variations of the stress which are produced under varied deposition conditions. Accurate measurement of the stress in thin films is rather difficult and a number of methods have been devised and described in the literature. These methods, and previous work on stress measurement in thin films, are summarised in the next section.

2.5 Experimental methods for measuring the stress in thin films

A wide variety of techniques have been employed to measure internal stresses. Good critical accounts of them have been given by Campbell (1963) and Hoffman (1966). Excellent reviews of the methods for thin film stress measurement has also been given by Maissel and Glang (1970) and Vinci and Vlassak. (1996).

If the substrate is flexible and the film adheres strongly to the substrate, internal stresses will produce a change in shape in the film/substrate system which can then be measured and used to determine the intrinsic stresses developed in the

film during deposition. Two substrate/film configurations have been primarily used to indirectly estimate, *in situ*, the stresses in thin films:

- (a) Bending plate or membrane methods.
- (b) Bending beam methods.

Other methods (e.g. electron or X-ray diffraction) may also be used but these are generally not suitable for *in situ* measurement.

2.5.1 Circular membranes and bending plate methods

Circular membranes of thin film material have been used to determine the residual stress by measuring the deformation (bulge height) versus pressure (Bromley, *et al.*, 1983). A clean 5.08 cm diameter silicon wafer was coated with 1 μ m of silicon nitride. A circular window pattern was opened on the wafer backside by conventional photolithography and gas plasma etching. The silicon was then etched away using appropriate chemical solution. The stress will bow the film membrane without pressure applied and the deflection δ can be related to the residual stress by

$$\sigma_f = \frac{2E_f\delta^2}{3(1-\nu_f)r}, \quad (2.6)$$

where E_f is the Young's modulus of the film, ν_f is Poisson's ratio and r is the radius of the hole. A known pressure difference was applied on both sides of a membrane. The deflection of the center of the membrane is measured by counting the number of fringes of the reflected interference pattern between a flat mirror and the center of the membrane as a function of pressure. Assuming that the deflection of the membrane is

small compared to its radius, the equation connecting pressure and membrane deflection was found to be

$$p = \frac{4t_f \delta}{r^2} \left[\sigma_f + \frac{2E_f \delta^2}{3(1-\nu)r^2} \right] \quad (2.7)$$

where t_f is the film thickness. The resolution of stress measurement using this method was found to be approximately 10 Pa.

A vibrational technique for stress measurement in films has been developed by Maden *et al.* (1994). The technique is based on the theory of membranes. A 76 μm thick copper sheet was mounted on a square glass plate. A polyamic acid was spin-coated onto the copper substrate. Then, the plate was cured for one hour in a nitrogen atmosphere. After curing, the polyamide film was 10 ± 0.5 μm thick. The sample was removed from the glass plate and the back side of the copper was coated with positive photoresist. A circular mask was used to expose the photoresist. The resist was then developed and the exposed copper was etched away in an appropriate chemical solution. After etching, the sample was rinsed with water and dried.

The natural transverse vibrational frequencies, ω_{mn} , for a circular membrane of radius a , for geometry described above, are given by

$$\omega_{mn}^2 = \left(\frac{\mu_{mn}}{a} \right)^2 \frac{\sigma}{\rho} \quad (2.8)$$

where μ_{mn} is the m -th root of $J_n(x)$, the n -th order Bessel function of the first kind, σ is stress and ρ is the density of the film. This technique does not require a knowledge of

the elastic constants of the film and offers a direct stress measurement. The main drawback of this technique is that buckling can occur in the film. The membranes are also highly sensitive to air currents and audio noise. The resonant frequencies were excited by a mechanical shaker which can cause some difficulties in interpretation of data when the membrane's natural frequencies are close to the natural frequencies of clamping structure.

A second type of 2D substrate configuration frequently employed for stress measurements is the circular plate (Finegan and Hoffman, 1959; Kinbara, 1961; Glang, *et al.*, 1965). The change in the radius of Newton's rings formed between the substrate and an optical flat can be used to measure the deflection of the plate produced by stress. This method also offers the possibility of observing stress anisotropy. This is not an *in situ* method and hence is not suitable for stress measurements during film deposition. A sensor head for *in situ* measurement of stress anisotropy in thin films has been developed by Hornauer, *et al.*, 1990. The method employs an array of capacitor probes and the shape of the deforming plate was determined by monitoring the electrical signals and processing the data by computer.

An optically levered laser technique schematically shown in Figure 4.6, to measure wafer curvature has also been used (Sinha *et al.*, 1978; Rosakis, *et al.*, 1998; Windischmann and Gray, 1995) for residual stress measurements. This technique has so far provided one of the best combinations of accuracy, convenience and speed for most applications (Flinn *et al.*, 1989). A laser beam is reflected from the coated

substrate onto a screen at a known distance from the substrate (section 4.4). From the position of the reflected spot on the screen, the radius, R , of the curved film/substrate composite is calculated using

$$R = 2L \frac{\Delta x}{\Delta x + \Delta d}. \quad (2.9)$$

Here Δx and Δd are the distances of the laser beam and its reflection from the symmetry axis perpendicular to the curved film/substrate structure and L is the distance of the measuring screen from the curved structure. The film stress can be calculated using

$$\sigma_f t_f = \frac{E_s t_s^2}{6R(1-\nu_s)}. \quad (2.10)$$

Here E_s and ν_s are the Young's modulus and Poisson's ratio for the glass substrate, t_s is the thickness of the substrate and t_f ($\ll t_s$) is the film thickness. Equation 2.10 assumes that the substrate is flat before coating. If this is not the case and the initial radius of curvature of the substrate is R_0 before coating, then equation (2.10) becomes (Sahu *et al.*, 1990; Leusink *et al.*, 1992)

$$\sigma_f t_f = \frac{E_s t_s^2}{6(1-\nu_s)} \left(\frac{1}{R} - \frac{1}{R_0} \right). \quad (2.11)$$

It should be noted that the use of laser deflection measurements together with equations 2.10 and 2.11 actually gives the product of stress and film thickness. Independent knowledge of the film thickness (via an additional thickness measurement) is necessary for separate determination of stress.

For measurement of stress changes in a coated sample during thermal cycling, a technique for curvature measurement using a scanning laser method was

developed (Flinn *et al.*, 1987). A laser beam is reflected from the surface of the substrate and the displacement of the beam is determined using a position sensitive detector. The wafer was scanned by an oscillating mirror.

Heterodyne interferometry has also been used to measure the curvature of a uniformly coated 1 μm thick silicon nitride film on a 200 μm thick silicon substrate (Nie, 1980). A gas laser having two orthogonally-polarised outputs which differ in frequency by 1.8 MHz was used for this measurement. These beams were separated in an interferometer and recombined at a detector in such a way that interference was produced after one of the beams was reflected from the coated substrate and the other from a reference retro-reflector. The phase of the output signal of the detector is directly proportional to the bending displacement of the coated substrate at the point where the reflection occurred. The curvature of the substrate was calculated by means of a least-squares curve-fitting program which fitted a circular arc to the measured deflection as the substrate/film combination was scanned across the interferometer beam. This method has limited usefulness for stress measurements as it requires a series of measurements for one sample and is not carried out *in situ*.

2.5.2 Bending - beam methods

In these methods a thin strip of glass or other substrate is rigidly clamped at one end in a fixed mount to form a cantilever onto which the film is deposited.

The deflection of the free end, as the strip becomes bent, is then measured by some means. The principal methods used for deflection measurement are:

- (1) Direct optical observation of the free end with a microscope (Murbach and Wilman, 1953; Novice, 1962).
- (2) Measurement of the electrical capacity formed between the flexible strip and the fixed conducting plate held parallel and close to it (Blackburn and Campbell, 1961).
- (3) Electromechanical measurement of the deflection using a stylus pick-up touching the free end of the cantilever (Campbell, 1963).
- (4) Counting interference fringes formed in a laser interferometer which uses one beam reflected from the free end of the cantilever (Ennos, 1966; Cardinale, *et al.*, 1996).

The deflection of one side of the substrate is proportional to the bending moment exerted on the substrate by the film. The bending moment is also proportional to $\sigma_f t_f$, where t_f is the film thickness and σ_f is the average stress in the film. By substituting the radius of the curvature of the beam, $R = l^2 / (2\delta)$, in equation 2.10, the film stress can be calculated using

$$\sigma_f t_f = \frac{E_s}{(1 - \nu_s)} \frac{t_s^2}{3l^2} \delta. \quad (2.12)$$

In this equation l is the length of the cantilever beam, δ is the beam deflection at the end, t_s is the beam (substrate) thickness and E_s and ν_s are the Young's modulus and Poisson's ratio of the beam, respectively. The sense of the deflection is a direct indication of the kind of stress in the film. For a film deposited on the underside of

the substrate, an upward deflection indicates a compressive stress in the film and tensile stress causes a downward deflection.

2.5.3 Electron-diffraction and X-ray method

Methods based on X-ray and electron diffraction have been used to measure changes in lattice spacing and hence stresses in films. Halliday *et al.* (1954) has published a detailed treatment of stress determination by electron diffraction. The X-ray technique is preferable to electron diffraction because of the higher sensitivity which exists for the larger Bragg angles available and a minimum strain of 10^{-8} has been achieved (Vreeland *et al.*, 1989; Uchida, *et al.*, 1999). The stress (assumed isotropic) in the film plane is computed from the fractional change in the lattice constant given by the relation

$$\sigma_f = \frac{E_f}{1 - \nu_s} \frac{a - a_0}{a_0}, \quad (2.13)$$

where a_0 and a are the lattice constant of the unstressed bulk material and the film, respectively.

2.5.4 Other techniques

Any physical property of the film affected by stress can in principle be used to measure the stress or sense changes in stress. Stress in ferromagnetic films will produce an anisotropy in magnetisation as a result of magneto-elastic coupling.

Since the ferromagnetic resonance frequency depends on the anisotropy as well as the magnetisation, a shift in the resonance peak will occur (MacDonald, 1957).

A single mode optical fibre sensor has been used for the measurement of stress in optical coatings (Shouyao and Jiu-Lin, 1992). Two fibres were attached around a stress sensitive strip. Bending of the strip due to induced stress in its deposited film strains the fibre causing a phase change in light passing through. By counting the fringes the stress was deduced. The drawback with this technique is that the film is also deposited on the fibre and the stress in the film causes the strain in the fibre as well.

Table 2.1 summarises the measured performance obtained with a range of techniques for measuring the deflection of the cantilever beam or plate caused by developed stress in the deposited film. While this table is relatively old, improvements have mostly been made in the quality of the films (due to better vacuums) rather than the sensitivity of the techniques for stress measurement. Hence, the data in Table 2-1 still gives a reasonable picture of the situation with regard to the sensitivity of the techniques. Data is also included in the table for some non-deflection methods for comparison purposes. For thicker films these methods are sufficiently sensitive but, during initial film growth, where stress is small, the more sensitive interferometric methods are needed. With all techniques involving bending or deformation of the substrate, the effect of the stress caused by the film will be larger if the thickness of the substrate is decreased. Hence it is generally possible to improve sensitivity by appropriate choice of substrate.

Table 2.1 Sensitivity of stress-measuring techniques after Hoffman (1966)

Method of observing deflection	Type of plate ^{a)}	Detectable stress times film thickness, (Pa m)	Reference
Optical	B	0.8	Hoffman <i>et al.</i> , 1954
Capacitance	C	0.5	Blackburn and Campbell, 1961
Optical	C	0.25	Murbach and Wilman, 1953
Magnetic restoration	C	0.25	Priest and Caswell, 1961
Electromechanical restoration	C	0.15	Story and Hoffman, 1957
Mechanical	C	0.001	Blackburn and Campbell, 1963
Electromechanical	C	0.001	Klokholm, 1969
Interferometric	P	0.015	Finegan and Hoffman, 1961
Ferromagnetic resonance		1.0	MacDonald, 1957
X-ray		0.5	Kinbara, 1961

a) B is shorthand notation for beam supported on both ends; C is for cantilever beam and P for circular plate.

2.6 Vibrations of thin plates and shells

The stress measurement technique developed in this thesis relies on sensing the changes in modal frequency of a film/substrate combination in the form of a thin disk or shell (when the plate is bent due to stress in film). This section is intended to briefly summarise information relevant to an understanding of this technique. A more detailed treatment of the derivation of the equations applying to the plates and shells used in this work is contained in chapter 3.

The vibration of plates and shells has been widely studied, both theoretically and experimentally, for a considerable period of time and there is a substantial amount of literature on the subject (Timoshenko and Woinowsky-Kriger, 1959; Morse and Ingard, 1968; Reissner, 1946). The shapes and frequencies of the

vibrational modes of plates and shells is an important topic in many areas of structural mechanics because thin plate and shell structures are widely used in building construction, shipbuilding, aerospace and acoustics.

Any elastic structure will possess one or more natural frequencies of vibration. The natural frequencies are the result of periodic exchange of kinetic and potential energy within the structure during vibration. The rate of energy exchange between the potential and kinetic forms of energy determines the natural frequency.

Plates and shells possess bending rigidity as a result of their thickness and the elasticity of the material. During transverse vibrations, plates and shells deform primarily by flexing perpendicular to their surface. The resonant vibrational modes of this structures will be considered in chapter 3.

2.6.1 Mechanical vibrations of circular plates

The symmetrical oscillations of thin circular plates can be calculated using the theory of elasticity (Timoshenko and Young, 1966). The general assumptions used in the analysis of the vibrations of these plates (McLachlan, 1951; Blevins, 1979) are:

- a) Vibration occurs *in -vacuo*.
- b) The plate is composed of a perfectly linear elastic, homogeneous, isotropic material.

- c) The plate has uniform thickness less than about $1/10$ the minimum lateral plate dimension.
- d) The plate deforms through flexural deformation.
- e) The maximum displacement (amplitude) is small in comparison with the thickness of the plate.
- f) Normals to the mid surface do not change direction during deformation.
- g) The deformation of the plate due to gravity is neglected.

This thesis considers only plates mounted by fixing a rod to the centre and holding this rod rigidly in a clamp. Prescott (1961) has considered the problem of vibration involving this geometry and has obtained an analytical expression for the dependence of fundamental frequency (first mode) on dimensions and mechanical properties. In chapter 3 the frequencies of the higher resonant modes are derived and three-dimensional displacement graphs for the first nine resonant modes are plotted. It is shown that the effect of stiffness increases the frequency of higher harmonics more than it does of the lower harmonics.

2.6.2 Vibrations of shallow spherical shells

Analysis of the natural frequencies and mode shapes of shells is much more complex than analysis of flat plates. Shell theories must incorporate flexural and extensional deformations. However, the theory of transverse vibration of plates

considers only flexural deformations, since the extensional deformation of the plates is zero. The natural frequencies of shells are a function of the axial constraint applied by the clamping mechanism (boundary conditions). The vibration of shells clamped at the edges is described in terms of an eighth-order differential equation. Because of the complexity of the shell equation only a few approximate solutions for the natural frequencies and mode shapes of shells are available in the literature. The main difference between the theories is due to the various assumptions (Blevins, 1979; Gibson, 1980) made in the analysis of shells.

A simplified shell theory, called the ‘shallow shell theory’ has been developed to describe the vibrations of shallow curved shells (Reissner, 1946; Hoppmann, 1961). It was shown that even a small alteration in curvature of the shell strongly affects its resonant vibrational frequencies. There is a close relation between the natural frequencies and mode shapes of flat plates and those of similar shallow spherical shell segments (Soedal, 1973). If a homogeneous plate and segment of a shallow spherical shell have identical boundary conditions (i.g. clamped edge, free edge, simply supported edge) the natural frequencies are related by (Soedal, 1973):

$$f_{mn(s)} = \sqrt{f_{mn(p)}^2 + \frac{E}{4\pi^2 \rho R^2}}, \quad (2.14)$$

where $f_{mn(s)}$, $f_{mn(p)}$ is natural frequencies of the mn mode of the shell and the plate respectively, E is the Young's modulus, ρ is the material density and R is the radius to the mid surface of the shallow spherical segment. For a flat plate, $1/R = 0$. When the coating is deposited on the plate the isotropic stress developed in the film will

induce changes in plate/film curvature and equation 2.14 can be used to determine the change in modal resonant vibrational frequencies of this mechanical system.

2.7 Summary

As stated in section 1.2, the technique for stress measurement in thin films, described in this work, is based on laser generation of vibrations of substrate/film structure and remote detection by a fibre optic interferometer. It is clear from the above review of experimental methods for measuring stress in thin films that this technique represents a novel approach for *in situ* stress measurements in thin films.

Theoretical basis of the technique for stress determination in thin films

3.1 Introduction

A thin flat glass plate mounted on a thin central pillar was chosen as a substrate arrangement for the measurement of stress in evaporated thin films in this thesis. For a given excitation, this supporting geometry resulted in less damping and larger amplitude of vibration than was the case when the plate was supported around the circumference. This arrangement thus gave a relatively large signal-to-noise ratio in the detected vibration signals.

This chapter will discuss the mechanical vibrations of a flat plate and a shallow spherically curved thin shell, both of which use the above support geometry. Analytical expression is derived for the resonant mechanical vibration frequencies of a

flat glass plate and these are compared, for the purposes of validation, with the results obtained using Finite Element Modeling (FEM). The analytical results are then extended to the case of a shallow spherical shell and frequencies obtained using these expressions are again compared with those obtained using FEM. All of the above work applies only to the special case of an isotropic homogeneous plate or shell.

Stress and strain relationships are then presented and an analytical expression is derived for the residual stress in a thin film on a much thicker substrate of different material. The difference between the Young's moduli of film and substrate are neglected in this expression as the film is assumed to be very thin. The derivation is subsequently extended to include the case of film stress in situations for which:

- a) The film thickness was not negligible in comparison with the substrate thickness.
- b) The Young's modulus of the film and the substrate are different.

The equations derived above are used to obtain an expression which relates the stress in a curved substrate/film combination to the resonant frequency of the curved structure and that of the previously flat substrate. One needs to know both these frequencies to calculate the stress. It is clear that the presence of a coating will modify the resonant frequency of a substrate even if there is no stress present at the interface and hence there is no curvature produced (change in thickness and average density will change resonant frequency). Thus the frequency shift produced in a substrate/film combination when it

curves under stress should be adjusted for this effect if one wishes to calculate the effect of stress alone. The final section of this chapter addresses this correction.

3.2 The general solution for vibration of uniform thin flat plates

The symmetrical oscillations of thin plates clamped at the center can be calculated using the standard theory of elasticity (Prescott, 1961). The general assumptions used in this analysis for a plate are given in section 2.5.1.

The oscillation of a uniform plate of half-thickness h are described by the equation (Prescott, 1961)

$$\nabla^4 \eta + \frac{3 \rho (1 - \nu^2)}{E h} \frac{\partial^2 \eta}{\partial t^2} = 0. \quad (3.1)$$

Here η is the displacement of any point at time t in a direction perpendicular to the plate and ρ , ν and E are the density, Poisson's ratio and Young's modulus of the material, respectively.

If M_1 represents the bending moment on a section of the circular plate which is perpendicular to r at radius r and M_2 represents the bending moment on a section

which is perpendicular to the previous one, then these bending moments can be shown to be given by (Prescott, 1961):

$$M_1 = \frac{2}{3} \frac{Eh^3}{(1-\nu^2)} \left(\frac{d^2\eta}{dr^2} + \frac{\nu}{r} \frac{d\eta}{dr} \right). \quad (3.2)$$

$$M_2 = \frac{2}{3} \frac{Eh^3}{(1-\nu^2)} \left(\frac{1}{r} \frac{d\eta}{dr} + \nu \frac{d^2\eta}{dr^2} \right). \quad (3.3)$$

The shear force per unit length in the direction of the z axis (perpendicular to the plate) on the same two sections is given by (Prescott, 1961):

$$F_1 = -\frac{2}{3} \frac{Eh^3}{(1-\nu^2)} \frac{d}{dr} \left[\frac{1}{r} \frac{d}{dr} \left(r \frac{d\eta}{dr} \right) \right] \quad (3.4)$$

and $F_2=0$. The latter result is simply a consequence of the fact that there is no dependence on θ due to symmetry about the z axis. The general solution of equation (3.1) for oscillations which are symmetrical about the z axis of the plate is given by (Prescott, 1961)

$$\eta = [AJ_m(kr) + BZ_m(kr) + CI_m(kr) + DH_m(kr)] \sin(2\pi ft), \quad (3.5)$$

with

$$k^4 = \frac{12\pi^2 f^2 \rho (1-\nu^2)}{Eh^2}, \quad (3.6)$$

where A, B, C and D are constants determined by the boundary conditions. In this equation, f is the frequency of vibration, J_m is the Bessel function of order m , Z_m is Neumann's form of the m -th order Bessel function of the second kind (Watson, 1944),

$$I_m = i^{-m} J_m(ix) \text{ and } H_m = i^{-m} Z_m(ix) - I_m(x) \log(i).$$

In the next section, equation 3.5 will be used to derive the frequency of vibration of a thin circular plate clamped in the center. From the boundary conditions for this geometry, the constants A, B, C and D will be determined and an analytical expression for the allowable vibrational frequencies will be obtained.

3.3 Symmetrical oscillations of a circular plate clamped at the center

For a circular plate of radius a , clamped at the centre, the following two boundary conditions at the centre ($r = 0$) must be satisfied

$$\eta = 0 \tag{3.7}$$

$$\frac{d\eta}{dr} = 0. \tag{3.8}$$

The boundary conditions at the rim ($r = a$) must also be satisfied and these can be obtained by substituting $M = 0$ and $F = 0$ in equations (3.2) and (3.3). Therefore,

$$\frac{d^2\eta}{dr^2} + \frac{\nu}{r} \frac{d\eta}{dr} = 0, \text{ and} \tag{3.9}$$

$$\frac{d}{dr} \left[\frac{1}{r} \frac{d}{dr} \left(r \frac{d\eta}{dr} \right) \right] = 0. \tag{3.10}$$

Equations 3.7-3.10 can be used to determine the four constants (A, B, C, D) in equation 3.5. This can be done in the following way:

Without loss of generality, let $C = cA$ and $D = dB$. Then equation 3.5 becomes

$$\eta = \left\{ A \left[J_m(kr) + cI_m(kr) \right] + B \left[Z_m(kr) + dH_m(kr) \right] \right\} \sin(\omega t). \quad (3.11)$$

The two conditions (3.7) and (3.8) give

$$A \left[J_m(0) + cI_m(0) \right] + B \left[Z_m(0) + dH_m(0) \right] = 0, \quad (3.12)$$

and

$$A \left[J'_m(0) + cI'_m(0) \right] + B \left[Z'_m(0) + dH'_m(0) \right] = 0. \quad (3.13)$$

This equation can be simplified using

$$J_m(0) = 1, I_m(0) = 1, \text{ and} \quad (3.14)$$

$$J'_m(0) = 0, I'_m(0) = 0. \quad (3.15)$$

Also, when $kr \ll 1$,

$$Z_m(kr) \approx J_m(kr) \ln(kr) \approx \ln(kr), \quad (3.16)$$

$$H_m(kr) \approx I_m(kr) \ln(kr) \approx \ln(kr), \text{ and} \quad (3.17)$$

$$Z'_m(kr) = \frac{1}{kr}, H'_m(kr) = \frac{1}{kr}. \quad (3.18)$$

Under these conditions, equation 3.11 is satisfied provided $A(1+c) = 0$, giving $c = -1$.

Similarly, one obtains $B(1+d) = 0$. If we put $B=0$ we should not have enough available constants to satisfy the two conditions at the rim, therefore, we must take $d = -1$.

Using these results,

$$\eta = \left\{ A \left[J_m(kr) - I_m(kr) \right] + B \left[Z_m(kr) - H_m(kr) \right] \right\}. \quad (3.19)$$

If we put

$$u = J_m(kr), u_1 = Z_m(kr), \text{ and} \quad (3.20)$$

$$v = I_m(kr), v_1 = H_m(kr), \quad (3.21)$$

then u and u_1 satisfy

$$\frac{d^2u}{dr^2} + \frac{1}{r} \frac{du}{dr} = -k^2u, \text{ and} \quad (3.22)$$

also, v and v_1 satisfy

$$\frac{d^2v}{dr^2} + \frac{1}{r} \frac{dv}{dr} = k^2v. \quad (3.23)$$

Using the relations above, equation (3.11) becomes

$$\eta = \left\{ A(u - v) + B(u_1 - v_1) \right\} \sin(2\pi). \quad (3.24)$$

The two conditions (3.9) and (3.10) reduce to

$$k^2 \left\{ A(u - v) + B(u_1 - v_1) \right\} + \frac{1-v}{r} \left\{ A \left(\frac{du}{dr} - \frac{dv}{dr} \right) + B \left(\frac{du_1}{dr} - \frac{dv_1}{dr} \right) \right\} = 0, \quad (3.25)$$

and

$$A \left(\frac{du}{dr} - \frac{dv}{dr} \right) + B \left(\frac{du_1}{dr} - \frac{dv_1}{dr} \right) = 0, \quad (3.26)$$

both of which must be true when $r = a$. Using equations 3.14 and 3.15 the last two equations can be written as

$$-\frac{B}{A} = \frac{b(J_m(b) + I_m(b)) + (1-v)(J'_m(b) - I'_m(b))}{b(Z_m(b) + H_m(b)) + (1-v)(Z'_m(b) - H'_m(b))} \quad (3.27)$$

$$-\frac{B}{A} = \frac{J'_m(b) + I'_m(b)}{Z'_m(b) + H'_m(b)} \quad (3.28)$$

where $b = ka$.

The following relations (Watson, 1944) can be used to simplify these expressions:

$$J'_m(x) = \frac{1}{2} [J_{m-1}(x) - J_{m+1}(x)], \quad (3.29)$$

$$I'_m(x) = \frac{1}{2} [I_{m-1}(x) - I_{m+1}(x)], \quad (3.30)$$

$$Z_m(x) = \frac{\pi}{2} Y_m(x) + \lambda J_m(x), \quad (3.31)$$

$$Z'_m(x) = \frac{\pi}{2} \left[Y_m(x) - \frac{m}{b} Y_{m+1}(x) \right] + \frac{\lambda}{2} [J_{m-1}(x) - J_{m+1}(x)], \quad (3.32)$$

$$H_m(x) = \lambda I_m(x) + \frac{K_m(x)}{(-1)^{m+1}}, \quad (3.33)$$

$$H'_m(x) = -\frac{m}{x} \left[\lambda I_m(x) + \frac{K_m(x)}{(x)^{m+1}} \right] + \lambda I_{m+1}(x) + \frac{K_m(x)}{(x)^{m+2}}, \quad (3.34)$$

$$J_{-m}(x) = -J_m(x), \text{ and} \quad (3.35)$$

$$I_{-m}(x) = I_m(x). \quad (3.36)$$

Here $\lambda = \ln 2 - \gamma$ and γ is Euler's constant ($\gamma = 0.5772156649$). As the $\lambda J_m(b)$, $\lambda I_m(b)$, $0.5[\lambda J_{m-1}(b) - \lambda J_{m+1}(b)]$ and $\lambda I_{m+1}(b)$ are $\ll 1$ and if, for simplicity, we denote either side of equation (3.27) as $L(b)$ and (3.28) as $R(b)$ they become

$$L(b) = \frac{b[J_m(b) + I_m(b)] + \frac{1-\nu}{2} [J_{m-1}(b) - J_{m+1}(b) - I_{m-1}(b) - I_{m+1}(b)]}{b \left[\frac{\pi}{2} Y_m(b) + \frac{K_m(b)}{(-1)^{m+1}} \right] + (1-\nu) \left[Y_{m-1}(b) - \frac{m}{b} Y_{m+1}(b) \right] + \frac{m}{b} \frac{K_m(b)}{(-1)^{m+1}} - \frac{K_{m+1}(b)}{(-1)^{m+2}}},$$

and

$$R(b) = \frac{1}{2} \frac{J_{m-1}(b) - J_{m+1}(b) + I_{m-1}(b) + I_{m+1}(b)}{\frac{\pi}{2} \left[Y_{m-1}(b) - \frac{m}{b} Y_{m+1}(b) \right] + \frac{m}{b} \frac{K_m(b)}{(-1)^{m+1}} - \frac{K_{m+1}(b)}{(-1)^{m+2}}}$$

With this notation we can write

$$L(b) - R(b) = 0. \quad (3.37)$$

This equation determines the allowed values of the frequency, because $b = ka$ and k depends on frequency. For each value of m there will be an infinite number of solutions of equation (3.37). Labelling the allowed values of the frequency f_m where m is the number of diametrical nodal lines and n is the number of circular nodes the equations (3.5) and (3.37) can be written as

$$k_{mn}^4 = \frac{12\pi^2 f_{mn}^2 \rho(1 - \nu^2)}{Eh^2}, \quad (3.38)$$

and

$$L(b_{mn}) - R(b_{mn}) = 0, \quad (3.39)$$

where $b_{mn} = k_{mn} a$.

Nine values for b_{mn} have been calculated by interpolation of equation (3.37) using Mathematica software:

$$\begin{array}{lll} b_{01} = 1.92853 & b_{02} = 4.55962 & b_{03} = 7.780656 \\ b_{11} = 2.49691 & b_{12} = 5.817204 & b_{13} = 9.021673 \\ b_{21} = 3.75798 & b_{22} = 7.239655 & b_{23} = 10.4927049. \end{array}$$

It should be mentioned that the equation 3.39 is sensitive to the number of decimal places. The allowed values of the frequency are therefore

$$f_{mn} = \frac{h}{2\pi a^2} (b_{mn})^2 \sqrt{\frac{E}{3\rho(1-\nu^2)}} , \quad (3.40)$$

and the fundamental frequency is

$$f_{01} = 0.348 \frac{h}{a^2} \sqrt{\frac{E}{\rho(1-\nu^2)}} .$$

Another way of writing these results is

$$\begin{array}{lll} f_{02} = 5.593 f_{01} & & f_{03} = 16.225 f_{01} \\ f_{11} = 1.677 f_{01} & f_{12} = 9.103 f_{01} & f_{13} = 21.894 f_{01} \\ f_{21} = 3.799 f_{01} & f_{22} = 14.099 f_{01} & f_{23} = 29.617 f_{01}. \end{array}$$

As can be seen, the non fundamental frequencies of vibration are not integral multiples of f_{01} , hence the allowed frequencies do not form a harmonic series. If r is very small (the region around clamping point) the terms involving $\ln(kr)$ in equations (3.16) and (3.17) are dominant, then we can write equation (3.19) as

$$\eta = B[Z_m(kr) - H_m(kr)]\sin(\omega t) . \quad (3.41)$$

By substituting the equations 3.16 and 3.17 the equation 3.41 becomes

$$\eta = B[J_m(kr) - I_m(kr)]\ln(kr)\sin(\omega t) , \quad (3.42)$$

or

$$\eta = -2B \left(\frac{k^2 r^2}{2^2} + \frac{k^6 r^6}{2^2 4^2 6^2} + \dots \right) \ln(kr)\sin(\omega t) . \quad (3.43)$$

Thus when r is small we can write

$$\eta = -\frac{1}{2} B k^2 r^2 \ln kr \sin(\omega t) . \quad (3.44)$$

By combining equations 3.39 and 3.3 the approximate value of the shear force when r is small is given by

$$F = -\frac{1}{3} \frac{EBk^2h^3}{(1-\nu^2)} \frac{d}{dr} \left[\frac{1}{r} \frac{d}{dr} \left(r \frac{d(r^2 \ln kr)}{dr} \right) \right] \quad (3.45)$$

$$F = -\frac{4}{3} \frac{EBk^2h^3}{1-\nu^2} \frac{1}{r}. \quad (3.46)$$

Equation 3.46 suggests an infinite shearing force at the centre of the plate. Thus the conditions we have assumed in this derivation (specifically that the plate is fixed at a point in the centre) cannot exist in practice. In reality the plate is held fixed over a finite circular region. The results presented here should apply with fair accuracy when the support is small compared to the radius of a plate. The dynamic analysis of a flat glass plate, using Finite Element Modelling (FEM), has shown that a 7% increase of the radius of the metal support rods will cause the frequency changes of 0.01 Hz. In addition, the radius of circular glass plates used in experiments was 28 times larger than the radius of the metal support rods, so equation 3.40 can be applied with confidence.

3.4 3D plots of solution for circular plate clamped at the center

Figures 3.1 to 3.3 shows instantaneous three-dimensional plots of the vibrational amplitudes for nine of the vibrational modes of the flat plate. These modal shapes are obtained by plotting equation 3.42.

3.5 Calculated and measured resonant mechanical vibration of substrate used for stress measurement in thin films

The substrates used to measure the stress in thin films were thin glass plates as described in section 4.3.1. Substitution of appropriate constants for the glass plate [$E_s = 7.2 \times 10^{10}$ Pa, $\nu = 0.25$, (Malecki, 1969), $\rho = 2.51 \times 10^3$ kg/m³ (as shown in Appendix 1), $a = 21 \times 10^{-3}$ m and $2h = 110$ μ m] in equation (3.40) gives

$$f_{mn} = 63.55 \times (b_{mn}^2). \quad (3.47)$$

The calculated values for natural resonant frequencies of the first nine vibration modes are given in Table 3.1.

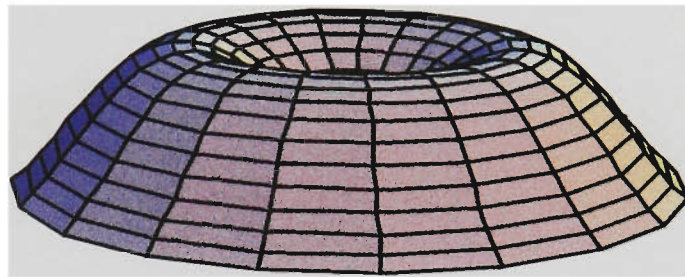
$$b_{01} = 1.92853$$

$$f_{01} = 236.3 \text{ Hz}$$



$$b_{02} = 4.55962$$

$$f_{02} = 1320.7 \text{ Hz}$$



$$b_{03} = 7.780656$$

$$f_{03} = 3845.7 \text{ Hz}$$

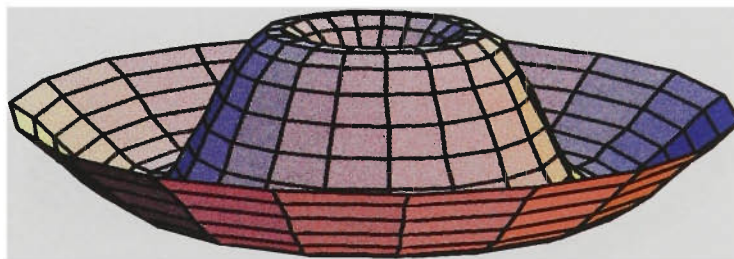
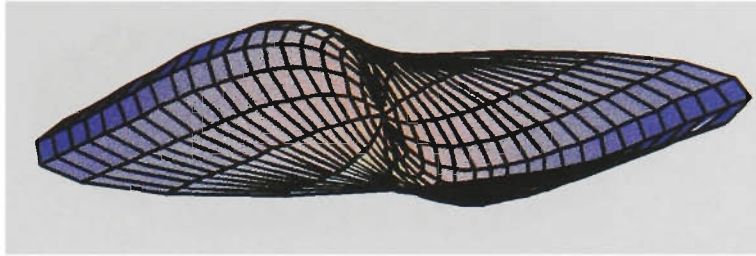


Figure 3.1

Representation of the first 3 natural modes of vibration of a circular plate clamped at the center. The frequencies of vibration do not form a harmonic series.

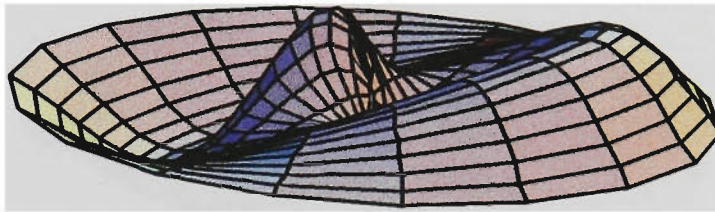
$$b_{11} = 2.49691$$

$$f_{11} = 396.0 \text{ Hz}$$



$$b_{12} = 5.817204$$

$$f_{12} = 2149.7 \text{ Hz}$$



$$b_{13} = 9.021673$$

$$f_{13} = 5170.3 \text{ Hz}$$

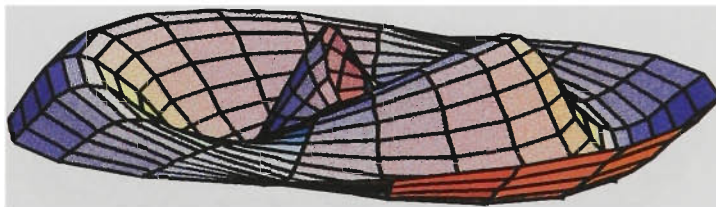
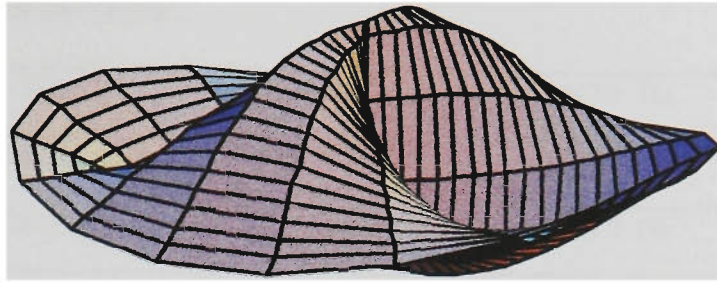


Figure 3.2

Representation of the 4th, 5th and 6th natural modes of vibration of a circular plate clamped at the center.

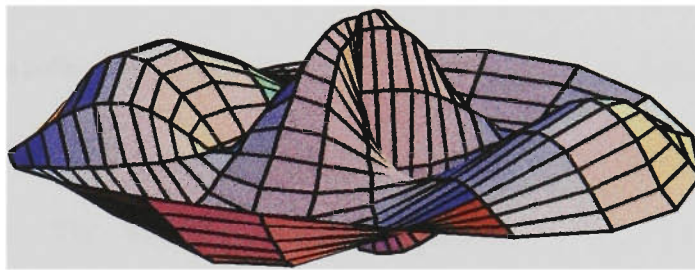
$$b_{21} = 3.75798$$

$$f_{21} = 897.1 \text{ Hz}$$



$$b_{22} = 7.239655$$

$$f_{22} = 3329.5 \text{ Hz}$$



$$b_{23} = 10.4927049$$

$$f_{23} = 6993.9 \text{ Hz}$$

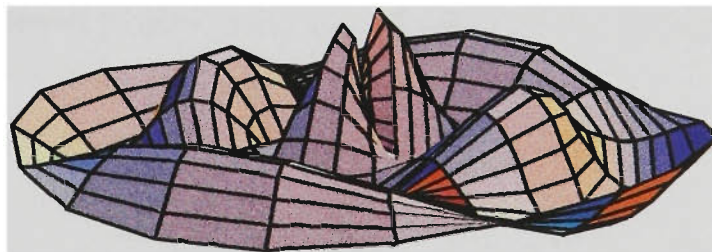


Figure 3.3

Representation of the 7th, 8th and 9th natural modes of vibration of a circular plate clamped at the center.

Table 3.1 Calculated value for natural resonant frequency for flat circular glass plate clamped in the center.

$f_{01} = 236.3 \text{ Hz}$	$f_{11} = 396.0 \text{ Hz}$	$f_{21} = 897.1 \text{ Hz}$
$f_{02} = 1320.7 \text{ Hz}$	$f_{12} = 2149.7 \text{ Hz}$	$f_{22} = 3329.5 \text{ Hz}$
$f_{03} = 3845.7 \text{ Hz}$	$f_{13} = 5170.3 \text{ Hz}$	$f_{23} = 6993.9 \text{ Hz}$

To preserve the flatness of the plate during optical measurements to check these frequencies, a 10 nm thick chromium film was deposited on both side of glass sample as shown in figure 3.4. The flatness of the sample was measured using an optical lever technique as describe in section 4.5.1. These measurements confirmed that there was negligible change in the flatness produced by gluing the metal support rod in the centre of the sample. The sample was than placed in the vacuum system and the frequency measurements were obtained in the air and under a vacuum of 10^{-5} Pa. The measured values are presented in Table 3.2. The removal of the damping produced by the air typically increases the resonance frequency of the sample, for modes with resonant frequencies above 2 kHz by less than 1%. While these frequency changes are

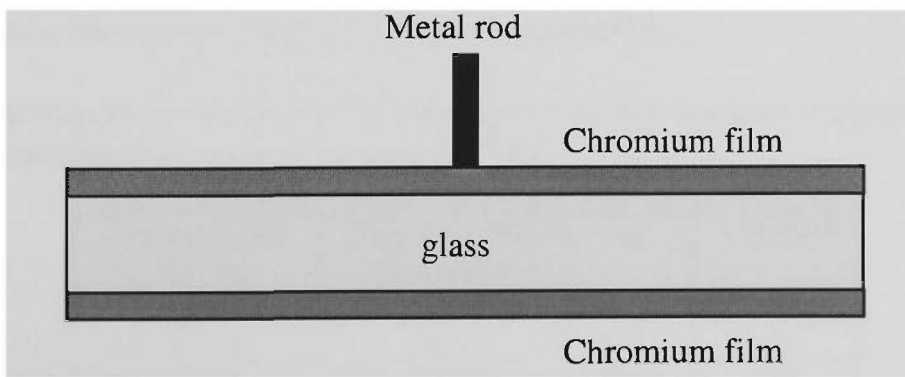


Figure 3.4 The sample used to measure the frequency of flat plate.

Table 3.2 The measured resonant frequencies of a flat circular glass plate in air and in vacuum (10^{-5} Pa).

Frequency (Hz) -in air	Frequency (Hz) - in vacuum(10^{-7} mbar)	Δf	Δf (%)
225.2	229.4	4.2	1.83
360.1	385.3	25.1	6.54
849.3	881.3	32	3.6
2130.6	2138.2	7.6	0.355
3268.3	3296.7	28.4	0.86

small, they are very easily resolved with the interferometer system. In principle, the elimination of the air damping can slightly increase the quality factor and hence the accuracy in determining the peak of the resonance curve. In practice the effect on accuracy is negligible.

As stated in section 2.5.1, one of the general assumption used in the analysis of the plates is that vibrations occur *in-vacuo*. The calculated resonant frequency using equation 3.47 and measured values at a pressure of 10^{-7} mbar are presented in Table 3.3. The difference between theoretical calculations and experimental data for modes greater than 2 kHz is less than 1% and this difference could easily be accounted for by uncertainties in the assumed values of the glass parameters.

Table 3.3 Comparison between calculated and measured resonant frequencies of a flat circular glass plate in vacuum (10^{-5} Pa).

Frequency (Hz) (theory)	Frequency (Hz) (experiment)	Δf	Δf (%)
236.26	229.4	6.86	2.90
396.05	385.3	10.75	2.71
897.13	881.3	15.83	1.76
2149.68	2138.2	11.48	0.53
3329.51	3296.7	32.81	0.98

An alternative method of calculating modal resonant frequencies involves numerical calculations using Finite Element Modeling (FEM). This method has the advantage that it can also be used for plate geometries which are not as simple as the flat plate above and which cannot be handled analytically. FEM was used to check all analytical results for plates and shells derived in this chapter. The mode shapes and resonant mechanical vibration frequencies of a uniform homogeneous circular glass plate were studied using ANSYS5.3 software. This plate had the same dimensions and physical properties as those used in the previous calculations and the thin films were neglected. The number of mesh elements used was 360 and the minimum element surface area (sector near the support) was $49 \mu\text{m}^2$. The area of the plate attached to the metal rod was restrained to have zero amplitude of displacement. Tables 3.4 and 3.5 compare the results of FEM with resonant frequencies calculated using equation 3.40

Table 3.4 Comparison of calculated resonant frequencies, using equation 3.40, for a flat glass plate and data obtained using FEM.

Frequency (Hz) - theory	FEM	Δf	Δf (%)
236.26	240.12	3.86	-1.63
396.05	384.02	12.03	3.04
897.13	872.26	24.87	2.77
2149.68	2187.13	-37.45	-1.74
3329.51	3343.04	-13.53	-0.4

and with measured values. While there are limitations to the accuracy of the calculations as a result of the assumptions involved in the analytic and FEM methods, it is clear that equation 3.40 and FEM gives result which agrees quite well with experiment. The FEM calculations were also used to check the effect of the glue used to attach the central metal

clamping rod. The glue increased the diameter of this attachment from 1.5 mm to 1.6 mm. The FEM calculations showed that this produced a change in resonant frequency of only about 0.01 Hz.

Table 3.5 Comparison of experimental results of resonant frequencies for a flat glass, obtained in vacuum of 10^{-7} mbar, for a flat glass plate and data obtained using FEM.

Frequency (Hz) - experiment	FEM	Δf	Δf (%)
229.4	240.12	-10.72	-4.47
385.3	384.02	1.28	0.33
881.3	872.26	9.04	1.03
2138.2	2187.13	-48.93	-2.24
3296.7	3343.04	-46.34	-1.39

3.6 Mechanical vibrations of shallow spherical shells

With good adhesion of the film-substrate structure, strong deformation of the thin substrate often takes place due to stress developed in the film. With the assumption that the stress in a uniformly-deposited film is isotropic, this stressed structure can be considered as a shallow spherical shell.

Analysis for the natural frequencies and mode shapes of shells is generally much more complex than the analysis for plates. There is no general agreement (Blevins, 1979; Gibson, 1980) in the literature on the best method of simplification and

solution of the linear differential equations which describe the deformations of a shell. A number of approaches have been used. Prominent among these are the approaches of Timoshenko and Woinowsky-Krieger (1959) and Nowacki (1963). The vibration of shells is described in terms of an eighth-order differential equation. Because of the complexity of the shell equation only a few approximate solutions for the natural frequencies and mode shapes of shells are available in the literature.

A simplified shell theory, called shallow shell theory, has been developed to describe the vibrations of shallow curved shells (Reissner, 1946; Hoppmann, 1961). This work has shown that even a small alteration in curvature of the shell strongly affects its resonant vibrational frequencies. There is a close relation between the natural frequencies and mode shapes of flat plates and those of similar shallow spherical shell segments (Soedal, 1973). If a plate and segment of a shallow spherical shell have identical boundary conditions (i.g. clamped edge, free edge, simply supported edge etc.) the natural frequencies are related by (Soedal, 1973):

$$f_{mn(s)} = \sqrt{f_{mn(p)}^2 + \frac{E}{4\pi^2\rho R^2}} \quad (3.48)$$

where $f_{mn(s)}$, and $f_{mn(p)}$ are the natural frequencies of the mn mode of the shell and plate respectively, E is the Young's modulus, ρ is the material density and R is the radius of curvature measured to the mid surface (neutral axis) of the shallow spherical segment. For a flat plate, $1/R = 0$. It should be noted that the general assumptions used in analysis of flat plates, given in section 2.5.1, are, also, applicable in the analysis of thin shells.

Because of the complexity of the shell equation, the normal mode shapes and frequencies of the shallow spherical shell were also studied by the ANSYS 5.3 FEM software. The FEM models of the flat plate and the shallow spherical shells all have the same number of elements and number of nodes; similar mesh patterns and material properties. It was assumed that the surface area at the neutral plane of the shell and the flat plate are the same. The mesh geometry used is shown schematically in figure 3.5.

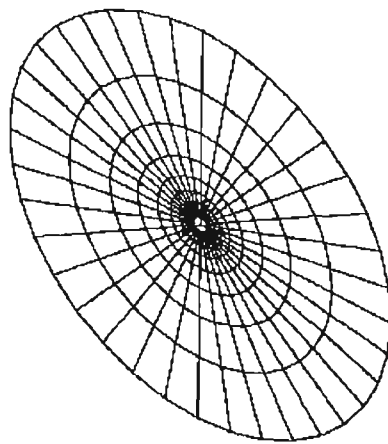


Figure 3.5. Isometric view of the mesh pattern used for FEM calculations with plates and shells.

Over a frequency range of 100 Hz to 5000 Hz, the FEM modal analysis gives a far greater number of normal modes of vibration than those which can be excited by the modulated laser beam. The laser excitation method can excite only bending modes but not modes which correspond to displacements in the plane of the plate or the shell.

The resonant frequency shifts with different radii of curvature for several modes are given in Table 3.6. This table compares calculated data using equation 3.48 and data obtained from finite element modeling. These data are graphically represented in figure 3.6. The differences between these sets of data is less than 1.3%. Therefore

Table 3.6 Comparison of calculated resonant frequencies, using equation 3.48 for a curved glass plate, clamped in the center, and data obtained using FEM. The frequency shifts shown are the differences in frequency between the curved and flat plates. The resonant frequency of flat glass was obtained using FEM method.

Radius (m)	Mode 2300 Hz			Mode 3400 Hz			Mode 4600 Hz		
	Δf_3 (Hz) equ 3.48	Δf_3 (Hz) FEM	Δ (Hz)	Δf_4 (Hz) equ 3.48	Δf_4 (Hz) FEM	Δ (Hz)	Δf_5 (Hz) equ 3.48	Δf_5 (Hz) FEM	Δ (Hz)
6.0	2.3	1.0	-1.3	3.1	2.3	-1.2	2.2	0.7	-1.5
5.0	4.3	-0.3	-4.0	4.4	2.7	-2.7	3.1	0.0	-3.1
4.0	7.9	0.9	-7.0	6.9	4.4	-2.5	4.9	0.3	-4.6
3.0	15.7	7.1	-8.6	12.1	9.3	-2.8	8.7	3.0	-5.7
2.0	37.9	29.5	-8.4	27.2	25.3	-1.9	19.7	14.2	-5.5
1.8	47.2	39.4	-7.8	33.6	32.2	-4.4	24.4	19.3	-5.1
1.6	60.2	53.2	-7.0	42.4	42.8	0.4	30.8	26.6	-4.2
1.4	79.0	73.1	-6.1	55.3	56.0	0.7	40.2	37.5	-2.7
1.2	107.6	104.1	-3.5	75.0	79.0	4.0	54.7	54.5	-0.2
1.0	154.4	154.4	-0.0	107.5	115.0	7.5	78.6	82.3	3.7
0.9	189.6	192.3	2.7	132.2	142.8	10.6	96.8	103.8	7.0
0.8	238.1	244.4	6.3	166.5	181.3	14.8	122.2	133.8	11.2
0.7	307.2	318.5	11.3	215.9	236.8	20.9	159.0	177.	18.0
0.6	410.1	428.5	18.4	290.7	320.7	30.0	215.1	243.6	28.5
0.5	572.6	601.3	28.7	411.5	455.8	44.3	306.8	351.9	45.1

equation 3.48 has been used throughout this thesis in situations requiring an analytic expression relating frequency shift to radius of curvature. Specifically it has been used

to relate modal frequency shift to stress via a separate relationship between stress and curvature (see section 3.8.2).

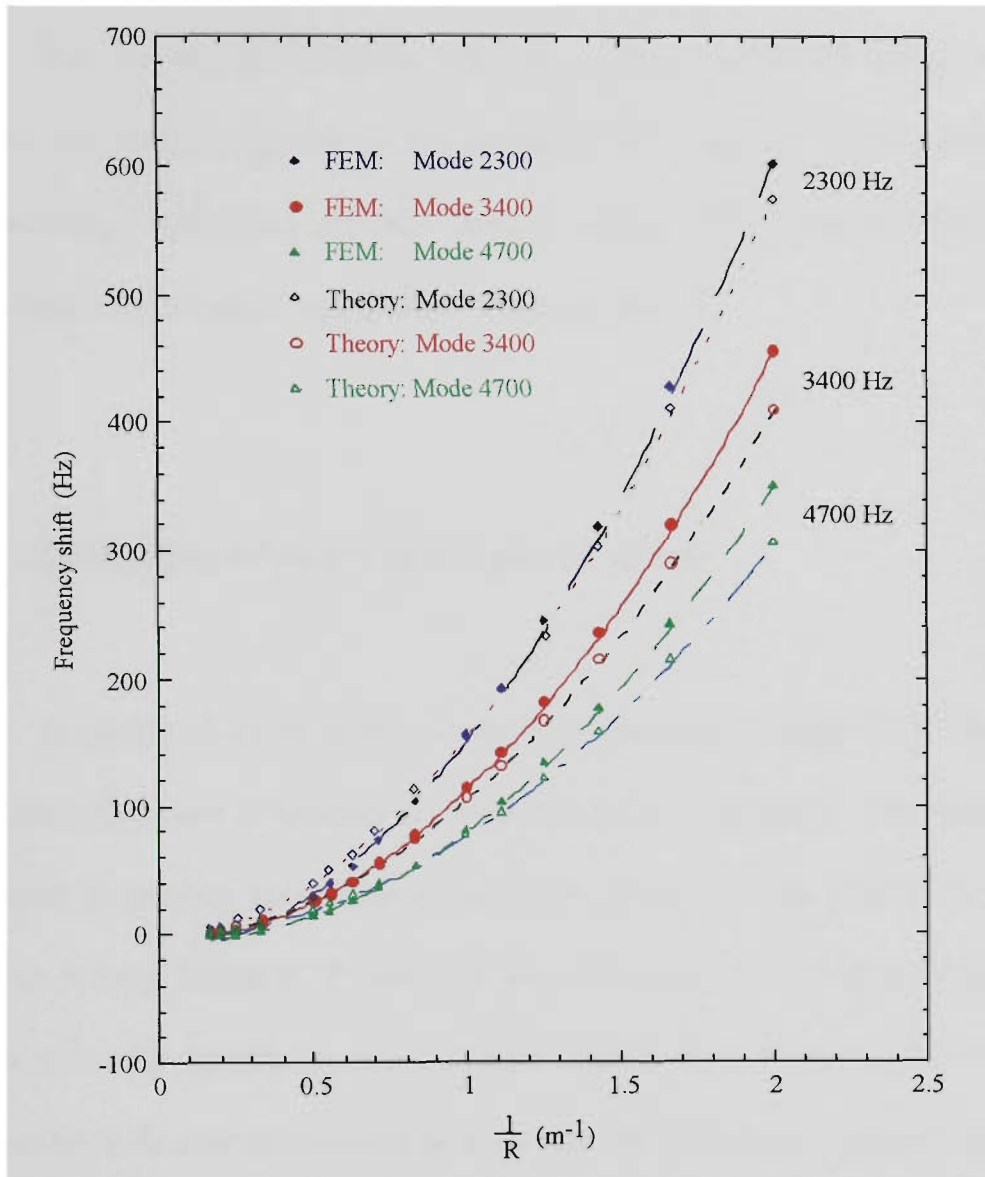


Figure 3.6 Variation of resonant frequencies for modes of about 2.3 kHz, 3.4 kHz and 4.7 kHz with inverse radius of curvature by FEM (open points) and theoretical calculations using equation 3.48 (solid points).

3.7 Stress and strain relationships

This section discusses the concepts of stress and strain which are used to characterise the elastic properties of the substrate-film structure. Stress and strain are defined and these definitions are then used in section 3.8 to obtain the relationship between stress and curvature for a shallow spherical shell.

3.7.1 Definition of stress and types of stress

A system of forces applied to the body produces a change in its dimensions. The fractional change in dimension is called the strain in the body. The force per unit area required to produce this strain is called the stress. If the surface of a solid is subjected to external forces P_1 , P_2 and P_3 as shown in figure 3.7, internal forces, denoted by F , will resist the deformation and maintain equilibrium. F will vary with position throughout the body and the intensity of this force (force per unit area) at a point is the stress at that point. Referring to figure 3.7, the resultant force on a small element of area ΔA , cut perpendicular to the x axis, at point Q is represented by ΔF , and components of ΔF along the x , y and z axes are ΔF_x , ΔF_y , ΔF_z . The stress components are defined as:

$$\sigma_x = \lim_{\Delta A \rightarrow 0} \frac{\Delta F_x}{\Delta A}, \quad \tau_{xy} = \lim_{\Delta A \rightarrow 0} \frac{\Delta F_y}{\Delta A}, \quad \tau_{xz} = \lim_{\Delta A \rightarrow 0} \frac{\Delta F_z}{\Delta A}, \quad (3.49)$$

where σ_x is the normal stress and τ_{xy} and τ_{xz} are the shear stresses. The normal stress is the intensity of a force perpendicular to a cut while the shear stresses are parallel to the plane of the element. By convention, normal stresses directed outward from the plane on which they act (i.e. tension) are considered as positive stresses and normal stresses directed towards the plane on which they act (i.e. compression) are considered to be negative stresses.

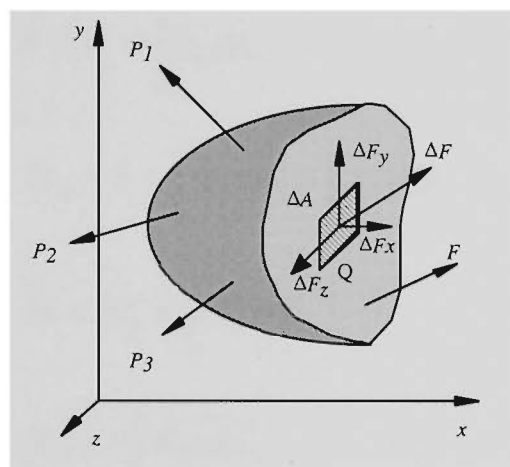


Figure 3.7 Stress components in a solid.

In general, there are three normal stresses σ_x , σ_y , σ_z , directed along the three principal axes. There are also six shears stresses τ_{xy} , τ_{yx} , τ_{zy} , τ_{yz} , τ_{zx} , τ_{xz} where the first subscript denotes the axis perpendicular to the plane on which the stress acts and the second provides the direction of the stress. In matrix form, the stress components appear as stress tensor

$$T = \begin{vmatrix} \sigma_x & \tau_{xy} & \tau_{xz} \\ \tau_{yx} & \sigma_y & \tau_{yz} \\ \tau_{zx} & \tau_{zy} & \sigma_z \end{vmatrix}. \quad (3.50)$$

Both the stress and internal force components are used to describe the internal state in a solid. For a bar cut perpendicular to the x axis, as shown in figure 3.8, the following relationships are valid (Pilkey, 1994):

$$F_x = P = \int_A \sigma_x dA, \quad (3.51)$$

$$V_y = \int_A \tau_{xy} dA, \quad (3.52)$$

$$V = V_z = \int_A \tau_{xz} dA, \quad (3.53)$$

$$M_x = T = \int_A \tau_{xz} y dA - \int_A \tau_{xy} z dA, \quad (3.54)$$

$$M = M_y = \int_A \sigma_x z dA, \quad (3.55)$$

$$M_z = - \int_A \sigma_x y dA. \quad (3.56)$$

Here σ is normal axial stress (σ_x), τ is shear stress, P is axial force, T is axial torque, V is vertical shear force (V_z) and M is bending moment.

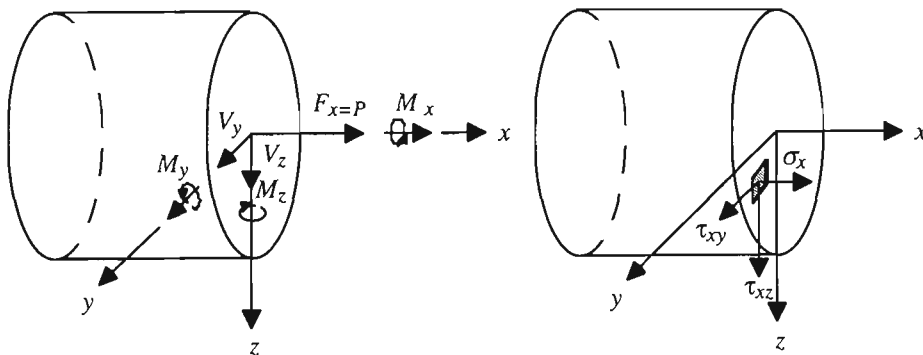


Figure 3.8 Internal forces and stresses in a solid bar.

3.7.2 Definition of strain

The application of external forces to an object can change the shape or size (or both). The extent of this deformation determines its strain. Such strains can be normal or shear. Normal strain is taken as positive when tensile forces elongates the object and negative when the compressive forces contracts the object. When a force F is applied along an object perpendicular to the cross section A as shown in figure 3.9(a), internal forces in the object resist the distortion. In this way the object attains an equilibrium in which its length is increased by an amount ΔL from its initial value L_0 . The tensile strain in this case is defined as the ratio of the change in length, to the original length

$$\epsilon_x = \frac{\Delta L}{L_0}. \quad (3.57)$$

When an object is subjected to a force F tangential to one of its surfaces while the opposite surface is held fixed a shear stress is developed in the object. If the object is a rectangular block, the shear stress results in a shape for which the cross-section is a parallelogram as shown in figure 3.9(b). Under the action of shear stresses, shear strains (γ) are induced. Shear strain is defined by the tangent of the shear distortion angle α in figure 3.9(b). In general, the dimensional changes at a point in a body is determined by six strains, $\epsilon_x, \epsilon_y, \epsilon_z, \gamma_{yx}, \gamma_{xz}$ and γ_{yz} .

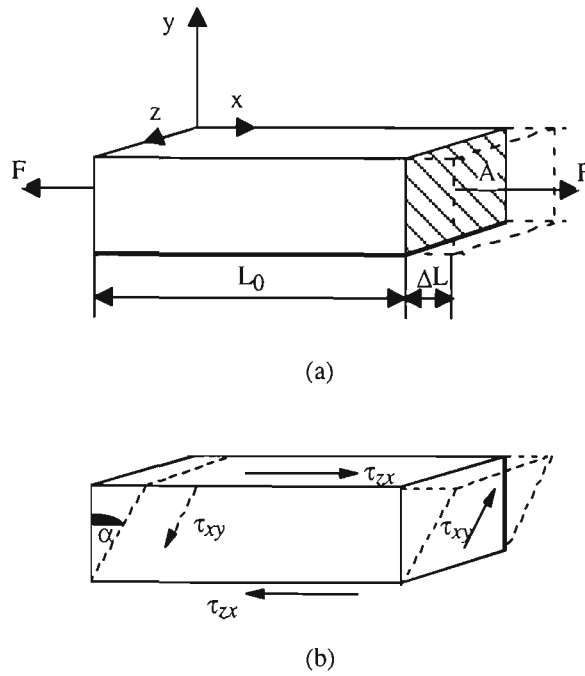


Figure 3.9 (a) Tensile force applied to a plate. (b) Distortion in a plate due to applied shear stress

For a bar of elastic material having the same mechanical properties in all directions and under uniaxial loading, measurements indicate that the lateral compressive strain is a fixed fraction of the longitudinal extensional strain. This fraction is known as Poisson's ratio ν and this relationship is expressed as

$$\epsilon_y = -\nu\epsilon_x. \quad (3.58)$$

Poisson's ratio is a material constant which can be determined experimentally. For metals it is usually between 0.25 and 0.35.

3.7.3 Elastic stress-strain relations

The stresses and strains are related to each other by properties of the material. In the elastic regime, all strains are small and Hook's law dominates the response of the system, so that for linear stresses

$$\sigma_x = E\varepsilon_x, \quad (3.59)$$

where E is Young's modulus. For a three-dimensional stress and strain, Hook's law for an isotropic material can be expressed as

$$\varepsilon_x = \frac{1}{E} \left[\sigma_x - \nu(\sigma_y - \sigma_z) \right], \quad (3.60)$$

$$\varepsilon_y = \frac{1}{E} \left[\sigma_y - \nu(\sigma_x - \sigma_z) \right], \quad (3.61)$$

$$\varepsilon_z = \frac{1}{E} \left[\sigma_z - \nu(\sigma_x - \sigma_y) \right], \quad (3.62)$$

$$\tau_{ij} = G\gamma_{ij} \quad (i, j = x, y, z). \quad (3.63)$$

Here G is the shear modulus. Volume changes are characterised by a bulk strain (change in volume divided by original volume) and a corresponding bulk modulus, K .

Of the many different material constants (e.g., E , ν , G , K) only two are independent for an isotropic solid and the relations between these constants are (Kaye and Laby, 1973):

$$G = \frac{E}{2(1 + \nu)}, \quad K = \frac{E}{3(1 - 2\nu)} = \frac{EG}{3(3G - E)}. \quad (3.64)$$

In the sections which follow, some of the previous formulas will be used in obtaining expressions relating stress in thin films to substrate deflection.

3.8 Relationship between stress in thin films and substrate deflection

The formulae that have been used in almost all experimental determinations to relate an average isotropic planar residual stress in a thin film to the resulting substrate curvature are variants of an equation given originally by Stoney (1909) as

$$\sigma_f = \frac{E_s t_s^2}{6R t_f}, \quad (3.65)$$

where t_f is the film thickness, R is radius of the substrate/film combination and E_s and t_s are the Young's modulus and the thickness of the substrate. This formula is applicable providing that the film thickness is very much smaller than the substrate thickness. However, in situations such as electrodeposition, the film thickness is often comparable to the substrate thickness and any difference in Young's modulus of a film and a substrate must be taken into account.

Brenner and Senderoff (1949) derived more general expressions which cover most common experimental situations. As has been pointed out (Hoffman, 1966; Davidenkov, 1961; Flinn, *et al.* 1987; Ohring, 1992), these derivations neglect the effect

of stress in two dimensions. When this is taken into account, the Young's modulus E_s needs to be replaced by the appropriate modulus for two dimensional deformation. The correct formula is then

$$\sigma_f = \frac{E_s t_s^2}{6(1-\nu_s)Rt_f}, \quad (3.66)$$

where E_s , t_s , R , t_f , are as defined previously and ν_s the Poisson's ratio for the substrate.

The average stress σ_f is defined by the relation (Klokholm, 1969)

$$\sigma_f = \frac{1}{t_f} \int_0^{t_f} \sigma_f(z) dz, \quad (3.67)$$

where $\sigma_f(z)$ is the stress distribution through the film thickness t_f . Experimentally, data is usually obtained for the product $\sigma_f t_f$ as a function of film thickness t_f and the average stress, σ_f , is then calculated from the slope of the line drawn from the origin to a point on the curve representing a given film thickness. Hence, it is convenient to rewrite equation 3.66 as

$$\sigma_f t_f = \frac{E_s t_s^2}{6(1-\nu_s)R}. \quad (3.68)$$

If the radius of curvature of the wafer before deposition of the film was R_0 than equation (3.64) could be modified to (Sahu, *et al.*, 1990 and Leusink, *et al.*, 1992)

$$\sigma_f t_f = \frac{E_s t_s^2}{6(1-\nu_s)} \left(\frac{1}{R} - \frac{1}{R_0} \right), \quad (3.69)$$

where R is radius of curvature of the wafer after deposition of a thickness t_f of thin film.

Equation 3.69 is sufficiently accurate for the most calculations of the stress in thin films and it is valid under the following conditions:

- (a) The substrate is linearly elastic, homogeneous and uniformly thick.
- (b) The bending displacement is small as compared with the thickness of the substrate.
- (c) The stress is uniform throughout the film thickness.
- (d) No stress relief or changes in elastic constants take place as the film is built up.
- (e) The ratio t_f / t_s must be $\leq 10^{-3}$. With $t_f / t_s \geq 10^{-2}$ and the ratio of Young's modulus of film to that of the substrate > 1 , the error in equation 3.68 can be as large as 20% (Brenner and Senderoff, 1949).

In the following section the formulas for relationship between stress in the films and substrate deflection for film/substrate system will be derived.

3.8.1 Determination of the stress in thin films

In deriving the equations for stress in the films, three cases will be considered:

1. $E_f = E_s = E$ $t_f \ll t_s$

2. $E_f = E_s = E$ t_f - is thick ($t_f > 1\mu$)
3. $E_f \neq E_s$ t_f - thick film

Case 1

It is assumed initially that the stress is anisotropic, $E_{film} = E_{substrate} = E_s$, $t_f \ll t_s$ and that the neutral axis lies in the middle of the substrate. Further, when the beam is deformed the radius of curvature of the upper surface of the substrate/film system is assumed to be the same as that of the lower surface (i.e. $R \gg t_f$).

Consider the element of thickness dz at a distance z from the neutral axis as shown in figure 3.10 (c). The strains ϵ_x and ϵ_y in the x and y directions are given by

$$\epsilon_x = \frac{z}{R_x} \quad \text{and} \quad \epsilon_y = \frac{z}{R_y} \quad (3.70)$$

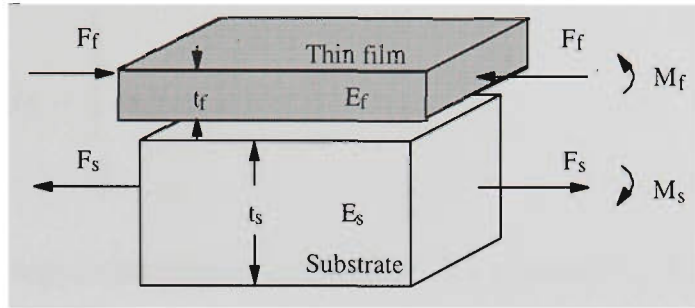
where R_x and R_y are radii of curvature of the substrate in x and y directions. The stress and strain are related to each other by the properties of the material and for the case of an elastic substrate equations 3.60 and 3.61 become:

$$\epsilon_x = \frac{1}{E_s} (\sigma_x - \nu \sigma_y), \quad (3.71)$$

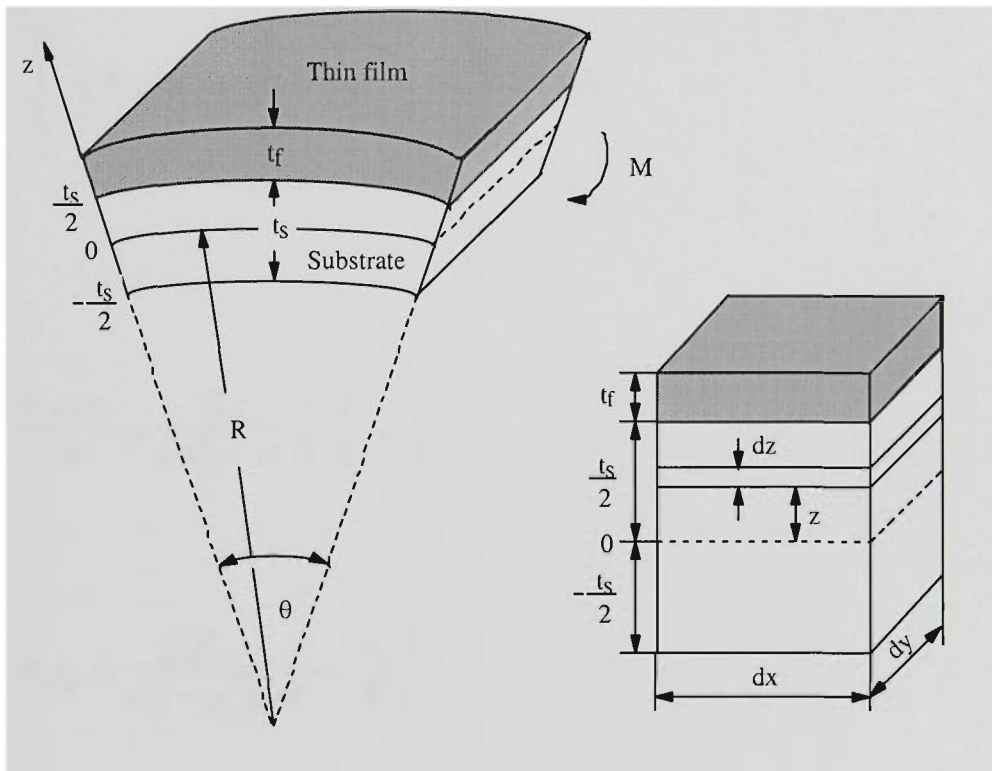
$$\epsilon_y = \frac{1}{E_s} (\sigma_y - \nu \sigma_x), \quad (3.72)$$

where σ_x and σ_y are the stress components in x and y direction.

Solving equation 3.70, 3.71 and 3.72 for σ_x and σ_y we obtain



(a)



(b)

(c)

Figure 3.10 Stress analysis of film-substrate structure: (a) composite structure; (b) elastic bending of structure under applied end moment. (c) an element of cross section of substrate/film structure.

$$\sigma_x = \frac{E_s z}{1 - \nu^2} \left(\frac{1}{R_x} + \frac{\nu_s}{R_y} \right) \quad \text{and} \quad \sigma_y = \frac{E_s z}{1 - \nu^2} \left(\frac{1}{R_y} + \frac{\nu_s}{R_x} \right). \quad (3.73)$$

Taking moments about the neutral axis, as shown in figure 3.10 (c), of film/substrate structure (equation 3.55, $M_f = M_s$) gives:

$$\int_{\frac{t_s}{2}}^{\frac{t_s+t_f}{2}} \frac{t_s}{2} \sigma_{fx} dA = \int_{-\frac{t_s}{2}}^{\frac{t_s}{2}} \sigma_x z dA , \quad (3.74)$$

where σ_{fx} is the stress in the film in x direction. By substituting for σ_x from equation 3.73 and using $dA=dzdy$, equation 3.74 becomes:

$$\int_{\frac{t_s}{2}}^{\frac{t_s+t_f}{2}} \frac{t_s}{2} \sigma_{fx} dzdy = \int_{-\frac{t_s}{2}}^{\frac{t_s}{2}} \frac{E_s z}{1-\nu_s^2} \left(\frac{1}{R_x} + \frac{\nu_s}{R_y} \right) z dzdy . \quad (3.75)$$

Hence

$$\frac{\sigma_{fx} t_s t_f}{2} = \frac{E_s t_s^3}{12(1-\nu_s^2)} \left(\frac{1}{R_x} + \frac{\nu_s}{R_y} \right) , \quad (3.76)$$

and

$$\sigma_f t_f = \frac{E_s t_s^2}{6(1-\nu_s^2)} \left(\frac{1}{R_x} + \frac{\nu_s}{R_y} \right) . \quad (3.77)$$

The y component of stress in the film, σ_{fy} is

$$\sigma_{fy} t_f = \frac{E_s t_s^2}{6(1-\nu_s^2)} \left(\frac{1}{R_x} + \frac{\nu_s}{R_y} \right) . \quad (3.78)$$

If there is stress isotropic, $\sigma_{fx} = \sigma_{fy} = \sigma_f$ and $R_x=R_y=R$ then equations 3.77 and 3.78 become

$$\sigma_f t_f = \frac{E_s t_s^2}{6(1-\nu_s)R} \quad (3.79)$$

for a single film. If several films are present then the interaction of each film with substrate can be treated separately. The total bending of the substrate is simply a linear combination of the bending contributions of the films determined separately (Flin, 1989). To determine the stress in a particular film the inverse radius of curvature must be determined with and without that film. This change in $1/R$ is then used in equation 3.73 to calculate the average stress in that film, therefore equation 3.69 should be used for multilayer films.

Case 2

Here it is assumed that $E_{film} = E_{substrate} = E_s$ and the film thickness, t_f , is not negligible in comparison with the thickness of the substrate, t_s . The neutral axis will now be at a distance $(t_s + t_f)/2$ from the bottom of the substrate. Considering isotropic stress, and taking moments as in *Case 1*:

$$\int_{\frac{t_s - t_f}{2}}^{\frac{t_s + t_f}{2}} \sigma_f z dz = \int_{\frac{t_s - t_f}{2}}^{\frac{t_s + t_f}{2}} \sigma z dz \quad (3.80)$$

where $\sigma = \sigma_x = \sigma_y$ is the stress developed in the substrate.

Using the simplified form of equation 3.73 (for the case $R_x = R_y = R$),

$$\sigma = \frac{E_s z}{(1 - \nu_s) R}, \quad (3.81)$$

and integrating equation 3.80 we finally obtain

$$\sigma_f t_f = \frac{E (t_s + t_f)^3}{6 t_s (1 - \nu) R} \quad (3.82)$$

This equation is identical to Brenner and Senderoff's equation (9), but differs from Davidenkov's (1961) equation (2), which is

$$\sigma_f t_f = \frac{4E(t_s + t_f)^2}{6R}. \quad (3.83)$$

The origin of this difference lies in the simplified expression for bending moment used in derivation of equation 3.82. Equation 3.82 reduces to equation 3.79 when $t_s \gg t_f$.

Case 3

When the substrate and the coating have different elastic moduli, $E_f \neq E_s$, and the film thickness is not negligible in comparison with the thickness of the substrate, the neutral axis no longer passes through $(t_s + t_f)/2$. The position of the neutral axis must be found by resolving forces. If it is assumed that the neutral axis is a distance z_0 from the bottom of the substrate. Then resolving forces, using equation 3.55, gives

$$\int_0^{z_0} E_1 z dz - \int_0^{t_s - z_0} E_1 z dz + \int_{t_s - z_0}^{t_s - z_0 + t_f} E_2 z dz = 0, \quad (3.84)$$

where $E_1 = \frac{E_s}{1 - \nu_s}$, and

$$E_2 = \frac{E_f}{1 - \nu_f}.$$

As before, ν the Poisson's ratio and the subscripts s and f refer to substrate and film respectively.

From equation 3.84 we get

$$z_0 = \frac{t_s}{2} \left[\frac{1 + 2E_r t_r + E_r t_r^2}{1 + E_r t_r} \right], \quad (3.85)$$

where $E_r = E_2/E_1$ and $t_r = t_f/t_s$. The assumption about the position of the neutral axis made for *case 1* and *case 2* may now be verified by putting $E_r=1$ in equation 3.85. This is identical to the result of Davidenkov (1961) who, also, derived the following expression for stress in thin film:

$$\sigma_f = \frac{E_s t_s}{6(1-\nu_s)R t_f \int_0^{t_f} \frac{(1 + 2t_r + E_r t_r^2)}{1 + 4E_r t_r + 6E_r t_r^2 + 4E t_r^3 + E_r^2 t_r^4} dt_f} . \quad (3.86)$$

The integral in the denominator of this equation cannot be expressed analytically and therefore numerical integration must be used for the final solution. If the term $E_r^2 t_r^4$ is neglected in comparison with terms of lower order in t_r , then the expression may be integrated by expanding the dominator in the integral as a binomial. The result of this integration is:

$$\sigma_f t_f = \frac{E_s t_s^2}{6(1-\nu_s)R \left[1 + (1 - 2E_r) t_r + \frac{E_r}{3} (16E_r - 13) t_r^2 - (4E_r - 19E_r^2 + 16E_r^3) t_r^4 \right]} . \quad (3.87)$$

This formula reduces to equation (3.79) when $t_s \gg t_f$.

The effect of the difference in elastic moduli is negligible when $t_s \gg t_f$, but may be significant with thicker coatings (Brenner and Senderoff, 1949). The relations given in equations (3.79) and (3.87) are only accurate for very small substrate deflections, at least an order of magnitude less than the substrate thickness (Harper and

Wu, 1990). Deflections of the order of the substrate thickness, or larger, provide measurement advantages, but require higher-order analytical relations. A partially nonlinear stress-curvature relation was developed for analysing the stress in an isotropic thin film deposited on the substrate (rectangular) undergoing large deflections (Harper and Wu, 1990; Masters and Salamon, 1993). It was shown that the nonlinear geometric effect may be responsible for some of the discrepancies which have appeared in the literature where different investigators have reported significantly different stress in the same film material. Nevertheless, in the present work $t_s \gg t_f$ ($t_f < 2 \times 10^{-3}$ for Cr films and $t_f < 4 \times 10^{-3}$ for MgF_2 films) and equation (3.79) has been used to evaluate stresses in thin films.

3.8.2 Relationship between stress in a film and measured resonant frequency of the curved substrate/film combination

From equation 3.48 the inverse radius of curvature can be expressed as

$$\frac{1}{R} = 2\pi \sqrt{\frac{\rho(f_{mn(s)}^2 - f_{mn(p)}^2)}{E_s}} \quad (3.88)$$

Combining this equation with equation 3.79, the relationship between average stress, thin film thickness and measured resonant frequency of the curved substrate/film combination is given by

$$\sigma_f = \frac{\pi t_s^2}{3(1-\nu_s)t_f} \sqrt{E_s \rho (f_{mn(s)}^2 - f_{mn(p)}^2)} . \quad (3.89)$$

Thus it is clear that the average stress in a film can be determined by measuring the change in resonant frequency which arises when a flat test substrate is curved by the stress in the deposited film layer. This is the basis of the method for measuring stress in thin films developed in the course of the work described in this thesis.

3.8.3 The effect of the coating material on resonant vibration frequencies of a flat glass/film composite structure

Up to present, the equations for the frequency shifts associated with the coating have all been derived with the implicit assumption that the thickness and mass of coating are negligible in comparison with that of the substrate and the only effect is to produce a curvature due to the stress. However, as can be seen from some of the previous analytic expressions, the addition of a coating, even without any stress or curvature change, will give rise to a small resonant frequency change due to the change in total thickness.

In this section the effect of the thickness and Young's modulus of the thin film on the resonant frequency of a flat substrate/film composite structure will be considered. According to the equation 3.40 the allowed values of the resonant frequency

of a flat plate depends on its thickness, density and Young's modulus. For a structure comprising a substrate and coated film, a composite beam analysis needs to be employed to determine the stiffness and resonant frequencies of the entire structure. To our knowledge, no exact analytical expression has been obtained for the particular geometry and mounting arrangement used in the work described in this thesis. However, an expression has been obtained for the case of a simple cantilever and this may be used to obtain approximate values of the frequency shifts caused by the coating in absence of bending due to stress (Walsh and Culshaw, 1991). In this treatment, the resonant frequency of the substrate/film combination, $f_{mn(sf)}$, is related to that of the uncoated substrate, $f_{mn(s)}$ by

$$\frac{f_{mn(sf)}}{f_{mn(s)}} = \sqrt{\Psi} \quad (3.90)$$

where Ψ is

$$\Psi = \frac{4 + 6\frac{t_f}{t_s} + \frac{E_s t_s}{E_f t_f} + 4\left(\frac{t_f}{t_s}\right)^2 + \frac{E_f}{E_s}\left(\frac{t_f}{t_s}\right)^3}{\left(1 + \frac{E_s t_s}{E_f t_f}\right)\left(1 + \frac{\rho_f t_f}{\rho_s t_s}\right)}. \quad (3.91)$$

Here the subscripts s and f refer to the substrate and film respectively and t , E and ρ are, as before, the thickness, Young's modulus and density. The factor Ψ takes into account the extra mass and also the mechanical properties of the film on the resonant frequency of the combined structure even if there is no stress at the film-substrate boundary. In order to include the physical properties of the glass/film composite structure used in this work, equation 3.48 could be re-written as

$$f_{mn(s)}^2 = f_{mn(p)}^2 \Psi + \frac{E}{4\pi^2 \rho R^2} \quad (3.92)$$

Table 3.7 shows the values of $\sqrt{\Psi}$ for both Cr and MgF₂ films calculated for a range of film thicknesses typical of the experimental data. The used values for Young's modulus are: $E_{\text{glass}}=7.2 \times 10^{10}$ Pa, $E_{\text{Cr}}=2.48 \times 10^{11}$ Pa and $E_{\text{MgF}_2}=1.17 \times 10^{11}$ Pa. The data shows that in absence of stress, the coating has only a small effect on the resonant frequency. However, when one is measuring frequency shifts, this effect can be a significant fraction of the shift. This matter will be addressed further when the experimental data is presented in chapter 5. In a situation where plate curvature cannot be measured and stress must be inferred from frequency shift alone, this effect needs to be considered. From Table 3.7, the variation in unstressed resonant frequency due to the addition of a film should be less than 0.61% for Cr and 0.66% for MgF₂.

Table 3.7 Calculated factor Ψ (using equation 3.91) for film thicknesses up to 200 nm for chromium and 400 nm for magnesium fluoride.

t_f (nm) for Cr	14.8	37.4	62.8	84.8	107.5	129.8	152.4	181.9
$\Psi^{1/2}$ (Cr film)	1.0005	1.0013	1.0021	1.0029	1.0036	1.0044	1.0051	1.0061
t_f (nm) for MgF ₂	15.0	52.4	100.7	157.7	213.5	267.8	329.5	396.2
$\Psi^{1/2}$ (MgF ₂ , film)	1.0002	1.0009	1.0017	1.0026	1.0036	1.0045	1.0055	1.0066

3.9 Summary

General analytical expressions for resonant modal frequencies modes for a flat circular plate, supported in the center, was derived and first nine 3D modes shapes were plotted. The analytic expression for the resonant modal frequencies of a flat plate was then extended to cover the case of a shallow spherical shell. An expressions was obtained for the modal frequencies of such a shell as a function of the radius of curvature. It was shown that the modal resonant frequencies of flat plates calculated from the analytic expressions are in agreement with those obtained using FEM analysis and with experimental measurements. Similarly, agreement was obtained between the calculated and FEM-determined resonant frequencies for the shallow spherical shells. Equations were also derived which relate the curvature of a substrate/film combination to the stress in the film. The equations relating both resonant frequency and stress to curvature were then combined to obtain an expression relating the stress in the film to the frequency changes of the resonant modes. This equation is the basis of the method for measuring stress in thin films developed in the course of the work described in this thesis.

Experimental methods

4.1 Introduction

This chapter describes the experimental methods developed for measurement of stress variations in thin films. Two types of measurement are described. In the first, the samples are coated in a vacuum system and then removed for stress measurements under room conditions. A second set of measurements was made inside the vacuum coating system, both during and subsequent to coating. This chapter also describes the vacuum deposition system which was modified and adapted for this work, the method of sample preparation and the calibration of the thickness monitoring system. Standard optical lever measurements were made to provide an independent measurements of the film/substrate system for samples studied outside the evaporation chamber (these measurements are not feasible inside the evaporation system). This chapter also includes a detailed description of the design and construction of the optical systems used to remotely excite mechanical vibrations and to measure the resonant frequencies.

4.2 Coating thin films

Thin films of materials such as metals, semiconductors, oxides and sulphides can be obtained in the crystalline or amorphous state by condensation of the vapour on a substrate. The mechanism involved in forming the thin film may be simple condensation or may involve chemical reactions. Films can be produced by physical vapour deposition (namely evaporation and sputtering methods) or chemical vapour deposition (CVD).

Thin films obtained by physical vapour deposition are usually made at pressures varying between an upper limit of 10^{-4} to 10^{-6} Pa and a lower limit set by the pressure value that modern vacuum technology can attain. High purity films are best produced at very low pressure with deposition rates high enough to prevent contamination during coating. Substrate distances should be less than the mean free path of the gas particles to reduce the incorporation of residual gas particles in the thin film.

Deposition of films by thermal evaporation is one of the simplest methods used. In this method a film is deposited by the condensation of the vapour on a substrate, which is maintained at a lower temperature than that of the vapour. All materials evaporate when heated to sufficiently high temperatures. Methods used to evaporate these materials include resistive, radio frequency (rf) or laser heating and electron bombardment (e-gun).

4.2.1 Description of vacuum system

Vacuum systems can be classified according to the pressure range in which they operate as rough, low, high, very high and ultra high vacuum. The level of vacuum required depends on the specific deposition methods being used and the required freedom from contaminants.

A conventional high vacuum bell-jar evaporation system as shown schematically in Figure 4.1 was used in our experiments. The main pumping chamber consisted of a cylindrical metal bell-jar (1) of diameter of 680 mm and the height 310 mm. This chamber was pumped down using a 60 l/min mechanical pump (3) and a 250 mm diameter diffusion pump (4). The mechanical pump is used in the initial or 'roughing' phase of the pump-down. During this phase the roughing valve (5) is open, while the high-vacuum isolation valve (6) and the backing valve (7) are closed, isolating the diffusion pump. Thus the flow of gas during roughing is from the vessel (bell-jar) through the roughing line and out to the exhaust of the mechanical pump (8). When the pressure as indicated by the Pirani gauge (9) is sufficiently low (less than 10 Pa) the roughing valve is closed and the high-vacuum isolation valve and the backing valve are opened, putting the diffusion pump in "circuit". The flow of gas is now from the bell-jar, through the high-vacuum manifold, the diffusion pump, the foreline (10), the mechanical pump and out to the mechanical pump exhaust. The mechanical pump is now being used as a "backing pump", pumping on the exhaust of the diffusion pump, which cannot exhaust its

gases to atmospheric pressure. The water-cooled baffle (11), near the inlet of the diffusion pump, reduces back streaming from the diffusion pump. To evaporate the

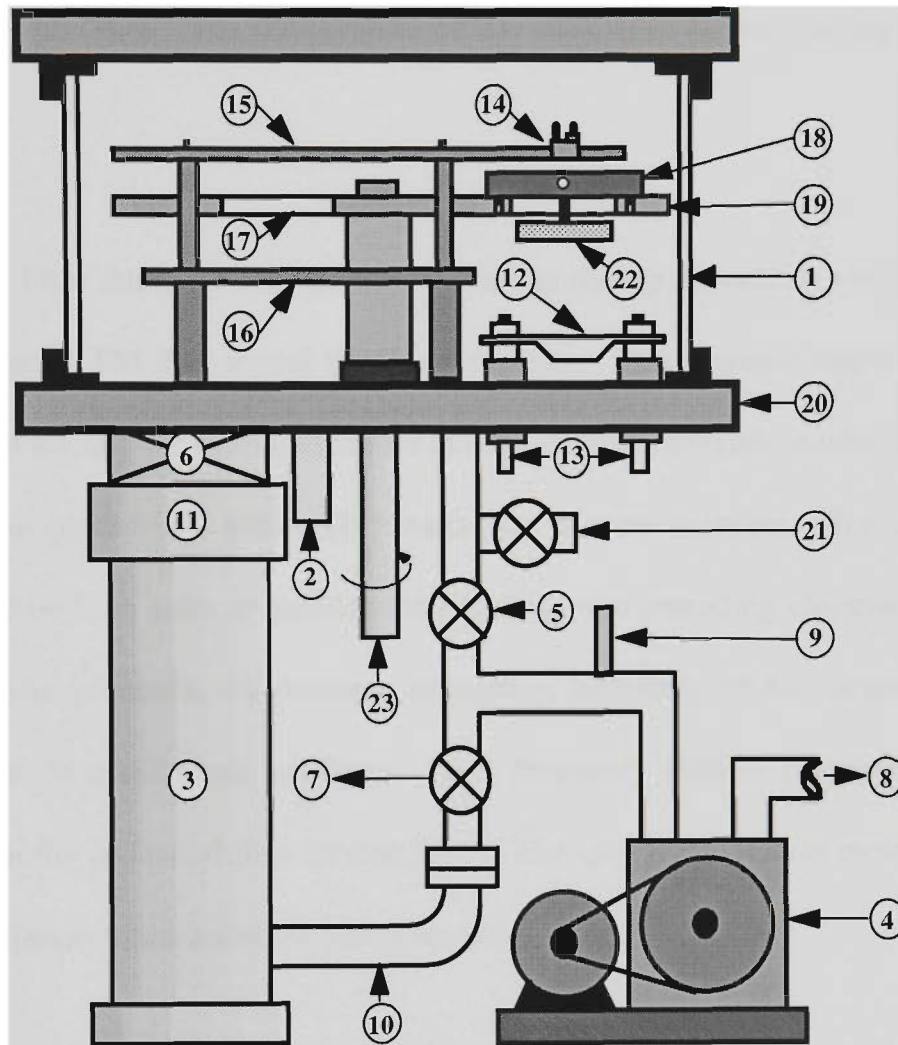


Figure 4.1 High vacuum system. (1) Bell-jar; (2) High-vacuum gauge; (3) Diffusion pump; (4) Mechanical pump; (5) Roughing valve; (6) High-vacuum isolation valve; (7) Backing valve; (8) Exhaust line; (9) Gauge; (10) Foreline; (11) Baffle; (12) Evaporation boat; (13) High current leads; (14) Thickness sensor; (15, 16) Stationary aluminium plate; (17) Slot; (18) Sample holder; (19) Rotating plate; (20) Base plate; (21) Vacuum release valve; (22) Glass substrate; (23) Rotation shaft.

film, indirect resistance heating was used. The evaporation material is placed in a boat (12) made of tungsten (for evaporation of Cr) or tantalum (for evaporation of MgF_2). The boat, clamped between water cooled electrodes (13), is heated by

electrical current flow and the material is evaporated on the substrate. The roughing pressure (down to 10^{-1} Pa) and total pressure were measured by means of Pirani and Penning gauges, respectively. All depositions were carried out at about 10^{-4} Pa residual gas pressure. The temperature of the substrates during coating was about 25°C.

Film thickness and the deposition rate during deposition were monitored using a Maxtek TM-200 crystal thickness monitor. This monitor displays the film thickness in kÅ and the evaporation rate in Å/s. A quartz crystal (oscillating at about 6 MHz) was placed in a holder (14) inside the vacuum chamber. The crystal was gold plated on both sides to provide long lasting, non-corroding electrical contacts. As deposition proceeds, the resonant oscillation frequency of this crystal changes with respect to a reference oscillator. This frequency shift is proportional to the thickness of the deposited film for thin films. The quartz crystal was mounted above the boat adjacent to the substrate being coated.

The substrate holder can hold seven substrates during the coating process as shown in Figure 4.2. The slot (16) for the quartz crystal on the substrate holder was designed in a such a way as to compensate for the geometry-dependent difference between deposition rate on the substrate and the rate on the thickness monitor crystal. The speed of rotation of the substrate holder, during deposition, was 60 rpm. Substrate rotation was used for all measurements except those where temperature and real-time deposition effects were being investigated. During these measurements, the substrate was stationary.

4.2.2 Chamber cleaning techniques

The vacuum system interior must be clean to achieve operating pressures of 10^{-4} Pa or better in reasonable times and to prevent contamination of the

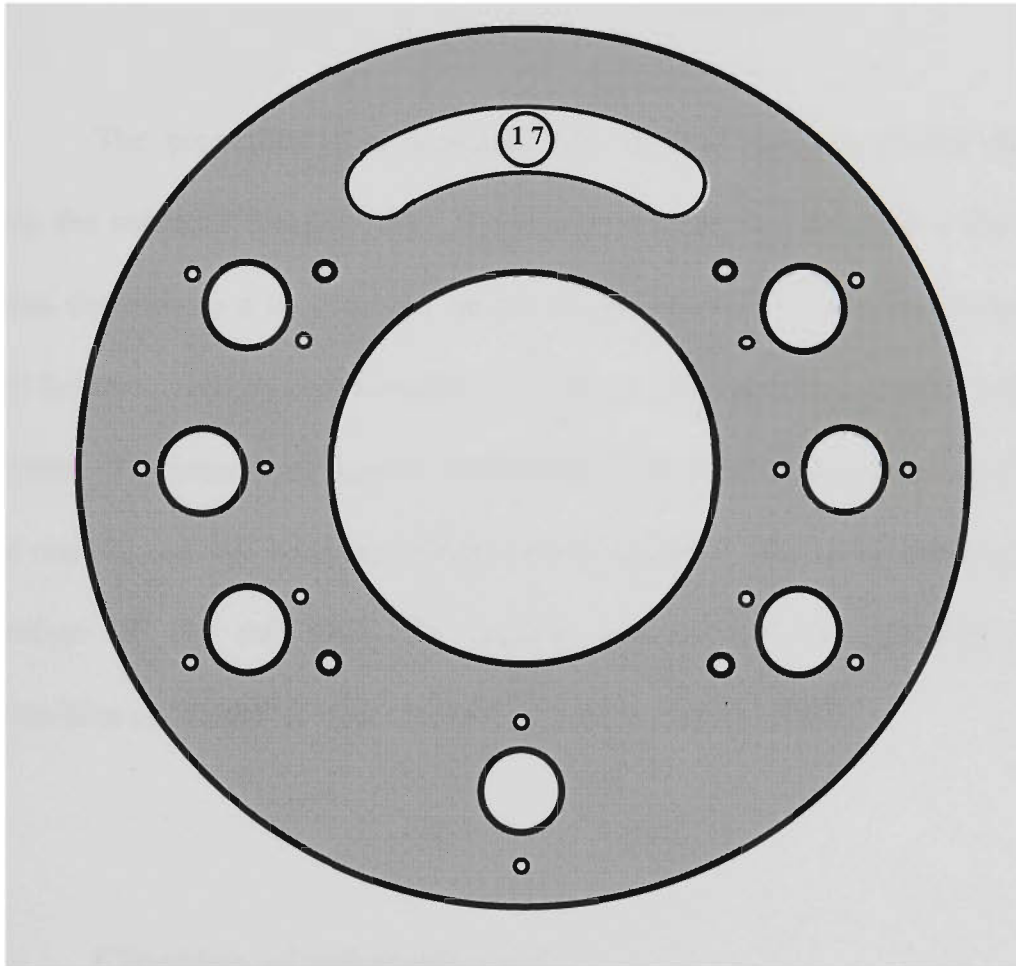


Figure 4.2 Aluminium rotation substrate holder. The slot (17) is to allow deposition on the crystal monitor.

evaporated films. Visible contaminants such as deposits of coating materials were removed by rubbing with emery cloth. This method is limited to robust components. Delicate parts (ceramics, glasses and polished surface) were wiped with a clean lint-free cloth as a preliminary step. Ethyl alcohol is very effective for removing water

and trichloroethylene is used to remove oil and fingerprints from vacuum components.

4.3 Sample preparation

The properties of a deposited film depend strongly on the adherence between the substrate and the film. The quality of adhesion between a film and its substrate depends to a large extent on the condition of the interfacial layer that is formed between coating and substrate and this is influenced by a large number of parameters. The interfacial bonding is strongly dependent on the choice of materials for the coating and the substrate. Other factors affecting interfacial bonding are the preparation of the substrate, the coating process and the handling of the substrate/film combination after the coating process is completed.

4.3.1 Cleaning of substrate surface

The substrates used to test our technique were circular glass plates of diameter 42 mm and thickness 0.11 mm as shown in Figure 4.3. Before a glass plate can be coated with a thin film, all unwanted contamination must be removed from the surface. If the substrate surface is not clean, then the film will not adhere well or may not adhere at all. The adhesion properties of the deposited film depend strongly

on the effectiveness of cleaning the substrates. The cleaning of the surface is important but is also a very delicate operation with those very thin substrates.

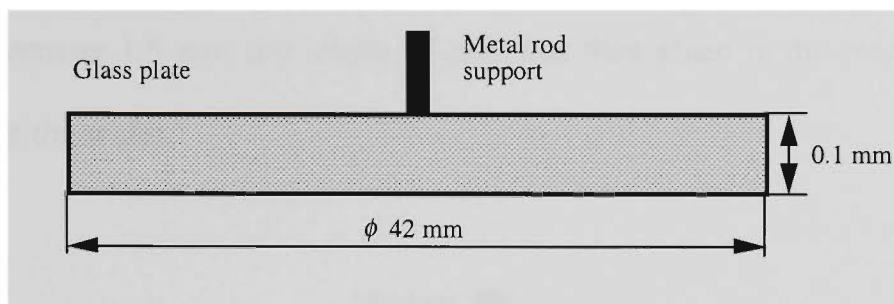


Figure 4.3 The substrate used in experiments.

There are a number of cleaning techniques used in scientific and industrial environments. Cleaning with solvents is a widespread procedure that is always included whenever cleaning of a glass surface is needed. Our glass samples were cleaned using the process developed by Kern and Poutinen (1970) for the semiconductor industry. To remove organic contaminants the wafers were soaked in hot trichlorethylene for 15 minutes. Two solutions are then used sequentially to remove ionic and atomic contaminants:

- 1) The first solution was composed of a mixture of 5:1:1 by volume of filtered deionised water, H_2O_2 and ammonium hydroxide (NH_4OH). This solution is used for 15-20 minutes at 75 - 85°C followed by a rinse in deionised water.
- 2) The second solution contained a 6:1:1 by volume mixture of filtered deionised water, H_2O_2 and HCl. This solution is used for 15-20 minutes at a temperature of 75 - 85°C followed by a rinse in deionised water.

The H_2O_2 used was the unstabilized electronic grade. The wafers were then dried in a vacuum furnace at a temperature of 90°C for 90 minutes. The clean wafer was then placed in the aluminium holder as shown in Figure 4.4. A thin steel rod of diameter 1.5 mm and length 25 mm was then glued in the centre of the rear surface of the wafer.

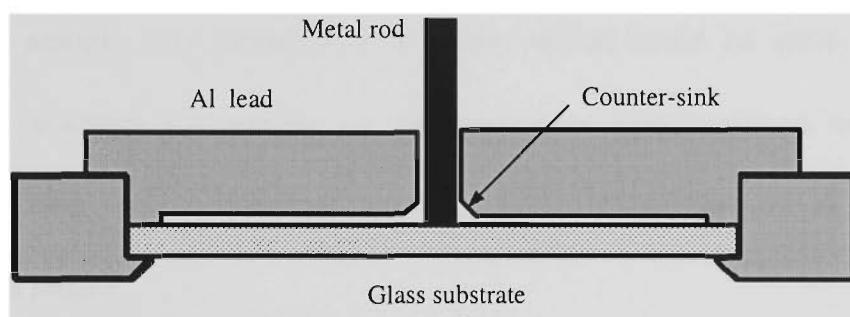


Figure 4.4 The jig used to glue the metal rod to the centre of the substrate.

4.3.2 The evaporants

Evaporation materials which were used included chromium, magnesium fluoride and titanium. The chromium used for evaporation was supplied by CERAC in 3-6 mm pieces and of 99.99% purity. Spectrographic analysis showed that it contains less than 0.001 % of Ca, Mg and Si and less than of 0.0003 % of Fe. The magnesium fluoride was supplied by SIGMA ALDRICH in 3-6 mm pieces and of 99.9% purity and titanium by PURE TECH as a plate of diameter 50.8 mm and thickness 3.175 mm. The spectrographic analysis of these evaporants is shown in Appendix A.2.

4.3.3 Actual coating procedure

Usually, the curvature of a coated wafer is not completely uniform because of the local variations of residual stress developed after deposition (Flinn, 1989). It is important for reproducible measurements that the same positions are always used for LD excitation and curvature measurements. To ensure that this was the case the sample was mounted in a holder which could be easily placed in a reproducible position for coating or measurement. Once placed in this holder (Figure 4.5), the sample was not removed until completion of all coating and measurement steps.

The sample, mounted in its holder, was then placed in a diffusion pumped vacuum chamber, the pressure was reduced to 2×10^{-4} Pa and the sample was coated with first layer of about 10 nm chromium at a deposition rate of 10 Å/sec. The sample was then removed from the chamber and the curvature and resonant mechanical vibrations were measured.

After measurement, the sample was replaced in the vacuum chamber and additional layers of a thin film were deposited. Measurements were made on the composite structure after each successive deposition until the glass plate had ten layers of deposited material.

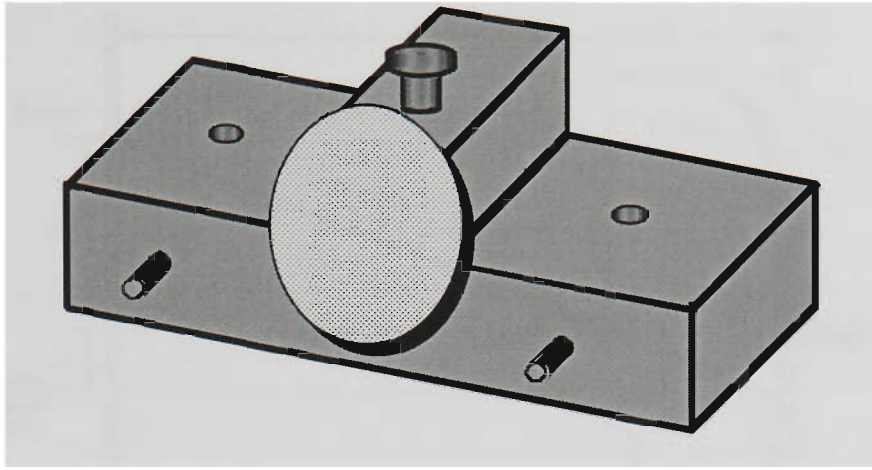


Figure 4.5 The holder used to hold the sample during deposition of thin film and measurement.

4.4 Curvature measurement

The flat glass plate coated with a chromium thin film is transformed to a concave spherical mirror due to the stress, as shown schematically in Figure 4.6. The sample has a radius of curvature R and the center of the curvature is located at point C . The principal axis connects the points C and S , where S is the centre of the spherical segment. When a laser source is placed on the principal axis at point O and the sample is translated by a distance Δx in the x direction than the resulting translation of the reflected beam on the screen is Δd . From simple geometry it is readily shown that the radius of the concave sample is given to a good approximation, by

$$R \approx 2L \frac{\Delta x}{\Delta x + \Delta d} . \quad (4.1)$$

the beam spot on the screen of approximately 6 mm (for the flat plate). The translation of this spot (Δd) could be measured to within about 1 mm. Also, since the wafer is generally not uniformly curved, the average radius of curvature is obtained by making the measurement over a range of Δx values by translating the mirror. The curvature and its standard error are then obtained by fitting equation 4.1 to the data. Using this method, the lever technique can give the average radius of curvature with an uncertainty of approximately 2.5%.

4.5 Calibration of the film thickness monitor

The thickness of an individual film is an extremely important parameter which figures in practically all equations used to characterise thin films. The physical thickness is the step height between the substrate surface and the film surface. Measurement of film thickness obviously cannot be accomplished in a manner which does not affect the film using conventional methods for length determination but requires special methods. A remarkable number of different, often highly sophisticated, film thickness measuring methods have been developed and are well reviewed in Maissel *et al.* (1970). Two beam interferometry is applicable to all types of films and it has a high accuracy and also represents the most reliable measuring method for the calibration of other techniques. This method, described by Tolansky (1955) is based on measuring the distance between the interference fringes formed by the multiple reflection of a beam of monochromatic light (often a sodium

or mercury lamp) between a highly reflective film and a specially-coated Fizeau plate which makes contact with the specimen at a slight angle and forms an air wedge (Figure 4.7). The film must end with a sharp edge to achieve maximum quality (sharp, high contrast, narrow) fringes. For such fringes, the film and substrate must be coated with a highly reflective surface material.

The film thickness t_f is obtained by measuring the spacing ΔL and displacement ($L-\Delta L$) of the lines:

$$t_f = \frac{\Delta L}{L} \frac{\lambda}{2}.$$

Our thickness monitor was calibrated using an Angstrometer (model Nos. 980-4000 produced by VARIAN-Vacuum Division) using monochromatic light from a sodium vapour lamp ($\lambda = 589.6$ nm). Suitable calibration samples were formed on flat glass slides. The slides were prepared under similar conditions to the thin film samples used in measuring the mechanical vibrations by the interferometric technique. This means that the slides were cleaned using the procedure described in section 4.3.1. Initially, all slides were coated with a 100 nm thick layer of chromium to provide a flat and highly reflective surface. Then the slides were removed from the vacuum chamber. A thin plate, made of brass shim, was then placed in contact with the coated slide in a slide holder (Figure 4.4) in a such way as to mask half of the slide. Then, all three slides were separately coated with different thicknesses of chromium. The film thicknesses were measured using the Angstrometer and these thicknesses were compared with the quartz thickness monitor readings. The stated

resolution of the Angstrometer is better than ± 3 nm throughout the range of 30-2000 nm, so the calibration uncertainties were mostly due to random errors.

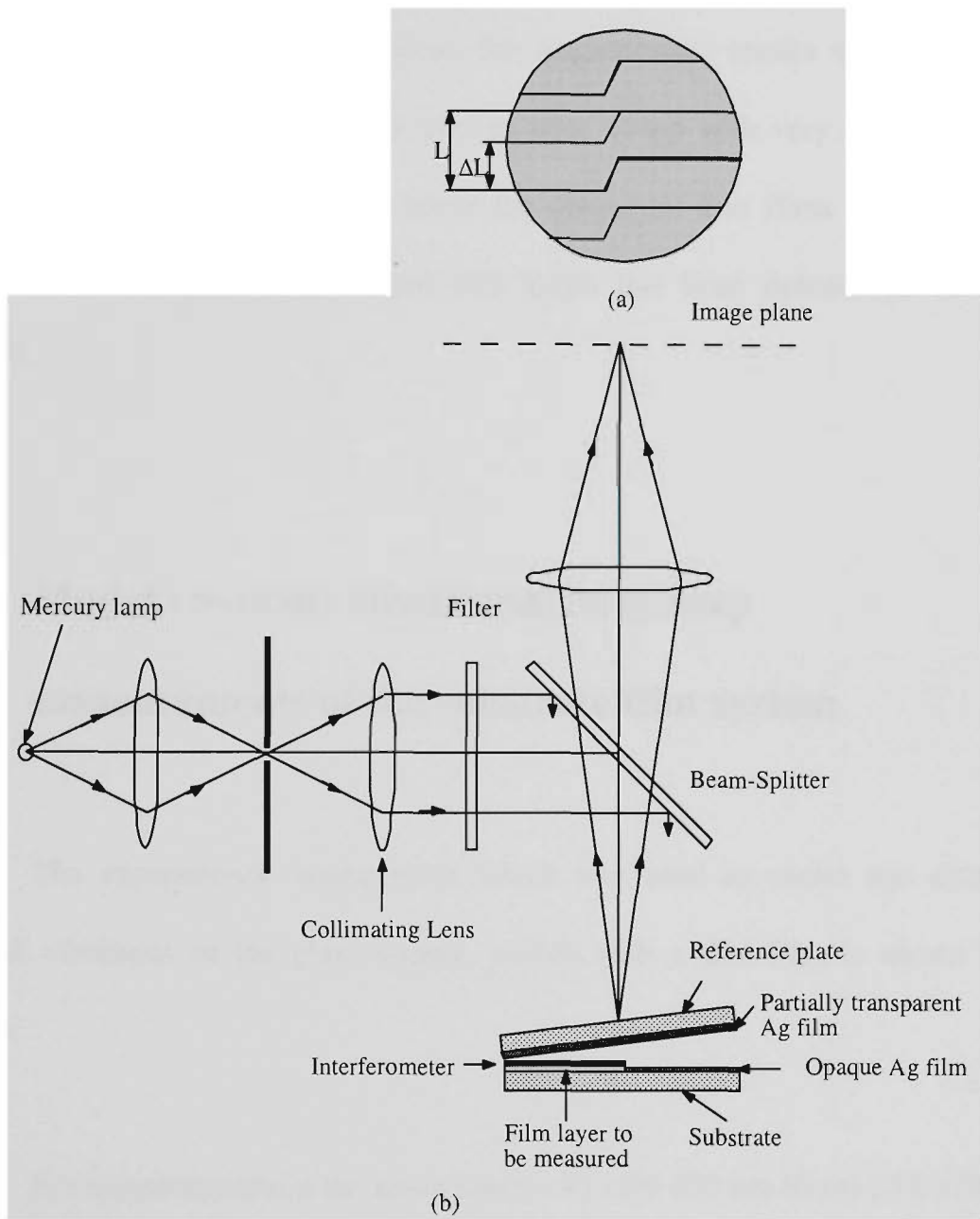


Figure 4.7 a) Angstromer - scope interferogram. ΔL is fringe spacing and L is fringe offset.
 b) Schematic of optical apparatus for the measurement of the thickness of thin film from multiple-beam Fizeau fringes. An opaque Ag film is deposited over a step in thin film.

The slides were coated under similar conditions to the 110 μm glass substrates. Since the slides are more than 10 times thicker than the glass substrates (1.5 mm), they do not bend appreciably as a result of the stress induced by the coating. Even if some bending did occur, the Angstrometer results would not be affected as it measures only the fringe change over a step with very small lateral dimension. The resulting calibration curve for chromium thin films is shown in Figure 4.8. The slope obtained from this graph has been determined to be 2.65 ± 0.075 .

4.6 Modal resonant vibrational frequency measurements of the substrate/film system

The experimental arrangement which was used to excite and detect mechanical vibrations of the glass sample, coated with a thin film is shown in Figure 4.9.

For measurements in the atmosphere a 40 mW 830 nm Sharp LTO15PD laser diode was used to excite vibrations in the sample. This diode was placed at a distance of approximately 250 mm from the sample. The output of the laser diode was square wave modulated (50 % duty cycle) using a TTL driving signal from a precision Hewlett Packard 33120A function generator. The output power of the laser diode was controlled by a Sharp IR3CO7 Laser Diode Driver integrated circuit.

This circuit incorporated automatic control of the optical output power via feedback from an internal photodiode to control the laser drive current. The laser was operated at an average power of 15 mW in order to keep it well below its damage threshold. The laser diode was mounted on an aluminium heat sink to keep its operating temperature well below its rated maximum of 50^o C.

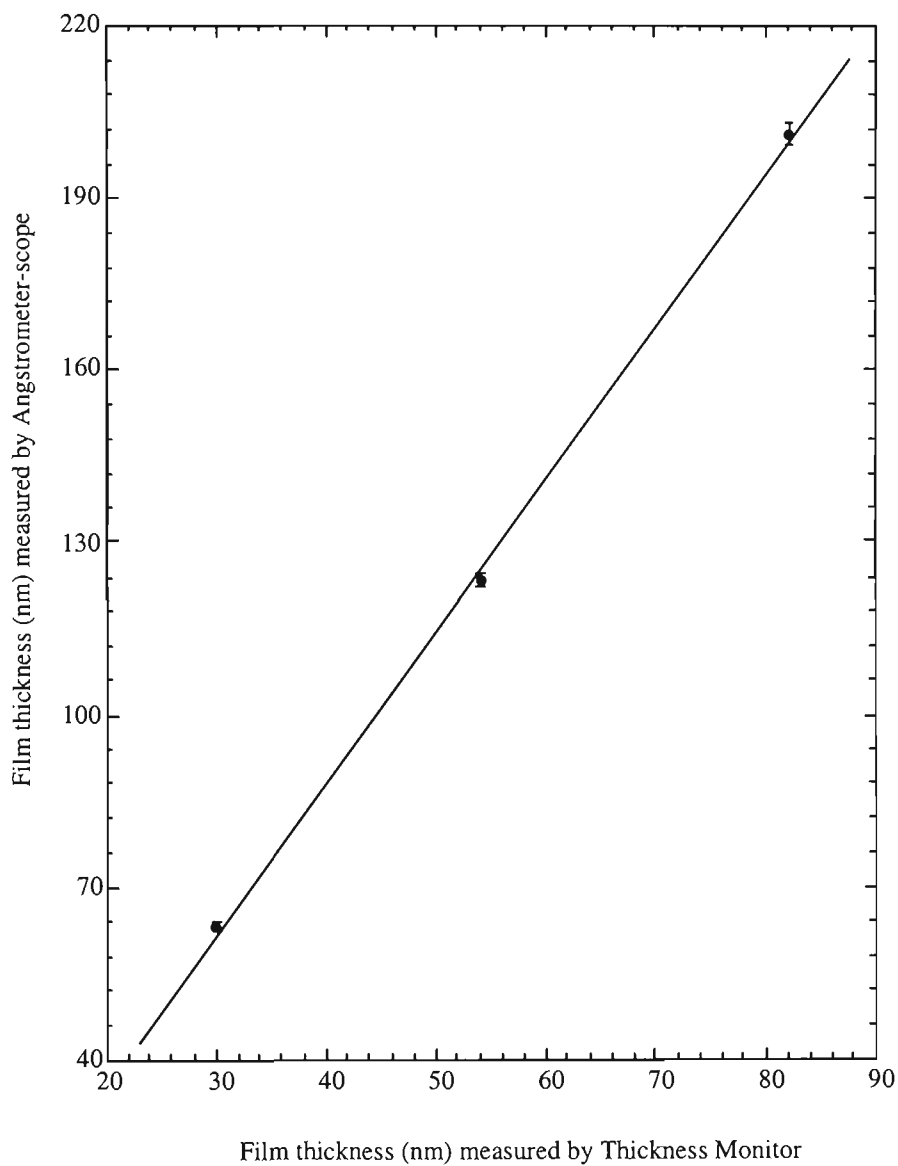


Figure 4.8 Calibration curve for the quartz crystal thickness monitor.

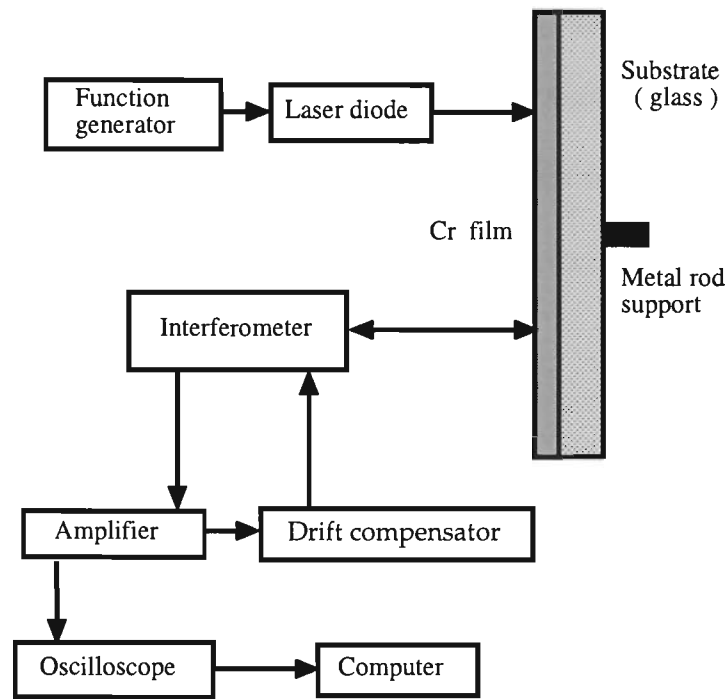


Figure 4.9 Schematic diagram of the experimental set-up used to excite and detect vibrations in a glass wafer coated with a thin film.

For detection of resonance, the output of the interferometer was monitored on the oscilloscope. Both the raw signal and the real-time FFT of this signal were monitored on separate channels. The resonant frequency was determined by adjusting the LD modulation frequency to maximise the amplitude of the particular mode. Since the Q of the resonance was high, this method had no difficulty in determining resonant frequencies to less 1 Hz. The resonant frequency was temperature dependent through the temperature dependence of elastic moduli. Thus fluctuations in ambient temperature were the limiting factor in resonant frequency detection in a vibration free environment. In the vacuum system, pump-generated vibration tends to limit the accuracy of resonant frequency determination from the sampled vibration waveform but a figure of 1 Hz is a reasonable guide to

the accuracy achieved. Variation of the modulation frequency by ± 0.5 Hz produced easily detectable changes in the interferometer output signal. For resonant frequency determination during a coating run, the evaporation rate was kept low so that manual changes could be made to the modulation frequency to confirm resonance at each measured point.

For some measurements the resonance detection system was automated by using a suitably filtered and amplified signal from the interferometer to modulate the LD. Provided the filter has a sufficiently narrow bandwidth the resonant vibration amplitude will grow from the initial vibration noise at the modal resonant frequency. In this way the resonant frequency could be read using a frequency counter or using the oscilloscope.

4.6.1 Homodyne optical fibre interferometric sensor

A fibre optic homodyne interferometer, shown schematically in Figure 4.10, was used to detect surface displacements of the sample caused by the photothermal excitation. This interferometer is a modified version of the interferometer used by Philp *et al.* (1994) for the measurement of small amplitude vibrations in a cantilever. The bandwidth of the Philp's detection electronics was 30 kHz and his interferometer was locked in the quadrature position using an active homodyne technique. The minimum detectable displacement of this interferometer

was reported as 0.3 nm for a signal to noise ratio of two, which corresponds to a minimum detectable phase shift of 2.4 mrad.

Light from a laser with long coherence length was coupled into a single-mode optical fibre. After input coupling, the light propagation in the fibre is split by

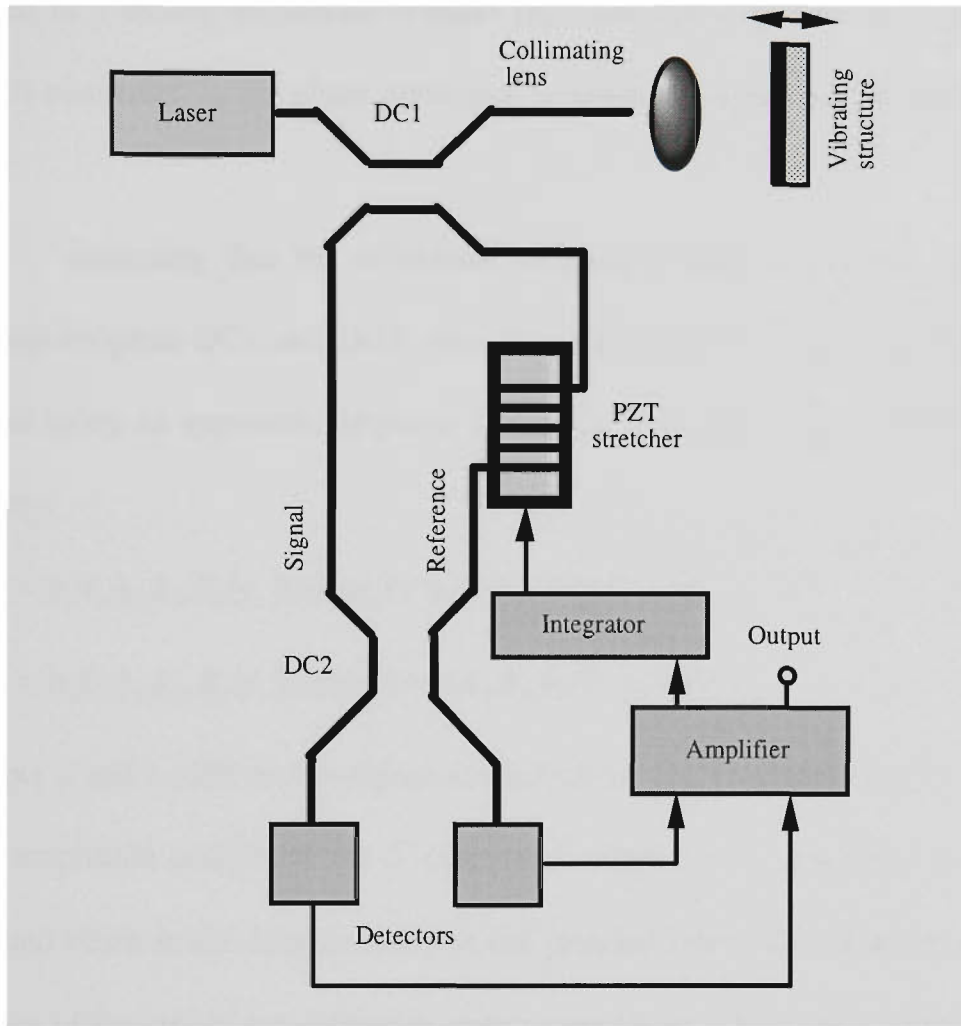


Figure 4.10 Schematic diagram of the fibre interferometer used to monitor surface displacements in the wafer.

a 3 dB (50% : 50%) directional coupler (DC1) into signal and reference arms as shown in the diagram. The reflected light from the vibrating surface will travel an effective distance Δl further than the light in the reference arm. This fact manifests itself in a phase shift between the signal and reference beams given by

$$\frac{\Delta\phi}{\phi} = \frac{\Delta l}{l}, \quad (4.2)$$

where $\phi = (2\pi/\lambda)nl$, l is the effective path length difference between signal and reference arm, λ is the wavelength of the laser light in vacuum and n is the index of refraction of the glass (about 1.5). Light from the reference and signal fibres is combined in a second directional coupler DC2 and the output in each arm of this coupler is controlled by the phase difference between the signal and reference arms.

Assuming that the amplitude coupling coefficients are k_1 and k_2 , for directional couplers DC1 and DC2, then the electric fields at each detector can be described using an approach similar to that of Jackson and Jones (1989) and Udd (1991), by:

$$E_1 = \alpha_s k_{1t} k_{1c} k_{2t} E_0(\tau_s) \exp(i\varphi_s) + \alpha_r k_{1c} k_{2c} E_0(\tau_r) \exp(i\varphi_r) \quad (4.3)$$

$$E_2 = \alpha_s k_{1t} k_{1c} k_{2c} E_0(\tau_s) \exp(i\varphi_s) + \alpha_r k_{1c} k_{2t} E_0(\tau_r) \exp(i\varphi_r). \quad (4.4)$$

Subscripts s and r refer to the signal and reference arms respectively, $k_{i(t \text{ or } c)}$ is the coupler amplitude coefficient for i^{th} directional coupler and subscript t denotes the transmitted beam in the coupler and c is the coupled beam, φ_s and φ_r are the phase retardance of the signal and reference arms, respectively. E_0 is the amplitude of the time-dependent source electric field, where τ_s and τ_r are propagation times from the source to the detectors via the signal and reference arms and α_s and α_r are the losses in signal and reference arms of the interferometer respectively. α_s occurs principally in the open air part of the signal arm and α_r is a loss which can be introduced into the reference arm to match the signal and reference powers and improve fringe visibility.

The coupled coefficients are complex to allow for phase changes that take place on coupling. The coupled arm of an ideal 50:50, 2x2 directional coupler experiences a $\pi/2$ phase retardance with respect to that of the direct (transmitted) arm. Therefore k_{ii} may be defined as real, making k_{ic} are imaginary, so that $k_{ic} = ik'_{ic}$, where k'_{ic} is real. If one traces the light through the system then the electric fields at detectors 1 and 2 may be written:

$$E_1 = \alpha_s k_{1i} (ik'_{1c}) k_{2i} E_0(\tau_s) \exp(i\varphi_s) + \alpha_r (ik'_{1c}) (ik'_{2c}) E_0(\tau_r) \exp(i\varphi_r) \quad (4.5)$$

$$E_2 = \alpha_s k_{1i} (ik'_{1c}) (ik'_{2c}) E_0(\tau_s) \exp(i\varphi_s) + \alpha_r (ik'_{1c}) k_{2i} E_0(\tau_r) \exp(i\varphi_r). \quad (4.6)$$

The output intensity observed at each detector I_i may be evaluated using

$$I_i = \langle E_i \cdot E_i^* \rangle, \quad (4.7)$$

where $\langle \dots \rangle$ denotes a time average over a period of the field and * indicates the complex conjugate. By combining equations 4.5 and 4.7 the output intensity at detector 1 is

$$I_1 = \alpha_s^2 k_{1i}^2 k_{2i}^2 k_{1c}^2 \langle E_0^2(\tau_s) \rangle + \alpha_r^2 k_{1c}^2 k_{2c}^2 \langle E_0^2(\tau_r) \rangle + 2 \operatorname{Re} \left[\alpha_s \alpha_r k_{1c}^2 k_{2c}^2 k_{1i} k_{2i} \langle E_0(\tau_s) \cdot E_0^*(\tau_r) \rangle \right] \sin(\varphi_s - \varphi_r). \quad (4.8)$$

Equation 4.8 can be simplified by noting that $\langle E_0^2(\tau_s) \rangle$ and $\langle E_0^2(\tau_r) \rangle$ are the source intensity, I_0 , coupled into the input fibre and that the degree of coherence γ of the source is given by

$$\gamma(\tau_s - \tau_r) = \frac{\langle E_0(\tau_s) \cdot E_0^*(\tau_r) \rangle}{I_0}. \quad (4.9)$$

Thus,

$$I_1 = I_0 \left[\alpha_s^2 k_{1i}^2 k_{2i}^2 k_{1c}^2 + \alpha_r^2 k_{1c}^2 k_{2c}^2 + 2 \alpha_s \alpha_r k_{1c}^2 k_{2c}^2 k_{1i} k_{2i} \gamma \sin(\varphi_s - \varphi_r) \right]. \quad (4.10)$$

A similar analysis starting with equation 4.6 yields

$$I_2 = I_0 [\alpha_s^2 k_{1l}^2 k_{2l}^2 k_{1c}^2 + \alpha_r^2 k_{1c}^2 k_{2c}^2 - 2\alpha_s \alpha_r k_{1c}^2 k_{2c}^2 k_{1l} k_{2l} \gamma \sin(\phi_s - \phi_r)]. \quad (4.11)$$

Therefore, it can be seen that the AC components of the intensities at the two detectors are in antiphase. Periodic changes in the optical path length of the open-air gap, due to vibration of the reflective surface, modulates the phase difference $\phi_s - \phi_r$ between the signal and reference beams at the detectors and so varies the output intensity according to a *sine* function as shown in Figure 4.11. The reason for the $\sin(\phi_s - \phi_r)$ terms in equations 4.10 and 4.11 rather than the usual $\cos(\phi_s - \phi_r)$ is that with this particular interferometer arrangement there is an additional 90° phase shift introduced in the second pass of the signal beam through DC1.

The fringe amplitude is only substantial provided the light from the reference and signal arms maintains a reasonable degree of coherence. If the optical path difference between the two interferometer arms is comparable to the coherence length of the source, then the amplitude of the AC component of the intensity in the output arms will decrease and the fringes will become more difficult to observe. Figures 4.11 and 4.12 show fringes produced by the two interfering beams under different conditions. Fringe visibility (V') is defined as

$$V' = \frac{I_{\max} - I_{\min}}{I_{\max} + I_{\min}} \quad (4.12)$$

where I_{\max} and I_{\min} are the maximum and minimum values of intensity as $(\phi_s - \phi_r)$ is varied.

For equal signal and reference intensities, V' is dependent on the degree of coherence between the two beams. Equation 4.10 is rewritten in the form

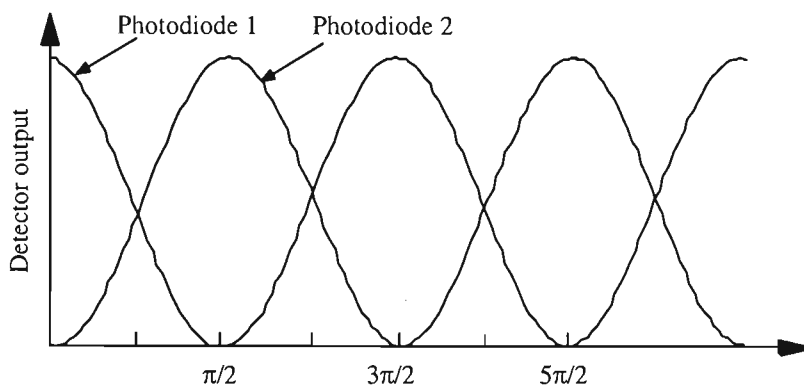
$$I_I = I_0' [1 + V' \sin(\varphi_s - \varphi_r)], \quad (4.13)$$

where

$$V' = \frac{2\alpha_s \alpha_r k_{1c}'^2 k_{2c}'^2 k_{1t}' k_{2t}'}{\alpha_s^2 k_{1t}'^2 k_{2t}'^2 k_{1c}'^2 + \alpha_r^2 k_{1c}'^2 k_{2c}'^2} \gamma \quad (4.14)$$

and

$$I_0' = I_0 (\alpha_s^2 k_{1t}'^2 k_{2t}'^2 k_{1c}'^2 + \alpha_r^2 k_{1c}'^2 k_{2c}'^2). \quad (4.15)$$



Optical phase difference between signal and reference beams in radians.

Figure 4.11 Interferometer output.

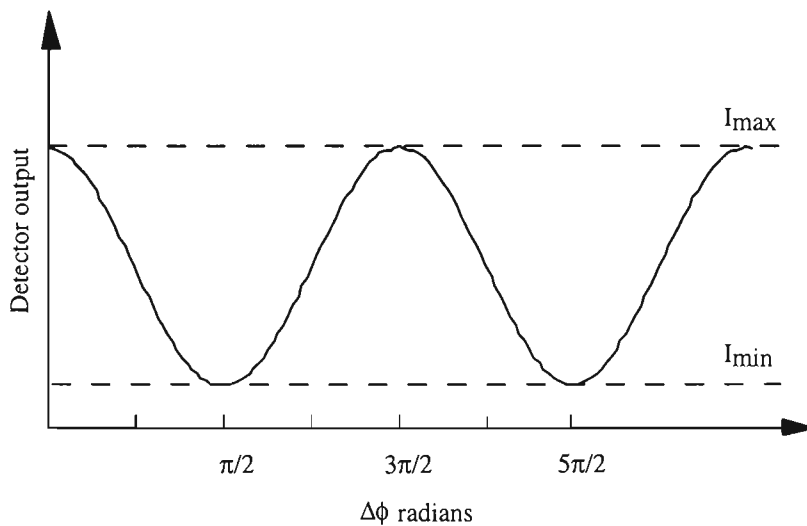


Figure 4.12 Interferometer output for $V' < 1$.

When the polarisation vectors of the signal and reference beams are not parallel, then the fringe visibility will further decrease. In this case, equation 4.13 can be rewritten as:

$$I_1 = I_0' [1 + V \cos\theta \sin(\varphi_s - \varphi_r)] \quad (4.16)$$

and

$$I_2 = I_0' [1 - V \cos\theta \sin(\varphi_s - \varphi_r)] \quad (4.17)$$

where θ is the angle between the two polarisation vectors. For maximum fringe visibility or output signal, θ should be as small as possible and for $\theta \rightarrow \pi/2$, total loss of signal occurs.

A small change of air path between fibre tip and vibrating structure induces a small change in phase difference, $\Delta\phi$, in equation 4.16 and 4.17 which is typically of the order of milli- to micro-radians. Small changes in phase can be made to induce significant changes in the output of suitably-designed detector electronics provided the interferometer is appropriately biased. The small-signal sensitivity of the sensor $dI/d(\Delta\phi)$ is dependent on the phase difference between signal and reference arms (phase bias). From equation 4.16 and 4.17 the small-signal sensitivity,

$$\left| \frac{dI}{d(\Delta\phi)} \right| \propto \left| \frac{d[\sin(\Delta\phi)]}{d(\Delta\phi)} \right| = |\cos(\Delta\phi)|, \quad (4.18)$$

is zero for $\Delta\phi \rightarrow \pi/2$. This is shown in Figure 4.13 where the sensitivity is plotted against $\Delta\phi$. From this plot, maximum sensitivity is achieved when the phase difference between the arms of the interferometer is set, or biased to a multiple of π .

The effect of operating at different phase bias points is shown schematically in Figure 4.14. The maximum sensitivity point is referred to as the quadrature point.

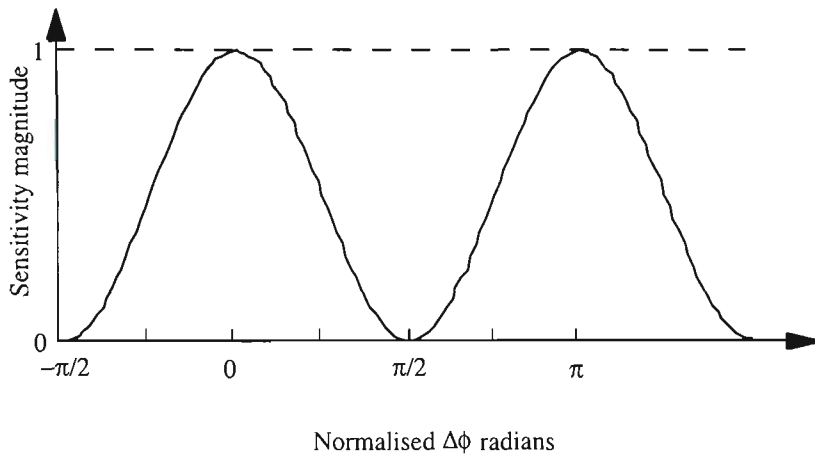


Figure 4.13 Small - signal sensitivity versus phase difference between the two arms of the interferometer.

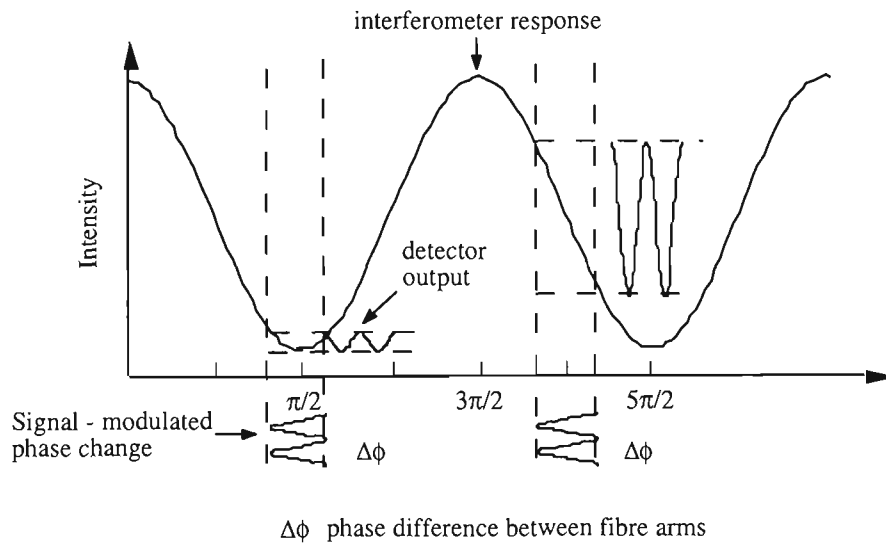


Figure 4.14 Signal fading problem in fibre interferometer.

Many factors such as temperature and strain variations may cause phase variations between two fibre interferometer arms. The optical path length difference between the reference and signal arms of the interferometer may, therefore, drift in

time. This will cause corresponding drifts in the sensitivity of the interferometer. This drift causes fading of the output signal of the interferometer. The fading can be eliminated by placing a feedback-controlled phase shifter in the reference arm and using the feedback to compensate for low-frequency drift-induced phase changes. Such a phase shifter can be produced by wrapping a number of turns of the reference fibre around a piezoelectric cylinder. Phase changes are induced by expansion and contraction of the fibre in response to voltages applied to the cylinder. The output of the detector in this situation is given by

$$V = V_0 \{1 \pm \sin[s(t) + A(t) + \phi_{nr} + \phi_{ns}]\} \quad (4.19)$$

where $s(t)$ is the signal phase to be detected, $A(t)$ is the phase shift induced by the piezoelectric phase shifter and ϕ_{nr} and ϕ_{ns} are drift-generated (noise) phase shifts in reference and signal arm, respectively.

From equation 4.19 it can be concluded that for maximum sensitivity the phase shifter should be set so that $A(t) + \phi_{nr} + \phi_{ns} \cong \pi$. The signal $A(t)$ is used to track out all low-frequency perturbations and keep the sensor interferometer at its quadrature point (maximum sensitivity). For this type of drift compensation to work, the signal-induced changes must be at frequencies well above the cut-off frequency of the feedback circuitry. The operation of the feedback circuit is most easily understood by observing that the voltage applied to the PZT stretcher (Figure 4.10) will continue to change until the input of the integrator (low pass filter) goes to zero. Since the changes in the two detector outputs are out of phase, this can only occur when both inputs to the differential amplifier are equal, i.e. at the quadrature point. Hence the effect of the circuit is to compensate for low frequency phase

changes and lock the interferometer at its quadrature point. High frequency phase changes are unaffected by the feedback circuit as they are not passed by the low pass filter.

4.6.2 Practical description of the interferometric sensor

a) Optical layout

A schematic representation of the experimental setup used to excite and detect the modal resonant vibrational frequencies of the substrate/film system is shown in Figure 4.15. The light source was a HeNe laser (Melles Griot OS SIP 871) emitting approximately 1.2 mW of light at wavelength of 1523.2 nm. Light was launched into one input arm of a standard single mode 1550 coupler (DC1) by means of a x10 microscope objective lens mounted in a Newport MF-915T positioner, which in turn was mounted directly on the front of the laser. The coupler divided the light into the reference and signal paths. A second x10 microscope objective lens, mounted in another Newport MF-915T positioner, collimated light from one of the outputs of DC1 to the vibrating substrate/film structure, the second output of DC1 constituted the reference arm. The interferometer laser gave a nominal optical power of 45 μ W at the sample surface and the reflected light from the substrate/film structure was focussed back into the signal arm. This returning

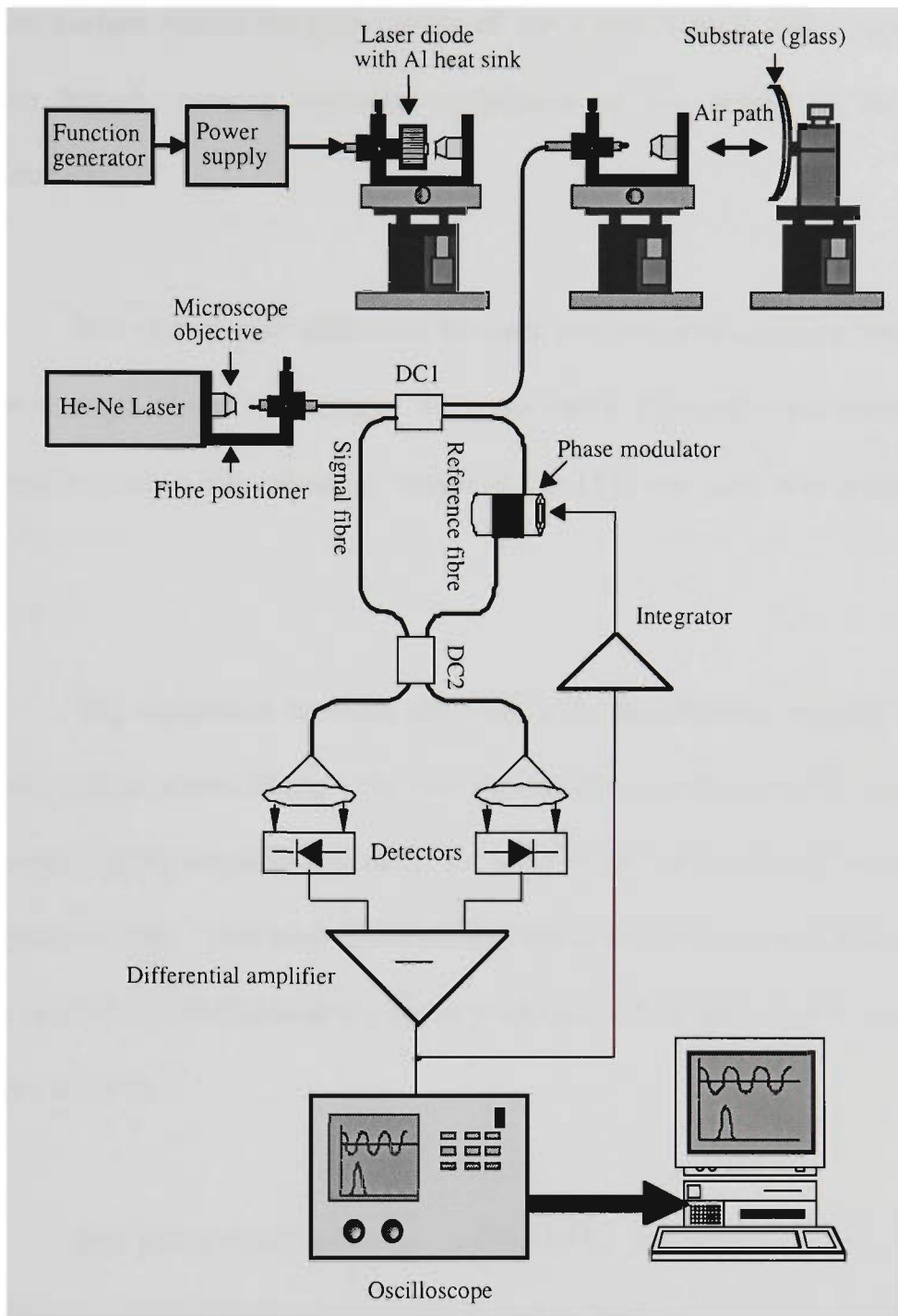


Figure 4.15 Experimental set-up in more detail.

light was also divided by DC1 into two paths, one returning back to the laser, the second forming the remainder of the interferometer's signal arm. The signal and reference beams were then recombined using a second 2x2 1550 directional coupler (DC2). Any change in air path between the sensing fibre tip and the vibrating

reflective surface varied the path length of the signal branch with respect to the reference branch, causing intensity modulation of the output of the InGaAs photodetectors.

The optical path difference between the two arms must be less than the coherence length of the light source. This was easily arranged in the interferometer arrangement used as the coherence length of the 1523 nm laser was greater than 1 metre.

The separation between the fibre and the vibrating surface (open air path) was typical about 20 cm. The two optical fibres (reference and signal arms) were paired closely together and therefore were largely subjected to the same non-signal perturbations. This tended to minimise the interferometer drift and reduce the voltage needed on the piezoelectric phase modulator. The optical path length of the each arm was 8 m.

The phase modulator was constructed by winding 50 turns of single mode fibre (standard Optix 1300/1550 nm communications fibre) around a piezoelectric cylinder (Tokin XOZ-138) of outside diameter 38 mm, inside diameter 36 mm and height 30 mm. This phase modulator was similar to that described by a number of other workers (Kingsley, 1978; Jackson *et al.*, 1980) and involved phase change being induced into the reference fibre by a voltage-induced radial change in the dimensions of the PZT which applied a longitudinal strain to the wound fibre. The induced phase shift in these devices is given by (Digonnet and Kim, 1988)

$$\Delta\phi = \frac{2\pi}{\lambda}(l\Delta n+n\Delta l), \quad (4.20)$$

where Δn and Δl are variations of the refractive index and the fibre length respectively and λ is the vacuum wavelength of laser beam. Martini (1987) gives a detailed analysis of the phase modulation efficiency (milliradian $V^{-1}\text{turn}^{-1}$) which can be obtained with PZT-type modulators. Kingsley (1978) and Jackson *et al.* (1980), operating at frequencies well below the first mechanical resonance, obtained values 70 volt-turn and 100 volt-turn respectively for a 2π radian phase shift at 633 nm using Vernitron PZT-5H ceramic piezoelectric transducers. These values are in general agreement with what would be expected from the calculations of Martini. In the arrangement described above using a Tokin PZT cylinder, the number of volt-turns for a 2π radian phase shift can be approximately calculated. The voltage V applied to the PZT, through the piezoelectric effect, causes the radius of the cylinder to expand or contract an amount $\Delta r=d_{PZT}V$ where d_{PZT} is the piezoelectric coefficient which is approximately $4.10 \times 10^{-10} \text{ mV}^{-1}$ (Ohki, *et al.*, 1992). The fibre attached to the cylinder will be stretched by cylinder expansion and its increased length will induce a phase shift in the propagating light. The fibre length extension is given by $\Delta L=2\pi N\Delta r$ where N is the number of turns. By neglecting variations of the refractive index when the fibre is stretched ($\Delta n=0$) the equation 4.20 becomes

$$\Delta\phi \approx \frac{4\pi^2}{\lambda} nNd_{PZT}V. \quad (4.21)$$

For $n=1.53$ (for glass), $N=50$ and $\lambda=1523.2$, we obtain

$$\Delta\phi \approx 0.792V \text{ (radian)}. \quad (4.22)$$

Hence, a phase change of 2π radians requires about 7.9 V. The piezoelectric feedback used an 18 V power supply and this proved to be quite adequate for drift compensation in a laboratory environment.

(b) Detector and feedback circuitry

The circuit diagram for the electronics used to detect the optical signal from the interferometer and to drive the piezoelectric modulator is shown in Figure 4.16. The two output signals of the interferometer are in antiphase and subtraction of these signals in a differential amplifier reduces the common mode noise and improves the signal-to-noise ratio. Two InGaAs photo detectors (LYTEL 0981) were followed by NE 5532 (A1 and A2) low noise operational amplifiers used in a transimpedance configuration. Further amplification was provided by LM347 low noise amplifiers (A3 and A4) before the signal has subtracted in a further LM347 (A5). The electrical bandwidth of the detectors and associated amplifiers was DC to 100 kHz.

The output of A5 was integrated using another LM347 (A6) and the output of this stage was used to drive the piezoelectric modulator. Provided the output voltage swing from A6 is large enough, this signal can maintain the interferometer at the quadrature point. The detector/feedback circuit was powered using two 18V batteries. For noise isolation, the circuit and batteries were mounted in a grounded metal box.

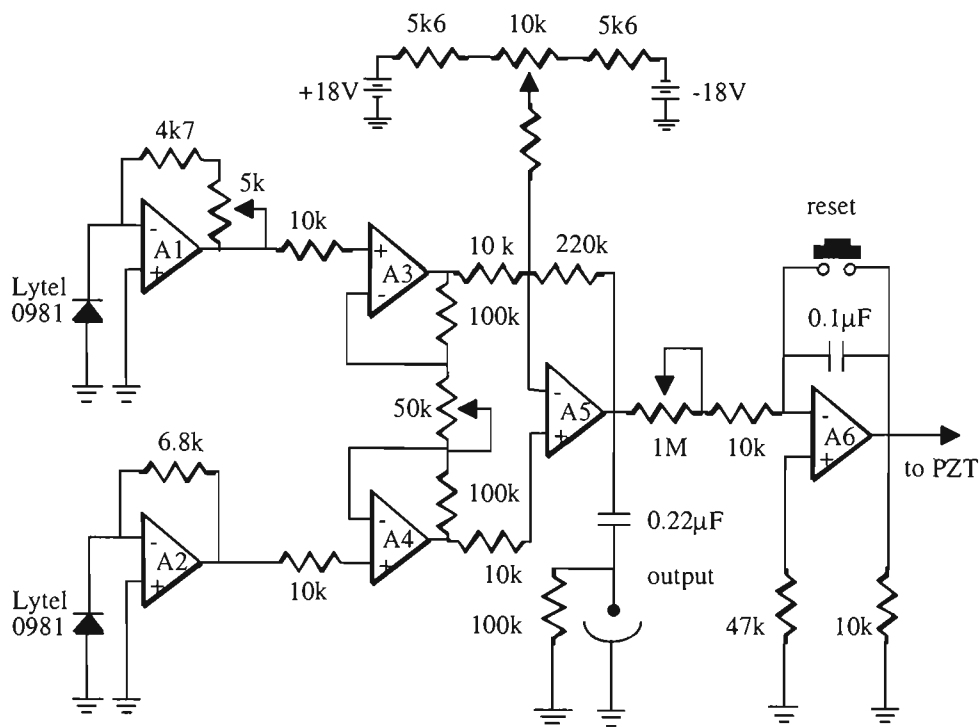


Figure 4.16 Electronic circuit to detect optical signal from interferometer and to drive PZT.

(c) Calibration of the interferometer

The interferometer was tested and calibrated by using the Lutz-Pickelmann piezoelectric mirror shaker (PZMS) type MB-ST-500/3. The PZMS was biased at +250V and was modulated by an $300 V_{p-p}$ ac voltage at a frequency of 410 Hz. The detector output, V , is related to the displacement, η , by the relation (Scrubby and Drain, 1990)

$$V = V_{DC} + V_0 \sin\left(\frac{4\pi\eta}{\lambda}\right), \quad (4.23)$$

where λ is the wavelength, V_0 is the amplitude of the interference signal and V_{DC} is the DC bias signal. The proportionality constant between the output of the interferometer and displacement depends on the optical signal levels and amplifier

gains. Calibration under operating conditions is necessary for absolute measurement of displacement. This was accomplished by switching off the PZT feedback and using sufficient vibration amplitude on the PZMS to take the interferometer output through a number of fringes. The peak interferometer signal voltage is then the parameter V_0 in equation 4.23. When the feedback is restored and the vibration amplitude of the PZMS is restricted so that the amplitude of the AC component of the interferometer output is less than V_0 , it can be simply shown (Scruby and Drain 1990) that the displacement η is related to the output V by

$$\eta = \frac{\lambda}{4\pi} \sin^{-1}\left(\frac{V}{V_0}\right) \approx \frac{\lambda}{4\pi} \frac{V}{V_0}, \quad \text{if } V \ll V_0. \quad (4.24)$$

The noise equivalent displacement, η_N , which is the displacement corresponding to the RMS noise level, is given by (Scruby and Drain, 1990)

$$\eta_N \approx \frac{\lambda}{4\pi} \frac{\langle V_N^2 \rangle^{\frac{1}{2}}}{V_0}, \quad (4.25)$$

where $\langle V_N^2 \rangle$ is the mean square noise at the output of the detector. The noise equivalent displacement (NED) was found to be 0.16 nm with an electrical bandwidth of 100 kHz.

A summary of characteristics and performance of the active homodyne interferometer is given in Table 4.1. This interferometer is amplifier noise limited and an appropriate performance figure of merit is the NED divided by the square root of the bandwidth. The NED can be reduced by limiting the electrical bandwidth of the detector electronics. This could have been done easily in the present work as the signal frequencies of interest were generally less than 10 kHz. However, since

the signal-to-noise ratio was more than adequate with the 100kHz circuitry, no attempt was made to limit the bandwidth. It should be noted that all calibration measurements have been made using the PZMS with a fully reflecting mirror mounted in the mirror shaker. This gives a high V_o for a given laser power and hence a low NED for a given noise level. If a less reflecting surface is used, a lower value of V_o would be obtained which would increase NED figure. The reflecting surface from the samples used in this work was titanium film of 20 nm thickness. This is a very good reflector and therefore during the experimental measurements the NED figure was very close to value as stated in Table 4.1.

Table 4.1 A summary of characteristics and performance of the active homodyne interferometer used to measure the changes of resonant frequencies which are related to the changes in the stress developed in thin films.

Wavelength	1523.2 nm
Detector	LYTEL 0981 (InGaAs)
Laser	Melles Griot 05 SIP 871 (1.2 mW)
Total optical path length	853 cm
Air path length	20 cm x 2
Bandwidth	100 kHz
RMS noise	5.7 mV
Total NED	0.16 nm
NED/ $\sqrt{\text{Hz}}$	5.06×10^{-13} m/ $\sqrt{\text{Hz}}$

4.7 Physical principle of the photothermal excitation mechanism

The physical principles involved in the generation of mechanical vibration using modulated laser beam are best understood by considering processes

occurring in metals. When a modulated laser beam illuminates a small region of a target, part of energy is absorbed by interaction of electromagnetic radiation with the surface. This process depends upon the electrical and magnetic properties of the material and the frequency of radiation. The remaining energy of the laser beam is reflected or scattered from the surface. The absorbed electromagnetic energy is converted to thermal energy resulting in a rapid rise in temperature. This temperature rise in turn gives rise to transient thermoelastic stress and strain in a very thin surface layer as the metal tries to expand. With heat diffusion, a time dependence temperature profile develops in the sample (Opsal and Rosencwaig, 1982). This time-dependent variation of temperature between the illuminated and rear (unilluminated) surface produces a modulated bending moment and thus the sample flexes and begins to vibrate at the modulation frequency. If the modulation frequency corresponds to a resonant vibration mode of structure, the amplitude of vibration is significant.

Since the glass or substrates used in the work described in this thesis are not strongly absorbing materials, the photothermal excitation can be greatly increased by coating one surface of the substrate with a thin coating of metal which is strongly absorbing at the laser wavelength used. This was generally achieved by sputtering a thickness of about 20 nm of titanium onto the rear surface of the substrate before deposition, on front substrate surface, of the film to be studied. The heat generated in this rear surface film is transferred to the glass substrate causing it to bend.

4.8 Description of modified vacuum system

As described in previous sections, the all-optical technique developed during this work allows indirect measurement of stress in coated substrates which were removed from a vacuum deposition system. This technique was modified to allow real-time measurements under controlled conditions inside a vacuum system. This has permitted much more accurate and reliable measurements and is very easy to implement as it only requires two optical fibre feedthroughs into the vacuum system. For this purpose the vacuum system described in section 4.2.1 was modified. Figure 4.17 shows a schematic representation of the vacuum coating chamber and excitation/sensing systems for in situ monitoring the modal resonant vibrational frequencies of the substrate/film system. The focussed and modulated laser diode light, for photothermoelastic excitation of the sample, was delivered to the substrate in the vacuum chamber via an optical fibre of core diameter 100 μm placed about 60 mm from its rear surface. The optical power incident on the sample was 13 mW. Only the one sensing fibre of the interferometer was passed through a feedthrough into the vacuum chamber (about 50 mm from the rear surface of the substrate being measured). Vibration from the mechanical pump was minimized by mounting it away from the coating plant. Figure 4.18 shows a typical FFT (Fast Fourier Transform) trace of the output of the interferometer when the resonance at about 3400 Hz was excited. This trace shows that most of the environmental noise is at low frequency and the signal-to-noise is quite high for frequencies greater than 2 kHz. The mechanical and diffusion pumps were operating during these measurements.

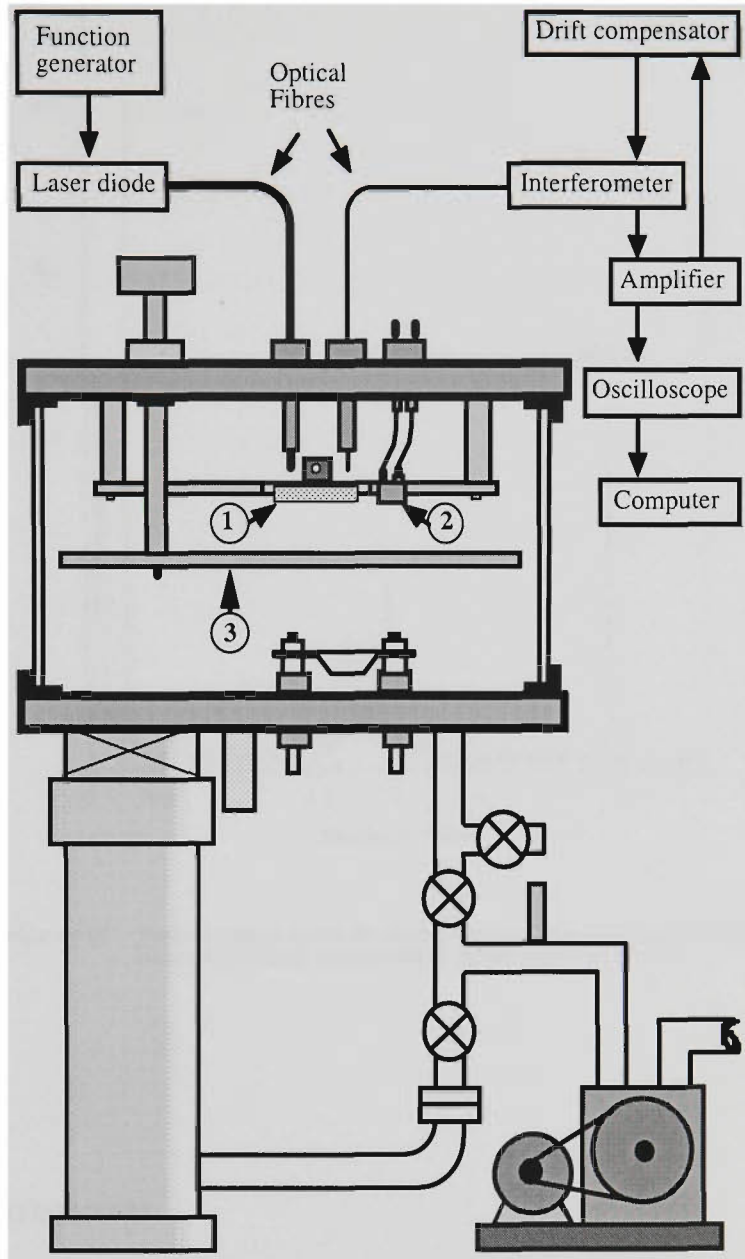


Figure 4.17 Schematic diagram of evaporation plant with experimental setup for in situ measurement of stress in thin films: (1) Glass substrate; (2) Head of film thickness sensor; (3) Shutter.

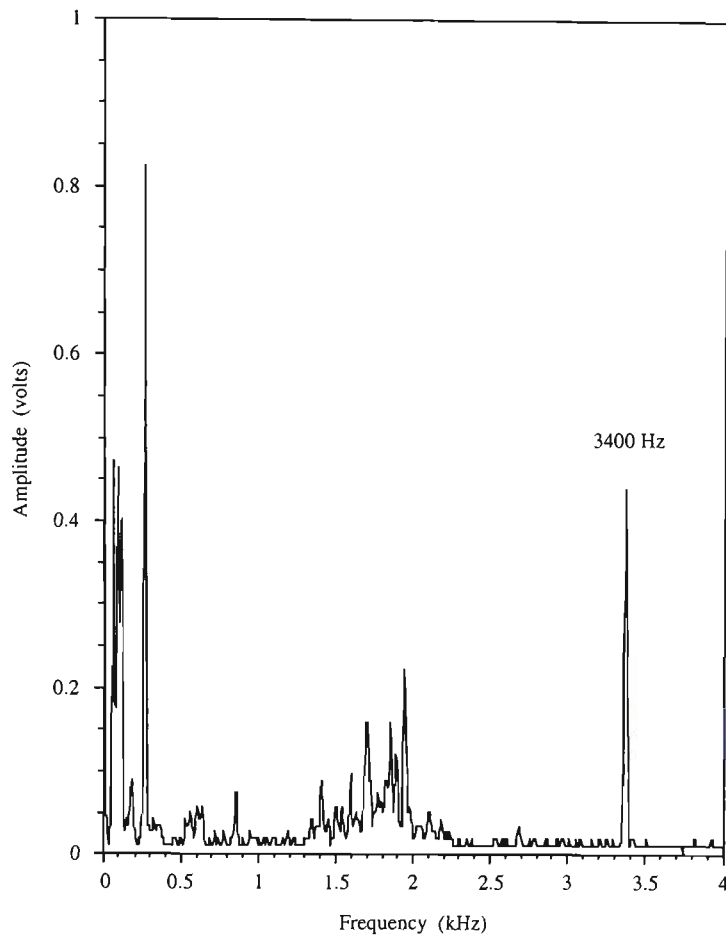


Figure 4.18 Typical output of the interferometer when the resonance at about 3400 Hz was excited. During these measurements all pumps were running.

4.9 Summary

The new fibre optic technique, described in this work, was first demonstrated when the samples were coated with Cr thin films in vacuum system and then removed for resonant frequency measurements under room conditions. The operation and design details of the homodyne interferometric sensor and its electronic signal processing circuit were described. This interferometer had a noise equivalent displacement (NED) of 0.16 nm with a bandwidth of 100 kHz.

For in situ measurements under controlled conditions the existing vacuum system was modified to accommodate the fibres of the interferometric sensor and photothermoelastic excitation systems. This modification requires only two feedthroughs into the vacuum system. Vibration from the mechanical pump was minimized by mounting it away from the frame of coating plant. The FFT trace of the interferometer output showed that an excellent signal-to-noise ratio was achievable during vacuum system operation for modes with resonant frequencies above 2 kHz. The equipment described in this chapter was used to make measurements with Cr and MgF₂ films and the data obtained is presented and discussed in the following chapter.

Experimental results and discussion

5.1 Introduction

The experimental techniques and corresponding stress equations, described in the preceding chapters are, in principle, simple. However, the stress may display variations as a function of deposition variables, the nature of the film-substrate interface and film thickness. Important deposition variables include substrate temperature relative to the melting point of metal, deposition rate, vacuum residual gas composition and pressure and also angle of incidence of the vapour beam. Data published by different investigators employing different measurement techniques for stress determination are frequently inconsistent. The following trends can be discerned from published results for stress in metallic and non-metallic thin films:

- (a) In metals coated on glass substrates, the film stress is tensile with a magnitude ranging from 10 MPa to 2000 MPa.
- (b) The magnitude of the stress in non-metallic thin films is frequently small. It should be noted that while the most

metallic thin films are under tension, dielectric and semiconductor films are generally in state of compression. Metals with high melting points generally tend to exhibit higher residual stress than more easily melted metals.

The experimental technique for indirect measurements of stress in coated substrates, described in the preceding chapters, was initially tested using chromium as the evaporation material. This chapter presents results for both chromium and magnesium fluoride thin films. In the early work on chromium films, the samples were coated in the vacuum chamber and then removed for resonant frequency measurement in the atmosphere. This was followed by re-insertion into the vacuum chamber and the cycle was repeated until a set of measurements had been made for various film thicknesses. Since the surface of each layer was exposed to air, the layers contain gaseous contaminants. To try to measure the extent of this problem, an Auger Nanoprobe was used to determine concentration of principal species as a function of depth. One further problem with these early measurements was that it was not possible to measure the resonant frequency of the substrate before coating commenced. This is due to the lack of any layer to act as an absorber for the excitation laser beam before the first coating layer was applied. These early measurements used the chromium layers themselves to absorb the laser modulation and reflect the interferometer beam.

For subsequent measurements using both Cr and MgF_2 films two improvements were made:

- (a) A thin layer of titanium was applied to the rear surface of the substrate to act as an absorber/reflector. This is a low stress layer, which does not contribute significantly to the overall stress/curvature of the samples.
- (b) The measurements were made in situ in the vacuum system and so atmospheric contamination between successive layers was not a problem.

The use of both atmospheric and in-situ measurement allows some quantification of the effect of the atmosphere on the coatings.

5.2 Auger Nanoprobe Analysis and depth profiles

The radius of curvature and the resonant frequencies of the glass plates were measured after depositing each successive layer of Cr and the stress of the composite calculated using Equation 3.66. It should be noted that Equation 3.66 assumes a uniform homogeneous film and the removal of the test sample from the vacuum chamber may produce a non-homogenous structure. Since chromium is a reactive material, some surface oxidation is to be expected. In addition, gas molecules incorporated into the lattice of Cr during deposition of the film may affect the stress. While the bulk of the contamination should arise from the atmosphere, organic molecules within the vacuum chamber originating from a diffusion pump oil, vacuum grease, gasket materials and adsorbed gases can be also incorporated in the lattice structure of the Cr during thin film growth as the base pressure of the vacuum system was only about 10^{-6} mbar. To check the homogeneity of the films, the samples were subjected to Auger Nanoprobe analysis.

The Auger Nanoprobe detects and measures the Auger electron signals from a sample (Ferguson, 1989). Auger electrons arise when an atom in the sample is struck by a fast-moving particle such as an electron and an inner shell is ionised. The vacancy can be filled by another electron in the atom making either a radiative (X-ray) or non-radiative (Auger) transition. The latter case can result in the emission of an electron with kinetic energy which is uniquely defined by the energies of the levels and which is thus characteristic of the ionised atom. Analysis of these Auger electrons permits quantitative analysis of the composition of the surface of a material. The Auger process is more probable than X-ray emission for energies less than about 3 keV and is strongest for lower atomic number elements

The energy of Auger electrons varies between about 10 eV and 2300 eV (Ferguson, 1989) with a mean free path of about 0.4 - 4 nm, in metals. To achieve a meaningful Auger analysis, in particular for low mean free path electrons, the equipment must be capable of maintaining a vacuum of better than 10^{-7} Pa if the surface is to be kept clean long enough for the analysis to be carried out. It is generally necessary to clean the surface before Auger analysis is possible. This is usually done by means of an ion etching device (ion gun) mounted in the apparatus. The ion gun is also used to expose successively deeper layers for Auger analysis.

A depth profile of a wafer coated with eight layers of Cr was made using the Auger Nanoprobe. During production of this film, the surface of each layer was

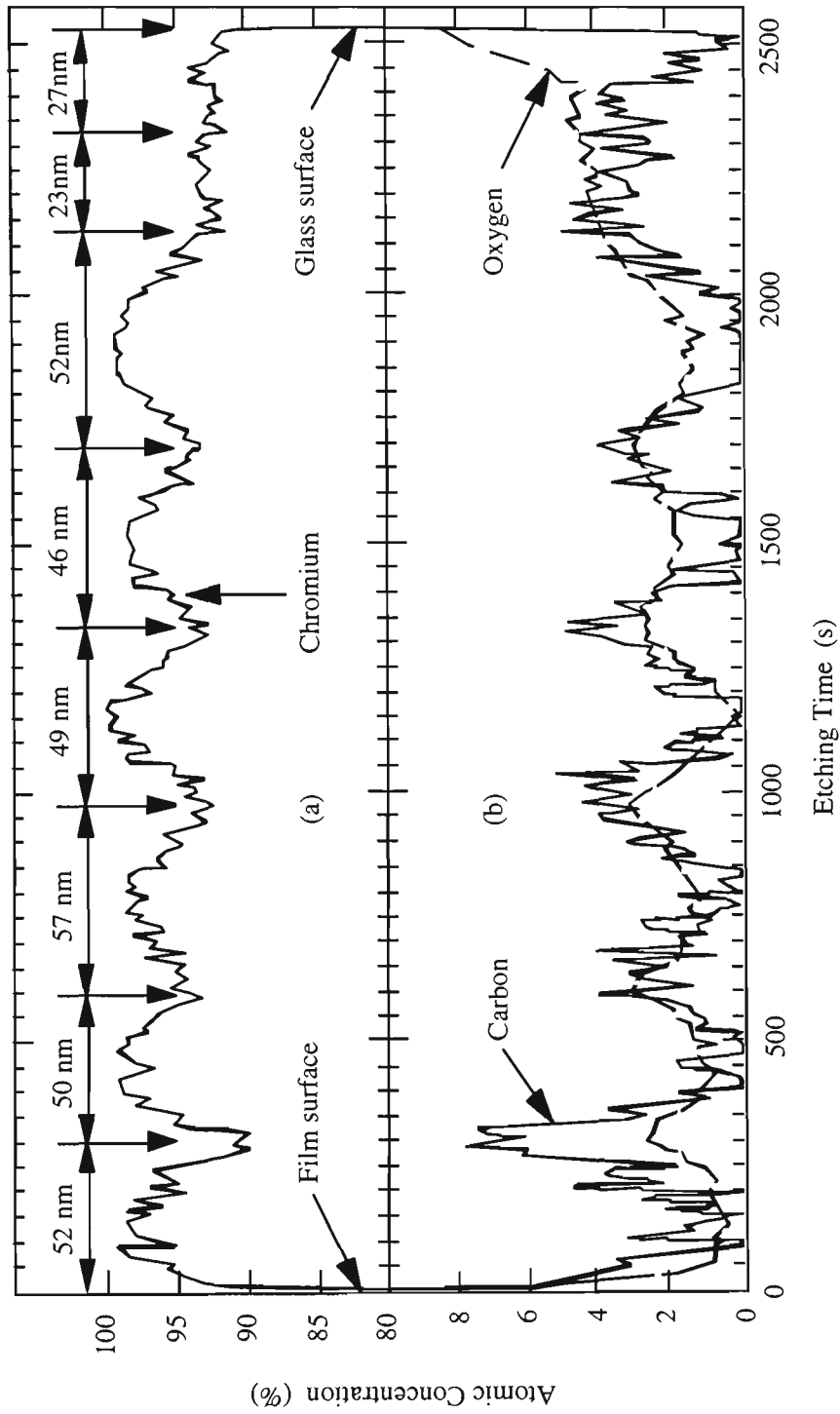


Figure 5.1 The Auger nanoprobe depth-profiles for chromium, oxygen and carbon. The independently measured film thickness is displayed on the diagram. (a) Atomic concentration of Cr, (b) atomic concentrations of carbon and oxygen impurities.

exposed to air for several hours before further coating with additional layers. The measured variation of atomic concentration with depth is shown in Figure 5.1. The depth is given in terms of etching time (at a constant ion dose rate) and the measured thickness of the deposited layers. This profile shows that some oxygen and carbon are present near the surface of each deposited layer, as expected. The innermost layers of Cr (near the glass surface) show the highest fractional oxygen content. Although, only a few percent contamination is present at the film interface, the non-uniformity of the film, which is evident in Figure 5.1, raises some doubts about any interpretation of the stress as being characteristic of Cr films for the particular samples used in these measurements (Abermann, 1990). Since the contamination appears mainly at the film interface, in order to accurately measure Cr stress as a function of film thickness, the sample would have to remain in a vacuum chamber at all times to prevent oxidation.

5.3 Initial results with chromium films (measured in air)

Before presenting data on stress measurements it is useful to clarify the way in which the data is presented and the meaning of the stresses which are plotted in the figures. Data on stress in films is normally presented in terms of force on the thin film layer per unit width of the film. This is equivalent to the average stress in the film times the film thickness since

$$\sigma_f = \frac{F_f}{t_f w_f}. \quad (5.1)$$

Here, σ_f , F_f , t_f and w_f are the average film stress, total force parallel to the substrate surface, thickness and unit width of the film respectively. In the equation above the symbols have exactly the same meaning as they did in chapter 3 where the various relationships between stress and measurable parameters, such as radius of curvature or frequency shift, were derived. In this chapter, figures will be presented as average stress times film thickness or as average stress. For a constant film width, the force divided by width (or average stress times thickness) is the parameter which best represents the force exerted by the film on the substrate or vice-versa. For constant force at the substrate – film boundary, the average stress decreases in proportion to the film thickness.

The radius of curvature and the resonant frequencies of the glass substrate/thin film combination were independently measured in the atmosphere after depositing each successive layer of Cr and the stress of the composite structure calculated using equation 3.66. The results of this calculation are presented in the Table 5.1. Figure 5.2 shows the variation of radius of curvature as a function of total film thickness. The curvature increases as the Cr thickness increases, showing that the total force exerted by the film on the substrate is increasing with film thickness. The relationship between radius of curvature and thickness is clearly non-linear.

Table 5.1 Measured resonant frequencies of the first 8 vibration modes (f_0) as a function of film thickness (t_f). The frequency shifts from the uncoated values (Δf_n) are also given as are the measured radius of curvature (lever method) and the calculated average stress (σ). This data was obtained by removing the sample from the vacuum chamber after each coating layer and making the measurements in air.

f_1 (Hz)	Δf_1 (Hz)	f_2 (Hz)	Δf_2 (Hz)	f_3 (Hz)	Δf_3 (Hz)	f_4 (Hz)	Δf_4 (Hz)	f_5 (Hz)	Δf_5 (Hz)
394.0	6.0	1462.0	19.0	2222.0	15.0	3328.0	16.0		
400.0	12.0	1471.0	28.0	2233.0	26.0	3337.0	25.0		
406.0	18.0	1504.0	61.0	2248.0	41.0	3372.0	60.0	4282.0	12.0
416.0	28.0	1532.0	89.0	2287.0	80.0	3396.0	84.0	4316.0	46.0
450.0	62.0	1565.0	122.0	2341.0	134.0	3436.0	124.0	4346.0	76.0
496.0	108.0	1594.0	151.0	2398.0	191.0	3474.0	162.0	4367.0	97.0
540.0	152.0	1615.0	172.0	2453.0	246.0	3509.0	197.0	4389.0	119.0
593.0	205.0	1633.0	190.0	2514.0	307.0	3551.0	239.0	4407.0	137.0
686.0	298.0	1677.0	234.0	2648.0	441.0	3631.0	319.0	4446.0	176.0
784.0	396.0	1774.0	331.0	2838.0	631.0	3746.0	434.0	4509.0	239.0

f_6 (Hz)	Δf_6 (Hz)	f_7 (Hz)	Δf_7 (Hz)	f_8 (Hz)	Δf_8 (Hz)	t_f (nm)	R(m)	R^{-1} (m^{-1})	σ (MPa)
5356.0	16.0					8.7	4.55	0.22	4881.2
5368.0	28.0					18.1	3.03	0.33	3.524.0
5390.0	50.0	7110.0	10.0	9853.0	18.0	35.9	1.54	0.65	3500.4
5421.0	81.0	7139.0	39.0	9877.0	42.0	53.5	0.97	1.03	3723.1
5466.0	126.0	7176.0	76.0	9922.0	87.0	71.6	0.78	1.28	3468.2
5504.0	164.0	7208.0	108.0	9959.0	124.0	89.4	0.6	1.67	3611.3
5540.0	200.0	7237.0	137.0	9987.0	152.0	108.7	0.52	1.92	3425.1
5581.0	241.0	7262.0	162.0	10019.0	184.0	127.2	0.44	2.27	3459.6
5665.0	325.0	7365.0	265.0	10085.0	250.0	179.7	0.36	2.78	2993.4
5808.0	468.0	7424.0	324.0	10170.0	335.0	269.4	0.27	3.77	2711.4

Figure 5.3 shows the relationship between change in resonant frequency (as measured by the fibre interferometer) and inverse radius of curvature for a selection of measured frequencies. In order to plot this data using a common axis, the frequency shift is plotted rather than the actual frequency. No measurements were made of the resonant frequency of the uncoated flat substrates so the frequency shifts were roughly obtained by simply extrapolating the data and estimating the

uncoated frequency from the intercept on the frequency axis. It should be noted that, for all resonant modes, the relationship between the resonant frequency and the

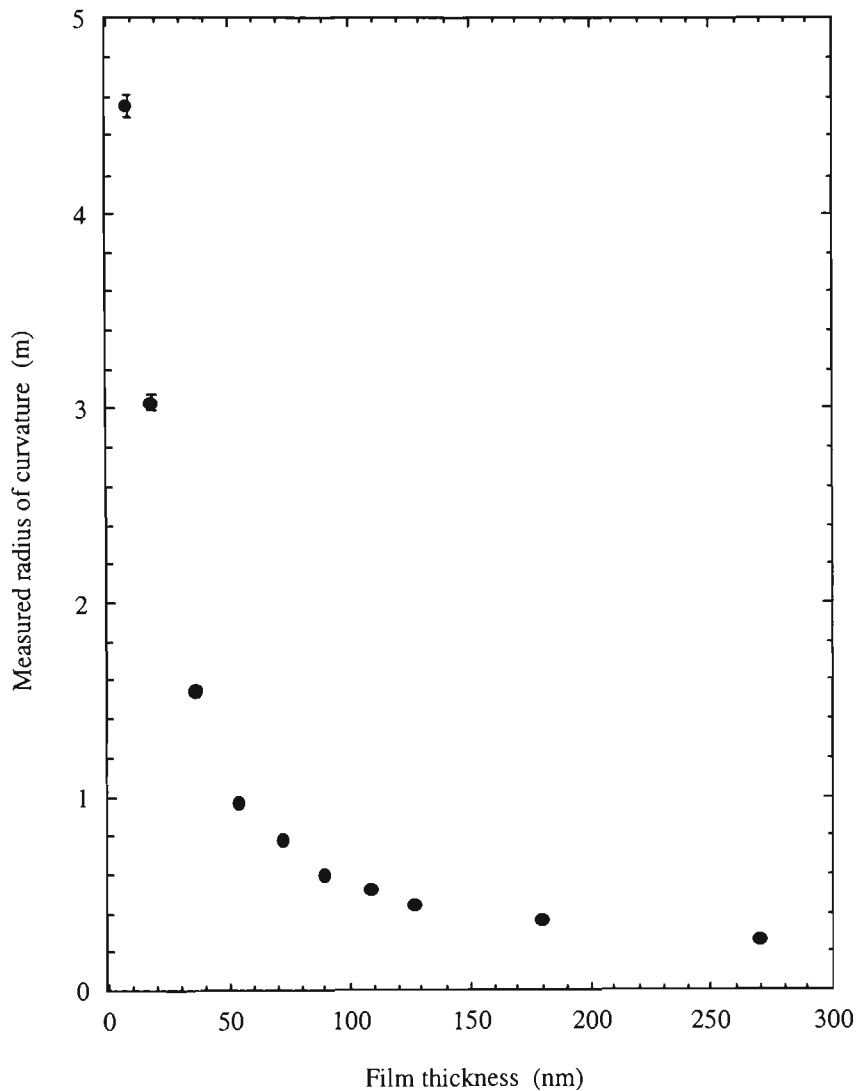


Figure 5.2 Variation of radius of substrate/film curvature with total deposited film thickness for a chromium film. The measurements were made in the atmosphere. The radius of the curvature was measured using lever method.

inverse radius of curvature is not a linear function and the uncoated resonant frequency was difficult to determine with an uncertainty less than about 10%. All the resonant frequencies of the sample varied systematically with wafer curvature and thus any one of the modes could be used to determine the stress. The modes with

frequencies of about 7.1 kHz and 9.8 kHz were not plotted in Figure 5.3 in order to avoid cluttering up the figure. These modes showed similar monotonic variations of frequency shift with curvature.

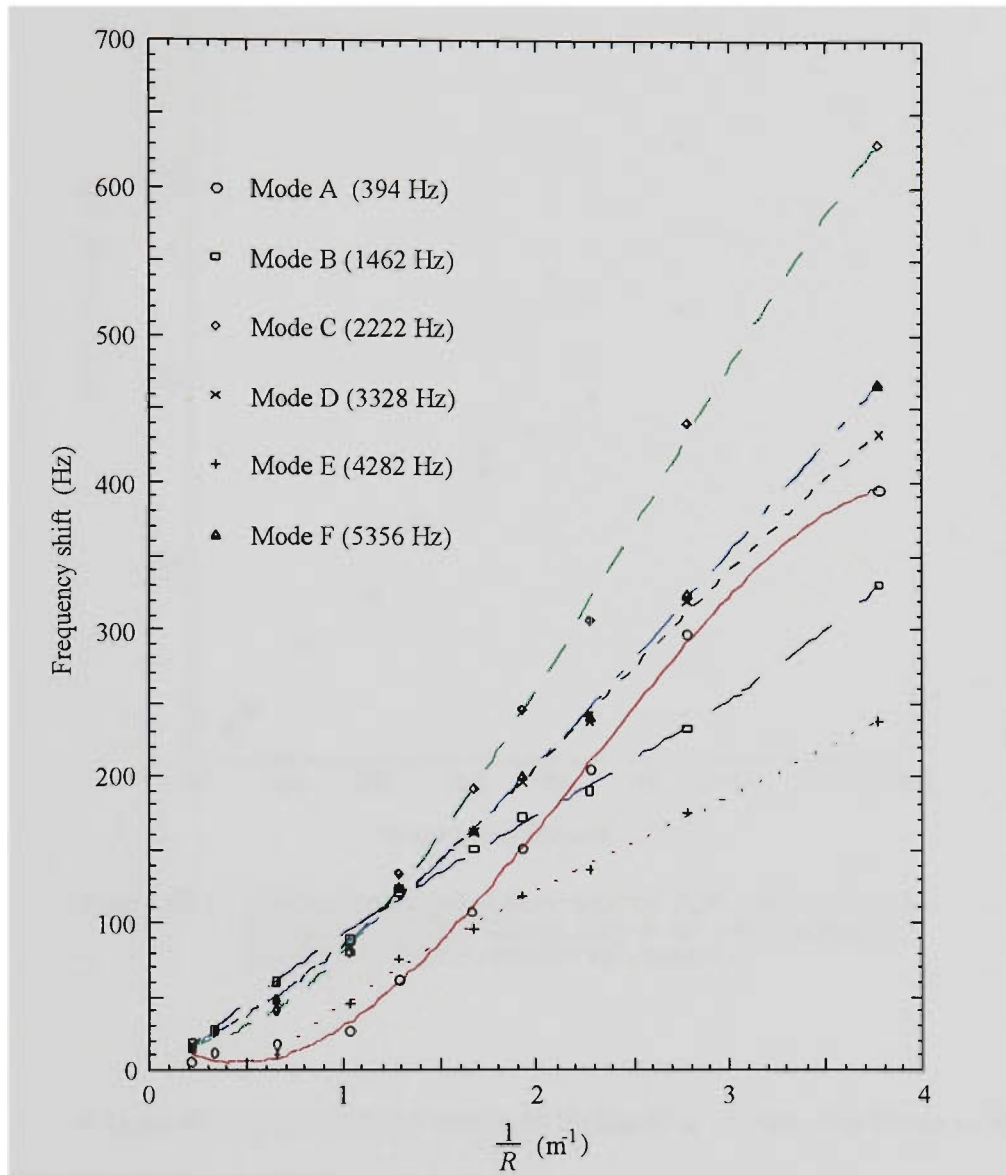


Figure 5.3 Measured variation of resonant frequency shift with the inverse radius of curvature measured using lever method for some different vibrationa modes. The data was obtained after each deposited chromium film laye was exposed to the atmosphere. The lines are a guide to the eye.

Equation 3.66 shows that for uniform films the inverse of the radius of curvature should be proportional to the product of stress and film thickness. Figure 5.4 shows some typical plots of frequency shift as a function of this product.

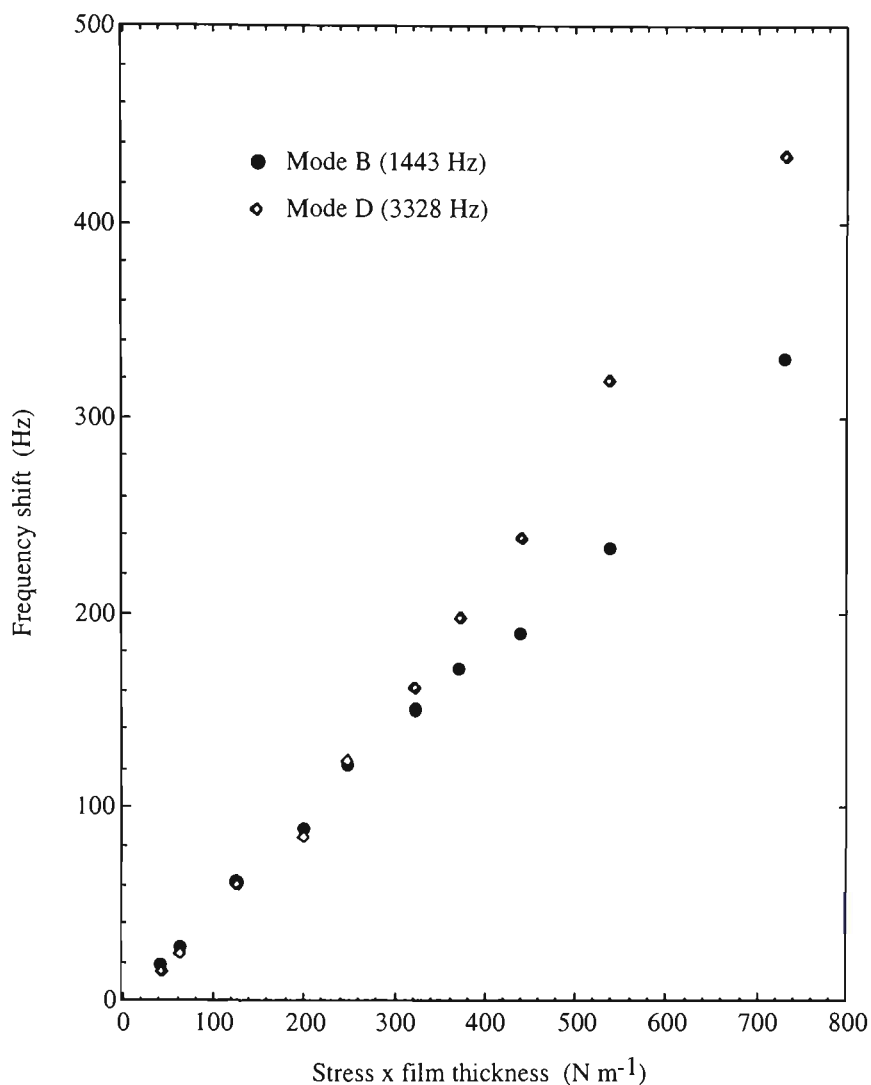


Figure 5.4 The resonant frequency shift versus the product of thickness and stress determined via equation 3.66 for successive deposition of the chromium film measured in the atmosphere.

A typical plot of average stress as a function of film thickness is shown in Figure 5.5. It should be noted that the error in the stress arises mostly from the uncertainties in obtaining independent measurements of film thickness (using a quartz crystal thickness monitor) and the radius of curvature (using the optical lever). The current measurements of resonant frequencies were made after varying periods of exposure of the films to the atmosphere (~2-3 hours) and should be seen as a proof of this technique rather than as a measurement of stress in pure Cr thin films. The

average stress, for our slightly oxidised and contaminated films, shows a generally decreasing magnitude with increasing film thickness.

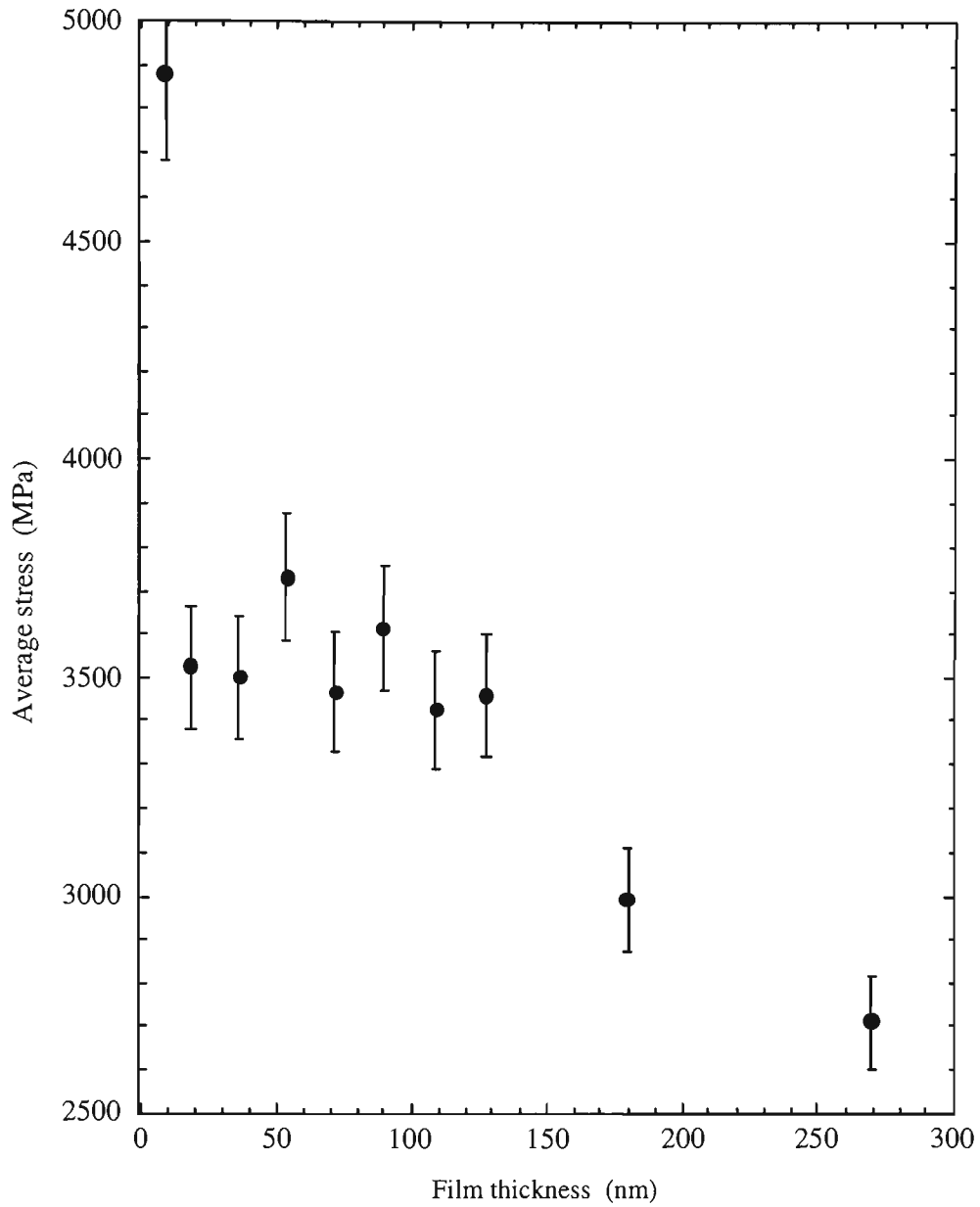


Figure 5.5 Stress as a function of film thickness for Cr films deposited on a glass substrate. The stress has been determined from the curvature of the glass plate using equation 3.66 and is measured in the atmosphere.

5.4 Measurements of stress when the rear surface of the sample was coated with a thin titanium film

The previous measurements suffered from two main problems:

- (i) It was very difficult to obtain frequency shifts since the resonant frequency of uncoated samples (starting frequency) could not be obtained reliably by extrapolating curves of unknown functional form.
- (ii) The removal of the specimens from the vacuum system to make measurements in the atmosphere led to contamination of the film.

In the following measurements, changes were made to try to overcome the first of these problems (later in this chapter, problem (ii) is also addressed). Glass substrates, with the same dimensions as in previous experiments, were cleaned using the cleaning process described in section 4.3.1. The rear surface of the plate was then coated with 20 nm of titanium film by sputtering from a magnetron source. Then, a metal rod was glued to the centre of the rear surface of the substrate using the jig shown in Figure 4.4. The sample was then placed in an aluminium holder (shown in Figure 4.5) and the curvature and resonant frequencies were measured using the optical lever (section 4.3) and the interferometric technique (section 4.6.3), respectively. With careful attention to the process of coating of the titanium film and gluing the metal rod on the rear surface, an almost flat sample can be produced. No significant movement of the reflected spot could be detected when the radius was

measured by translation of the mirror (Figure 4.6) and application of equation 4.1. In practical terms this means the radius was greater than about 120 m. The sample, supported by the metal rod in an aluminium holder, was placed in the vacuum system and the first layer of Cr was then deposited.

Again, the radius of curvature and the resonant frequencies of the sample were measured in the atmosphere after deposition of each successive layer of Cr. This process was repeated until the sample had been coated with eight layers of Cr. During the process of coating the substrate, measurement of the radius of curvature and resonant frequencies, the sample was not removed from the aluminium holder (Figure 4.5) but it was removed from the vacuum chamber after each layer was coated.

Figure 5.6 shows the variation of radius as a function of film thickness and the shape of the curve is very similar to the curve shown in Figure 5.4. Figure 5.7 shows a typical relationship between change in resonant frequency as measured by the fibre interferometer and inverse radius of curvature for a selection of measured frequencies. The resonant frequency of the titanium-coated flat substrates was measured, so the frequency shifts were obtained by simply subtracting this data from the data when the samples were subsequently coated by Cr. All the resonant frequencies varied systematically with wafer curvature. The data shows a monotonic increase in resonant frequency with inverse radius of curvature.

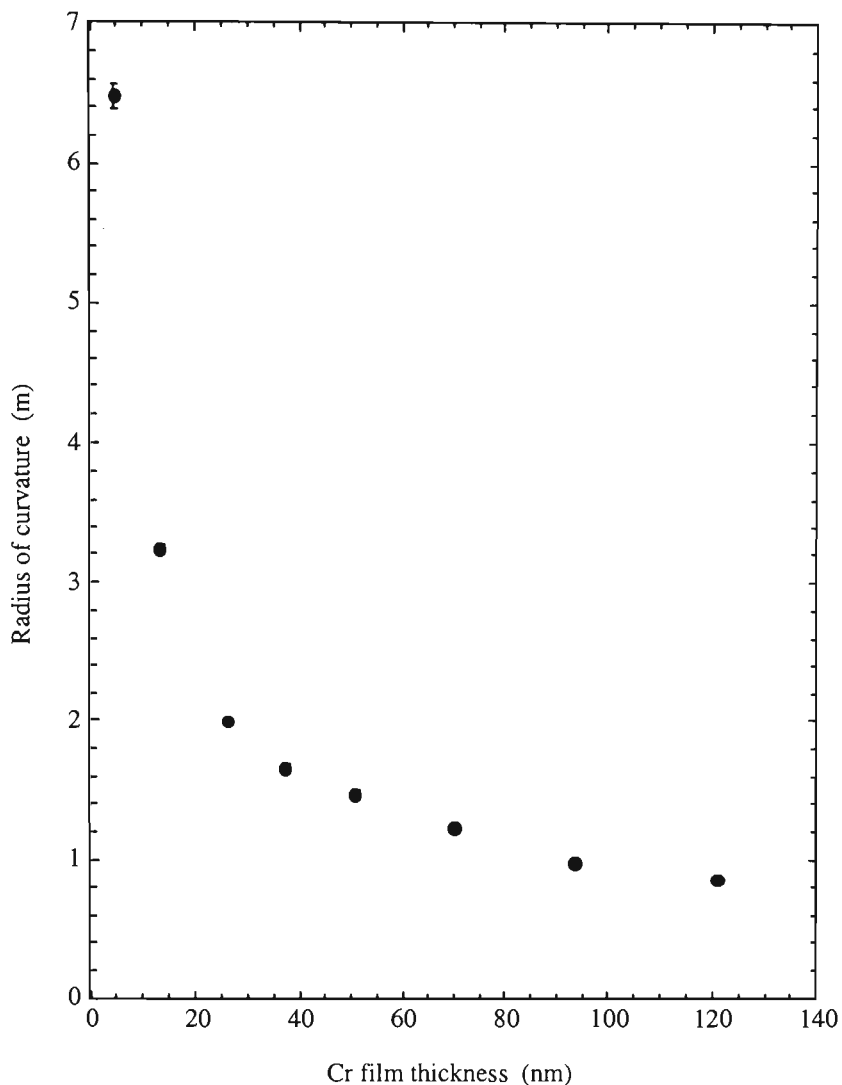


Figure 5.6 Variation of radius of substrate curvature, measured using the lever method, with Cr film thickness. The measurements were made by removing the sample from the vacuum system after each successive layer of Cr was deposited. Samples were coated with an initial 20 nm layer of Ti in order to measure the resonant frequency before Cr deposition.

Figure 5.7 shows a plot of frequency shift as a function of substrate curvature. A typical plot of average stress as a function of film thickness is shown in figure 5.8. The stress for our partially oxidised films shows a much smoother, monotonically decreasing, curve with increasing film thickness than was the case with the initial results (Figure 5.5). One likely reason for such behavior is that the samples were exposed to air for no more than 40 minutes before further coatings.

Therefore, the oxidation and contamination of the Cr film was likely to be substantially reduced compared to the initial measurements reported in section 5.5.

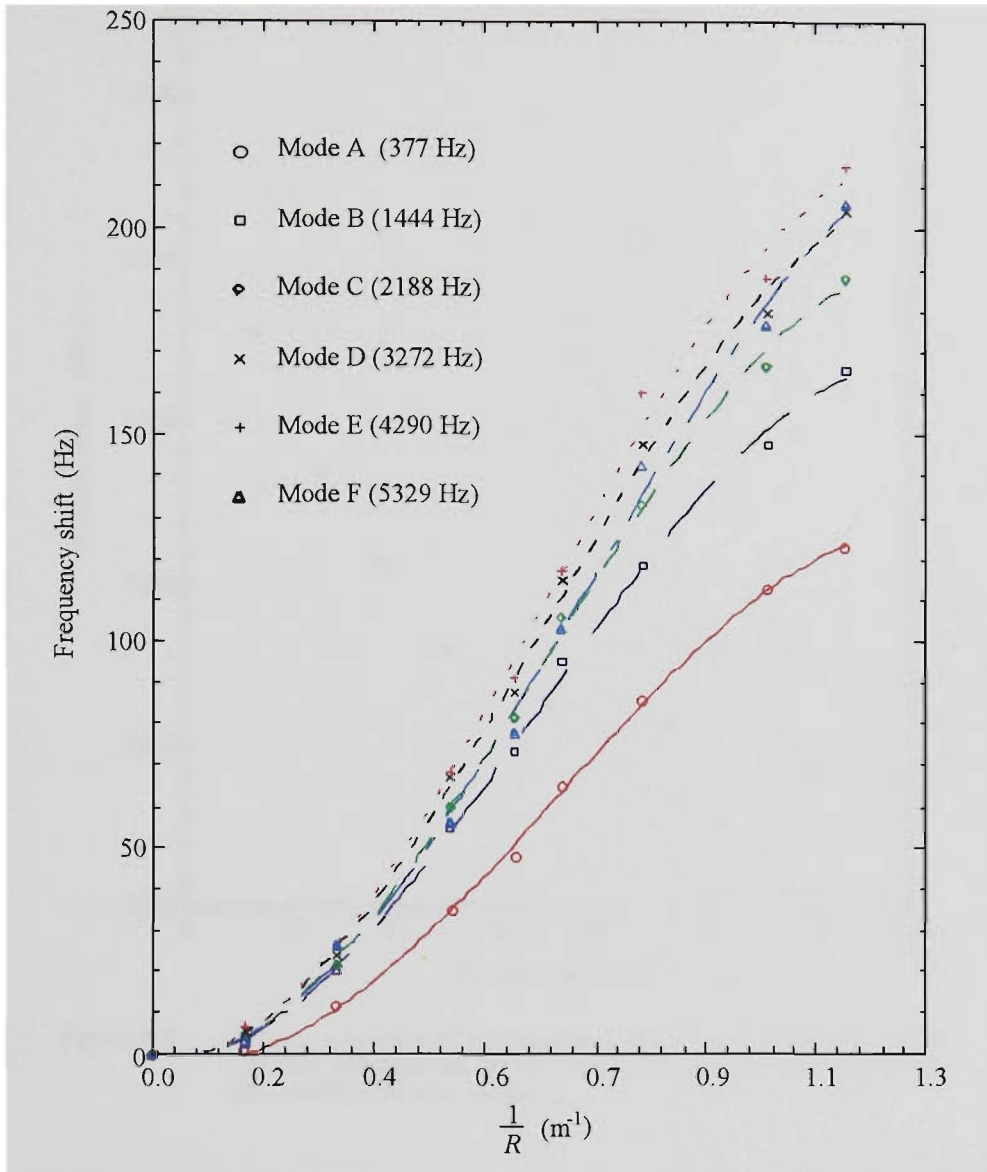


Figure 5.7 Typical measured variation of resonant frequency shift with the inverse radius of substrate curvature (obtained using the lever method) for some vibrational modes of the samples coated with titanium on the rear surface. The measurements were taken in the atmosphere after deposition of each chromium layer. The lines are merely a guide to the eye.

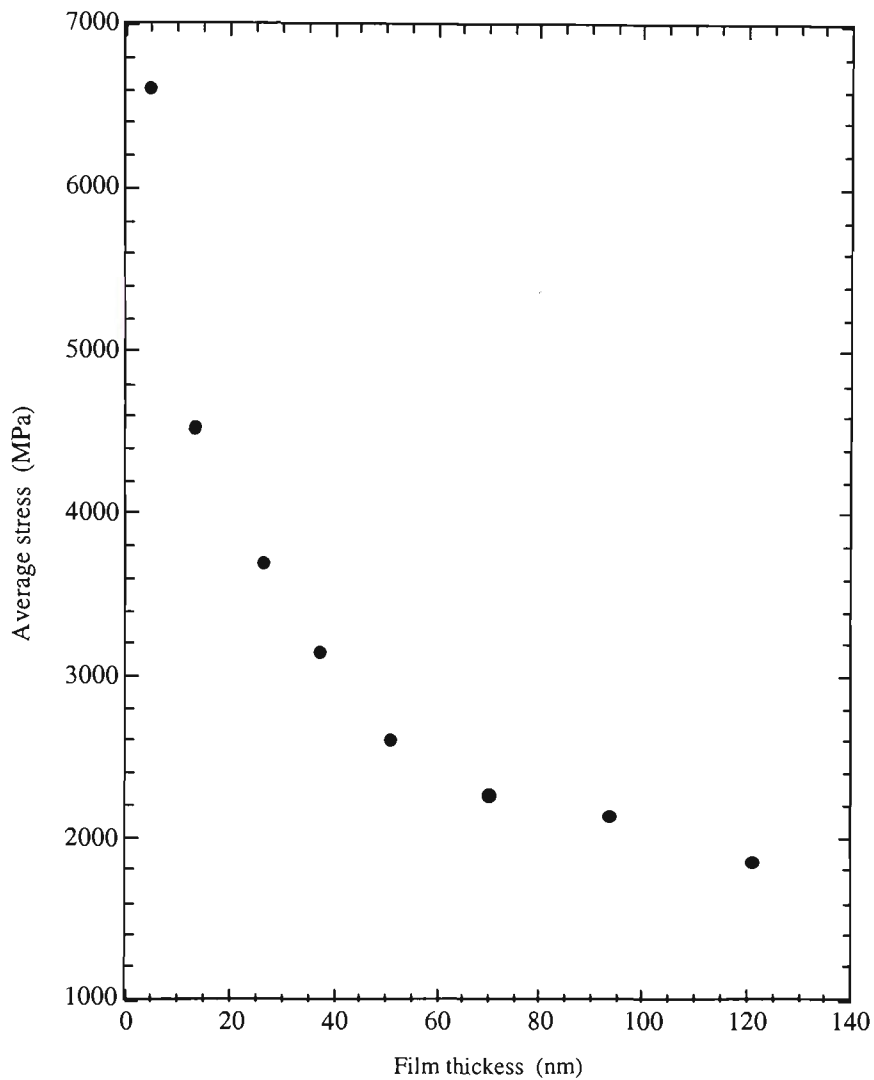


Figure 5.8 Stress as a function of film thickness for Cr films coated on a glass substrate with titanium film on the rear surface. The measurements were made in the atmosphere.

Figure 5.9 shows some typical plots of change of frequency as a function of the product of stress and film thickness. Again, frequency shift is used so that the data for the two chosen modes may be displayed using the same axis.

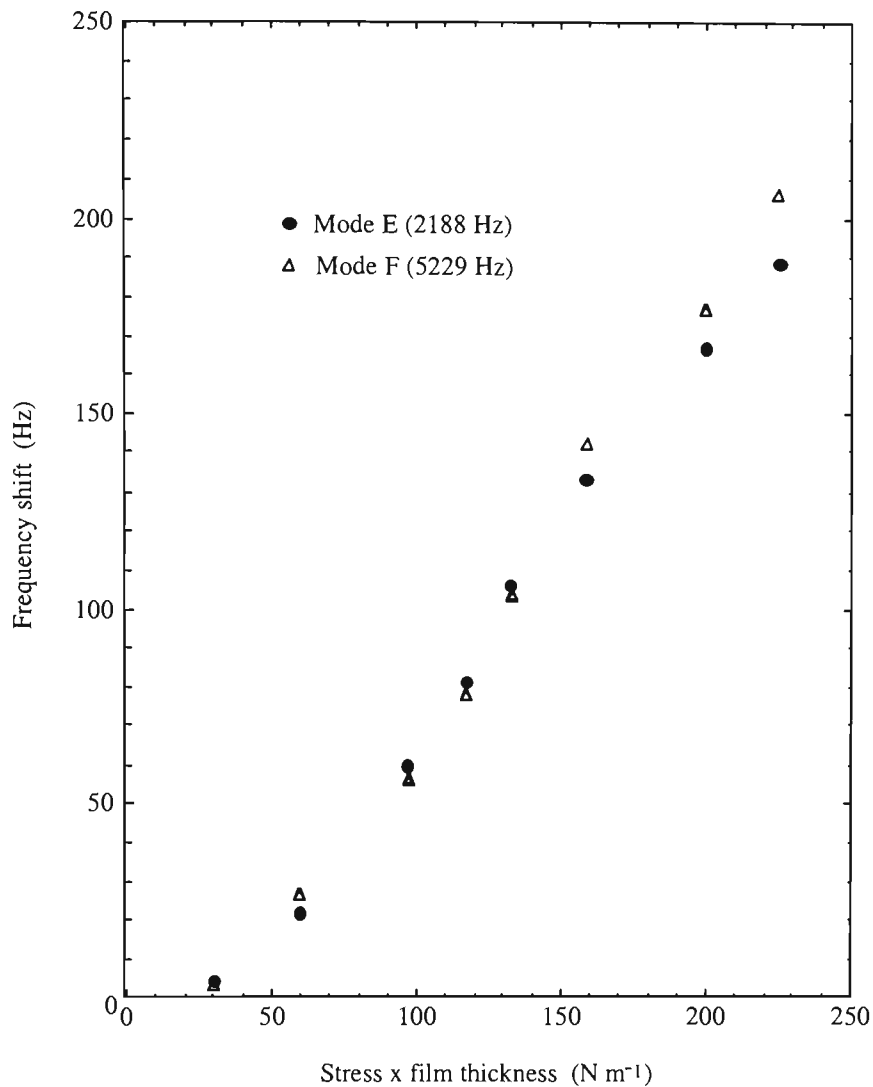


Figure 5.9 Resonant frequency shift versus the product of thickness and stress determined via Equation 3.66 for a sample coated with titanium on the rear surface. The measurement were made for chromium films in the atmosphere.

The second set of atmospheric measurements is clearly superior to the first in that the resonant frequency was determined before Cr coatings were applied and also the exposure time to the atmospheric contaminants was reduced. However, the two sets of results which are shown in Figures 5.2 - 5.5 and 5.6 - 5.9 are broadly similar. These curves show generally monotonic variations when one parameter is plotted against another but since there is obviously significant atmospheric contamination (Figure 5.1) it is difficult to make quantitative conclusions about the

nature of the stress in these Cr films. To obtain meaningful data would require measurements made within the vacuum system so that atmospheric contamination is not a factor. Such measurements are presented in the next section. The disadvantage of making measurements inside a vacuum system is that it is not possible to make meaningful independent measurements of radius (R) using the lever method for comparison with the frequency shifts determined by the interferometer. These atmospheric measurements certainly demonstrate that the frequency shifts accompanying deposition of thin film coatings can certainly be measured and these shifts represent another parameter which can be used to indicate changes in stress for thin film coatings.

5.5 Experimental results for *in situ* measurements

In this section experimental results are presented for real-time measurements on Cr and MgF₂ films under controlled conditions inside a vacuum chamber. However, under real deposition conditions, frequency shifts are also produced by differential heating and non-uniform temperature distribution in the sample.

Before coating the sample with a thin film, the effect of thermal cycling was investigated for a number of glass/Ti substrates. For these measurements, the substrate was placed in the vacuum system and exposed to radiant heat from an empty evaporation boat which had previously been outgassed. The sample was placed 15cm

above the evaporation boat. This distance was limited by the size of the bell jar of the vacuum system. To obtain an indication of the surface temperatures of the substrate during an evaporation cycle without affecting the resonant frequency, thermocouples were placed about 1mm from the front and rear surfaces. While these thermocouples did not accurately record the surface temperature, they do show similar trends during radiant heating and can be used to indicate when the surface has returned to its original temperature following a heating/cooling cycle. It was found that the resonant frequency of the substrate decreased when the temperature of the sample increased. A typical plot of resonant frequency shift as a function of temperature for the front surface (as indicated by front surface thermocouple) is shown in Figure 5.10. A similar graph was obtained for the rear surface except that the temperature was lower than the temperature of front surface by about a factor of two. The resonant frequency shift is very sensitive to the temperature variations, mainly due to temperature dependence of Young's modulus of the glass substrate (Kaye and Laby, 1973)

$$E_s(T) = E_0 [1 - \alpha_0 (T - T_0)] \quad (5.2)$$

Here E_0 and α_0 are the Young's modulus and its temperature coefficient at the ambient temperature T_0 . The variation in Young's modulus with temperature produces a negative modal frequency shift as the temperature rises. Using values of E_0 and α_0 at room temperature for glass (Kaye and Laby, 1973) the approximate magnitude of the changes observed agrees reasonably well with the shift shown in Figure 5.10. The positive resonant frequency shift evident in the latter stages of the cooling cycle may be due to the thermal stress resulting from the difference between the thermal

expansion coefficients of the titanium film and substrate. The substrate will be bent with a slight concave curvature due to small difference in temperature coefficients of titanium film ($\alpha_{Ti}=8.6 \times 10^{-6} \text{ K}^{-1}$; Ohring, 1992) and substrate ($\alpha_{\text{Substrate}}=7.4 \times 10^{-6} \text{ K}^{-1}$, see Appendix I). The different paths followed by the heating and cooling phases of Figure 5.10 are probably due to the very different timescales associated with the heating and cooling temperature changes.

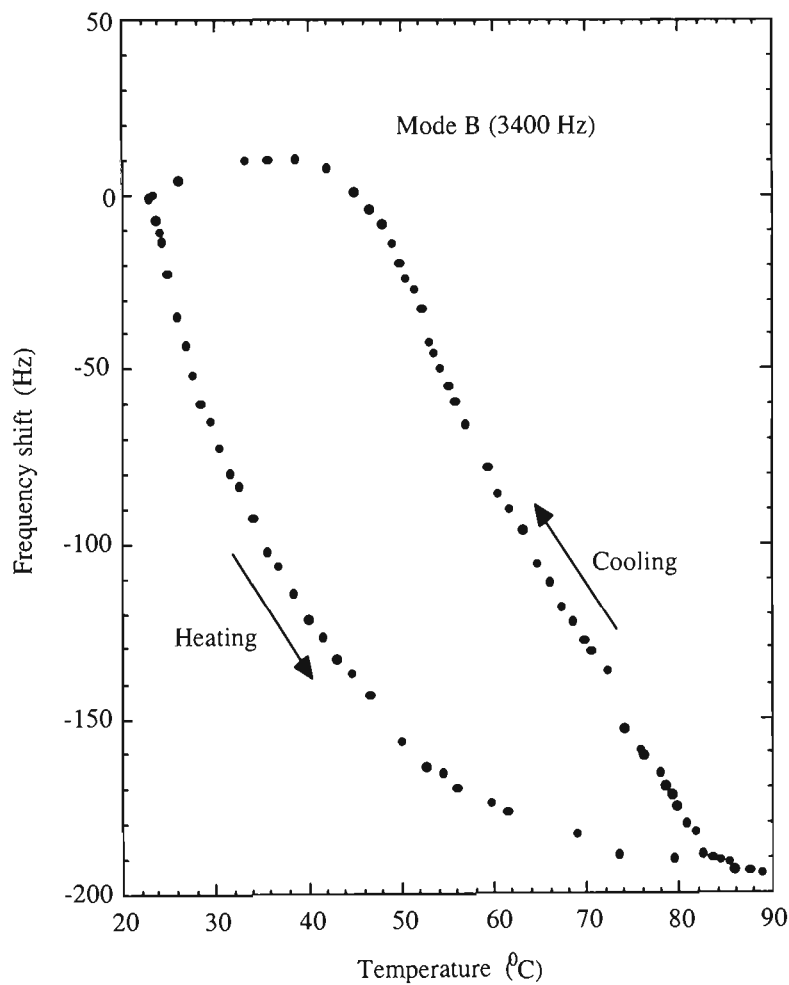


Figure 5.10 *In situ* measured variation of resonant frequency shift of the glass sample coated with titanium on rear surface, versus temperature. The temperature measurements were made using a thermocouple near the front substrate surface.

The thermal cycling, previously described, was repeated three times on each sample for a number of glass/Ti substrates. Similar graphs to that shown in

figure 5.10 were obtained on each occasion. From this figure, it is clear that the frequency shift always returns to the initial point after the process of heating and cooling a glass/Ti substrate. This indicates that the thermal cycling process of the samples is reversible and it does not change permanently the resonant frequency of a substrate. Therefore, one can conclude that temperature rises accompanying the deposition of the thin film do not affect the final measured resonant frequency shift of the substrate/thin film structure provided the structure is allowed to first return to ambient temperature. When all measurements are made at the same uniform temperature, frequency shifts are due only to changes of the curvature of the substrate caused by the stress in the deposited thin film. If frequency shift measurements are made during a continuous deposition, then some thermal changes will be present and hence a component of the observed frequency shift will be thermal in origin.

Figures 5.11 and 5.12 show the measured variation of resonant frequency of the 3400 Hz mode as a function of film thickness for chromium and magnesium fluoride films respectively. These measurements were made in real time during the continuous film deposition and hence will contain some thermal effects. For these measurements, no shutter was used and the evaporation current was slowly raised while the substrate was exposed to the radiant heat. Hence the resonant frequency initially decreased due to the temperature rise before any coating occurred. Once the coating commenced, positive (stress-induced) frequency shifts occurred. The shift as a function of film thickness for one continuous coating run is shown in the figures. For this data, the deposition rate for chromium was about 10 Å/sec and for magnesium fluoride about 40 Å/sec. It is estimated from the frequency shift before

coating commences that the temperature of the front and rear surfaces during coating was between 90-120 °C and 40-80°C respectively. During film deposition, the resonant frequency of the film/substrate composite will increase mainly due to the changes in the curvature caused by the residual stress developed in thin film. Figures 5.11 and 5.12 show a fairly linear variation of frequency shift during coating with film thickness. The fact that the slope is constant during deposition is a good indication that the thermal stress and substrate temperature did not vary significantly during the coating. This was confirmed by the thermocouple monitors.

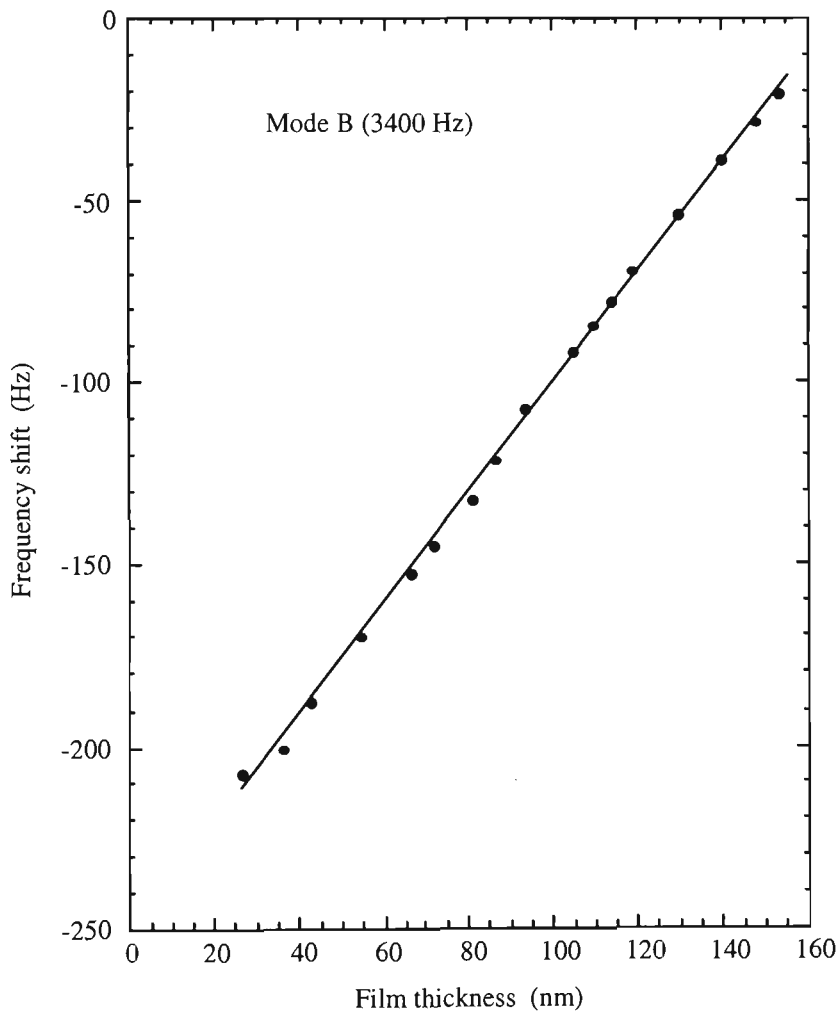


Figure 5.11 Measured variation of resonant frequency shift with film thickness during the deposition of chromium. Under these conditions temperature changes also occur.

Detailed interpretation of the previous set of results is complicated by the existence of stresses produced by both thermal and thin film effects. In order to avoid this

problem, further sets of measurements were conducted for which all frequency measurements were made at the same ambient temperature and hence thermal effects

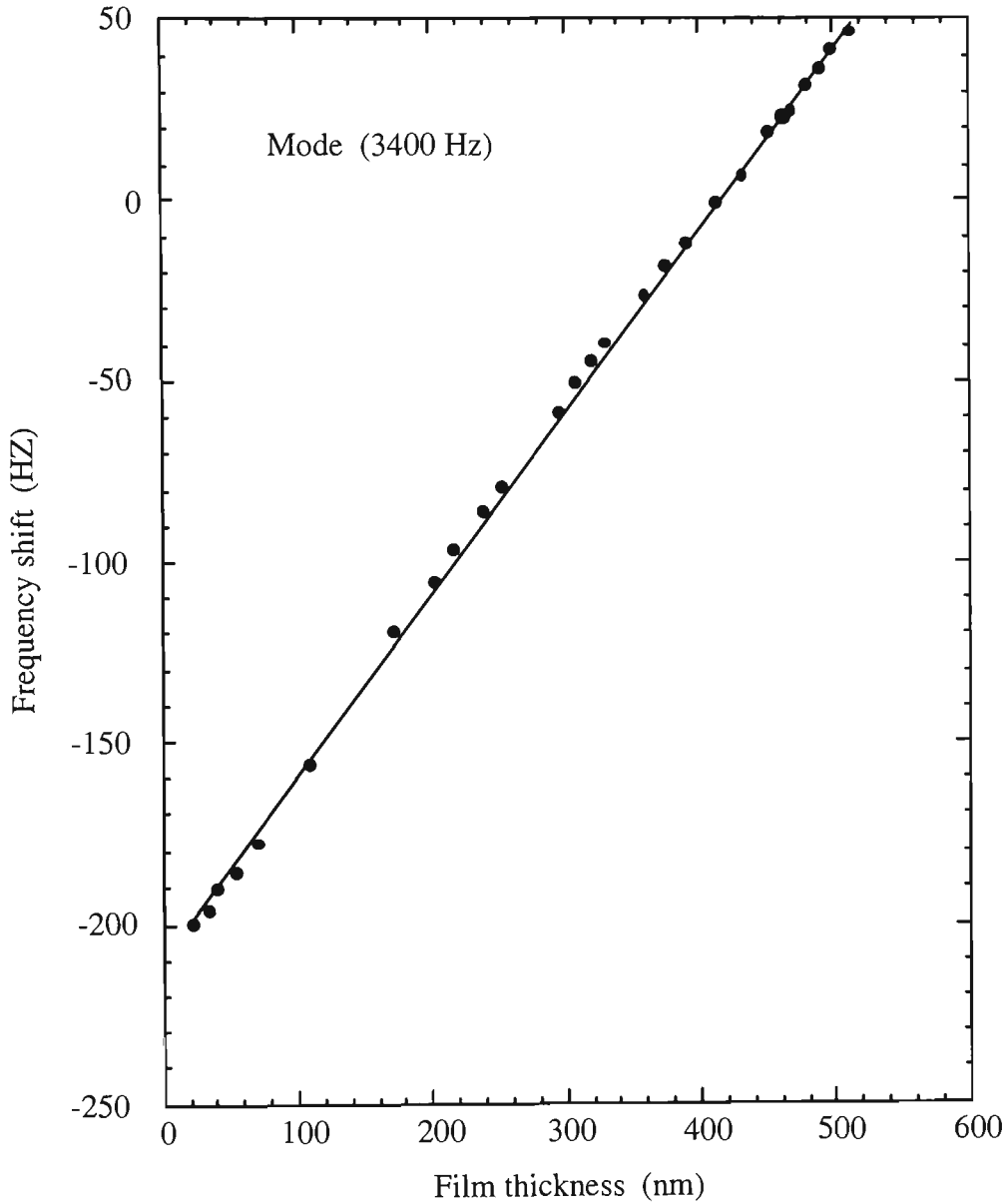


Figure 5.12 *In situ* measured variation of resonant frequency shift during the deposition of MgF₂. Under these conditions temperature changes also occur.

should not be present. For these measurements a shutter was used to control coating and shield the substrate from radiant heat when coating was not in progress. The measurement technique involved sequential deposition of eight layers, each with a

thickness of around 10 – 40 nm. After deposition, the coated substrate was allowed to cool back to the ambient temperature before a resonant frequency was measured. The return of the coated substrate temperature to ambient was monitored by the thermocouples and even though the temperature rise during coating was only about 60 °C, the return to ambient took 3 – 4 hours after deposition of each layer.

The data obtained from these measurements is tabulated in tables 5.2 and 5.3 and plotted in Figures 5.13 and 5.14. If this data is to be used to calculate film stress without independent curvature measurements, then the curvature must be inferred from the frequency shifts. Under these conditions, the measured frequency shift should be corrected for the effect of increased thickness and mass of the resonating structure during coating in order to obtain the frequency shift due to stress-induced curvature. Hence the tables and figures include both measured and “corrected” frequency shifts using equation 3.90. The total film thickness of less than 0.2 μm for Cr and 0.4 μm for MgF_2 is small compared to the substrate thickness of 110 μm . Hence the corrections would be expected to be small and in all cases are less than 5% of the measured frequency shift for the 2300 Hz mode of Cr. For MgF_2 , the overall frequency shifts are smaller and so the corrections are more significant, generally being about 7.5% for the 2300 Hz mode. It can be seen from the tables and the figures that the corrections become even more significant for the higher frequency modes. For the 4700 Hz mode, the measured frequency shifts for Cr and MgF_2 are about 15% and 30% respectively.

Table 5.2 Measured and corrected resonant frequency shift for Cr thin film for three different resonant modes.

t_{film} (nm)	Mode 2300 Hz			Mode 3400 Hz			Mode 4700 Hz		
	$\Delta f_{\text{measured}}$ (Hz)	$\Delta f_{\text{corrected}}$ (Hz)	Δ (Hz)	$\Delta f_{\text{measured}}$ (Hz)	$\Delta f_{\text{corrected}}$ (Hz)	Δ (Hz)	$\Delta f_{\text{measured}}$ (Hz)	$\Delta f_{\text{corrected}}$ (Hz)	Δ (Hz)
14.8	23.9	22.8	1.1	21.5	19.8	1.7	12.3	10.0	2.3
37.4	62.4	59.6	2.8	48.6	44.4	4.2	36.6	30.7	5.9
62.8	109.2	104.5	4.7	83.6	76.5	7.7	60.3	50.4	9.9
84.8	150.1	143.7	6.4	114	104.4	9.6	85.9	72.6	13.3
107.5	193.9	185.8	8.4	145.6	133.5	12.1	108.6	91.7	16.8
129.8	234.9	225.2	9.7	177.7	163.1	14.6	135.2	114.9	20.3
152.4	279.1	267.7	11.4	210	192.9	17.1	161.2	137.4	23.8
181.9	338.5	324.9	13.6	255	234.6	20.4	196	167.6	28.4

Table 5.3 Measured and corrected resonant frequency shift for MgF₂ thin film for three different resonant modes.

t_{film} (nm)	Mode 2300 Hz			Mode 3400 Hz			Mode 4700 Hz		
	$\Delta f_{\text{measured}}$ (Hz)	$\Delta f_{\text{corrected}}$ (Hz)	Δ (Hz)	$\Delta f_{\text{measured}}$ (Hz)	$\Delta f_{\text{corrected}}$ (Hz)	Δ (Hz)	$\Delta f_{\text{measured}}$ (Hz)	$\Delta f_{\text{corrected}}$ (Hz)	Δ (Hz)
15.0	4.8	4.2	0.6	5.0	4.1	0.9	5.1	3.9	1.2
52.4	26.8	24.8	2.0	19.1	16.1	3.0	13.6	9.4	4.2
100.7	51.1	47.2	3.8	36.2	30.4	5.8	25.5	17.4	8.1
157.7	76.6	70.6	6.0	55.6	46.5	9.9	38.8	26.2	12.6
213.5	106.5	98.4	8.1	73.6	61.3	12.3	53.5	36.4	17.1
267.8	133.1	122.9	10.1	92.9	77.5	15.4	67.6	46.2	21.4
329.5	162.2	149.7	12.5	115.6	96.7	18.9	86.4	60.1	26.3
396.2	192.6	177.6	15.0	139.6	116.9	22.7	103.6	72.0	31.6

Figures 5.13 and 5.14 again show a linear variation of frequency shift with film thickness as was the case for the continuous deposition measurements shown in figure 5.11 and 5.12. Direct comparison of the two data sets is complicated by the fact that the same substrate was not used for all measurements. However the substrates were nominally equivalent yet the slope of the measured frequency shift for the continuous coating case was significantly higher than was the slope for the sequential deposition case. For the 3400 Hz mode of Cr these frequencies were about 1.5 Hz/nm (continuous) and 0.35 Hz/nm (sequential). For MgF₂ the corresponding frequencies were 0.5 Hz/nm and 0.35 Hz/nm. It may be that these differences in

slope indicate some difference in structure (and hence stress) for films deposited under different conditions (temperatures and time).

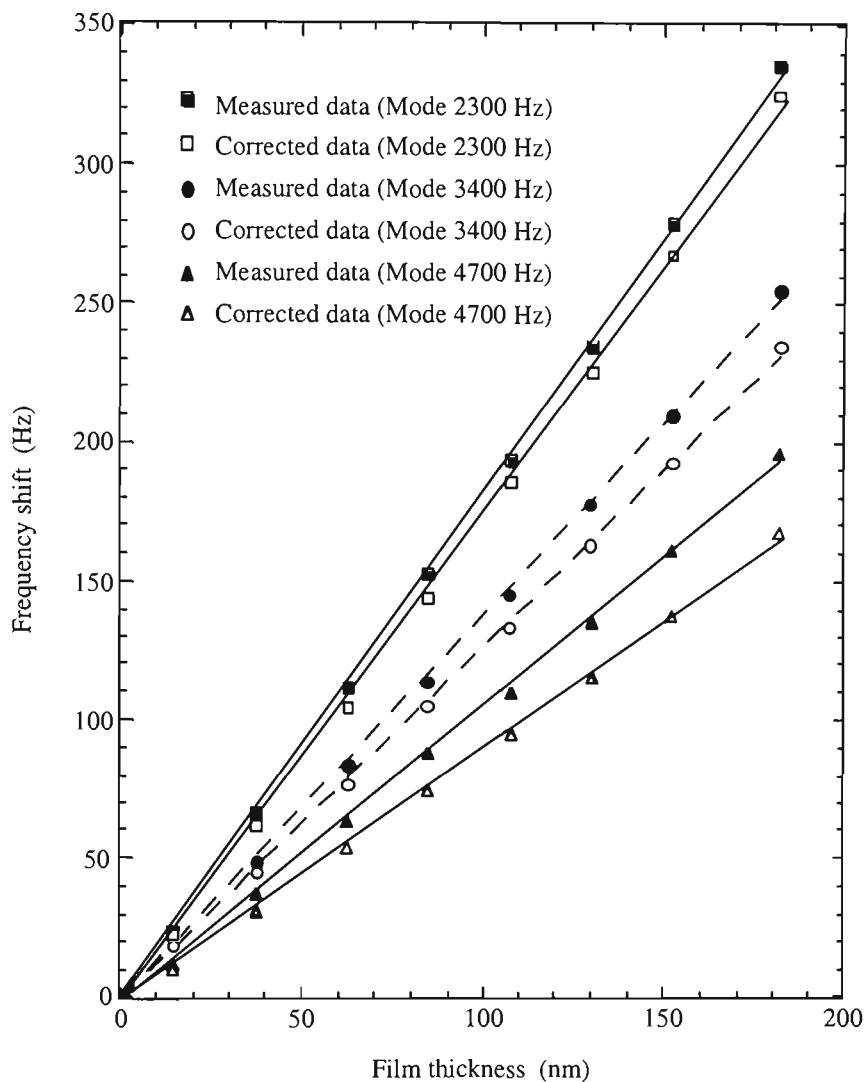


Figure 5.13 *In situ* measured variation of resonant frequency shift with film thickness of chromium for sequential deposition of layers. The substrate was allowed to cool back to room temperature before resonant frequency measurements are made. The lower line for each mode shows the frequency shift after correction by factor $\Psi^{1/2}$.

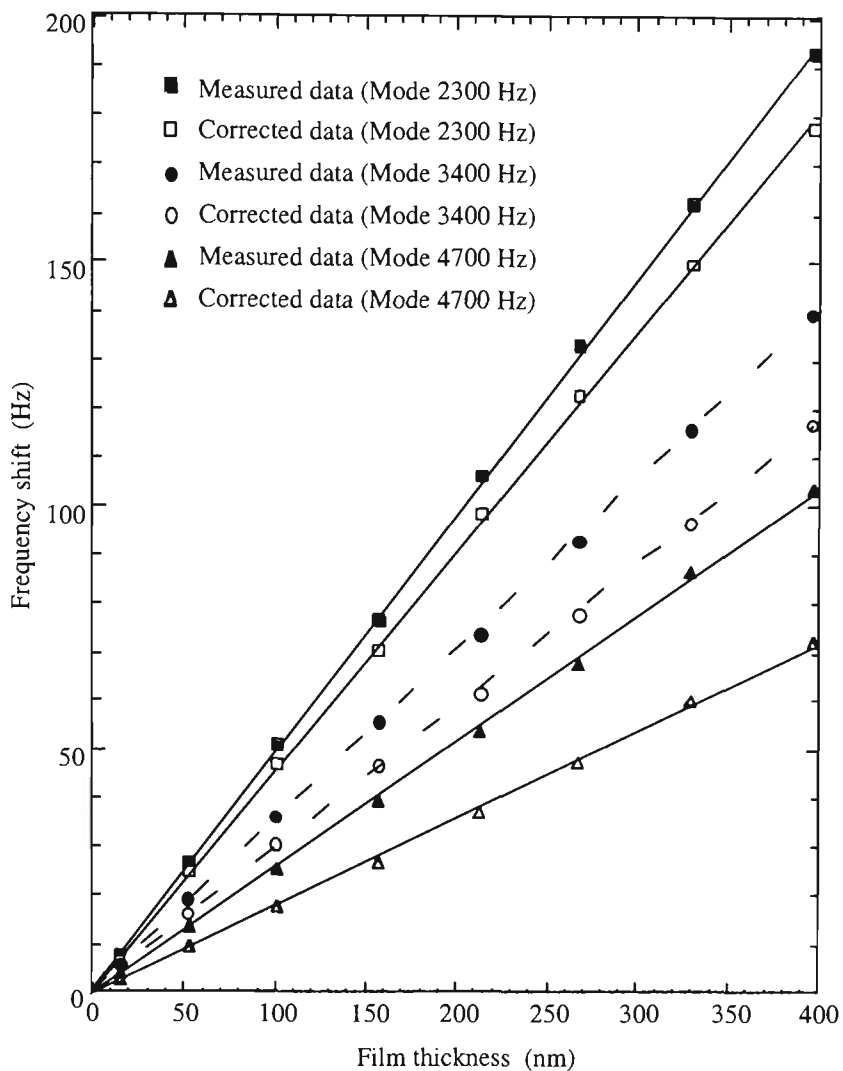


Figure 5.14 *In situ* measured variation of resonant frequency shift with film thickness of magnesium fluoride for sequential deposition (constant temperature for measurement). The lower line for each mode shows the frequency shift after being corrected by factor $\Psi^{1/2}$.

Figures 5.15 and 5.16 show the average stress as a function of thickness for Cr and MgF_2 films. These figures are calculated using equation 3.89 and the 3400 Hz mode data of tables 5.2 and 5.3. Note that the calculated stress should be independent of which mode is used for the calculations and in fact very similar data is obtained for all measured modes. Figures 5.15 and 5.16 show data calculated using both measured and corrected frequency shifts and the variation of average stress with thickness for these two cases is quite similar. Correction of the data to allow for the

thickness and mass of the coating results in a decrease of the calculated stress by less than 10% for both Cr and MgF₂ films.

Figure 5.17 shows another plot of average stress against film thickness for Cr and MgF₂ films. Here the data is plotted on a log-log plot and the results are excellent straight lines with slopes and standard errors of -0.497 ± 0.009 for Cr and -0.496 ± 0.003 for MgF₂. Thus for this thickness range of these films, which are deposited within the vacuum system without atmospheric contamination, the average stress varies as $\sqrt{t_f}$. Although no independent measurements were made of the curvature as a function of film thickness, this stress variation, together with equation 3.66, suggests that the curvature varies as $\sqrt{t_f}$. This result is consistent with the linear variations of resonant frequency with film thickness (Figures 5.13 and 5.14). A log-log plot of the radius data for sequential layers measured in the atmosphere (Figure 5.17) appears to confirm this result with the slope of -0.489 ± 0.0187 . Appropriate re-plotting of data presented by Klokholm and Berry (1968) for Cr films of thickness up to about 150 nm on glass substrates shows a slope very close to -0.5 . A similar result is obtained using the data of Pulker (1984) for Cr films of thickness up to 100 nm, again on a glass substrate. It should be noted that this $\sqrt{t_f}$ variation does not apply to all types of films, with much more complicated variations being observed with other films and thickness ranges (Klokholm and Berry, 1968). The

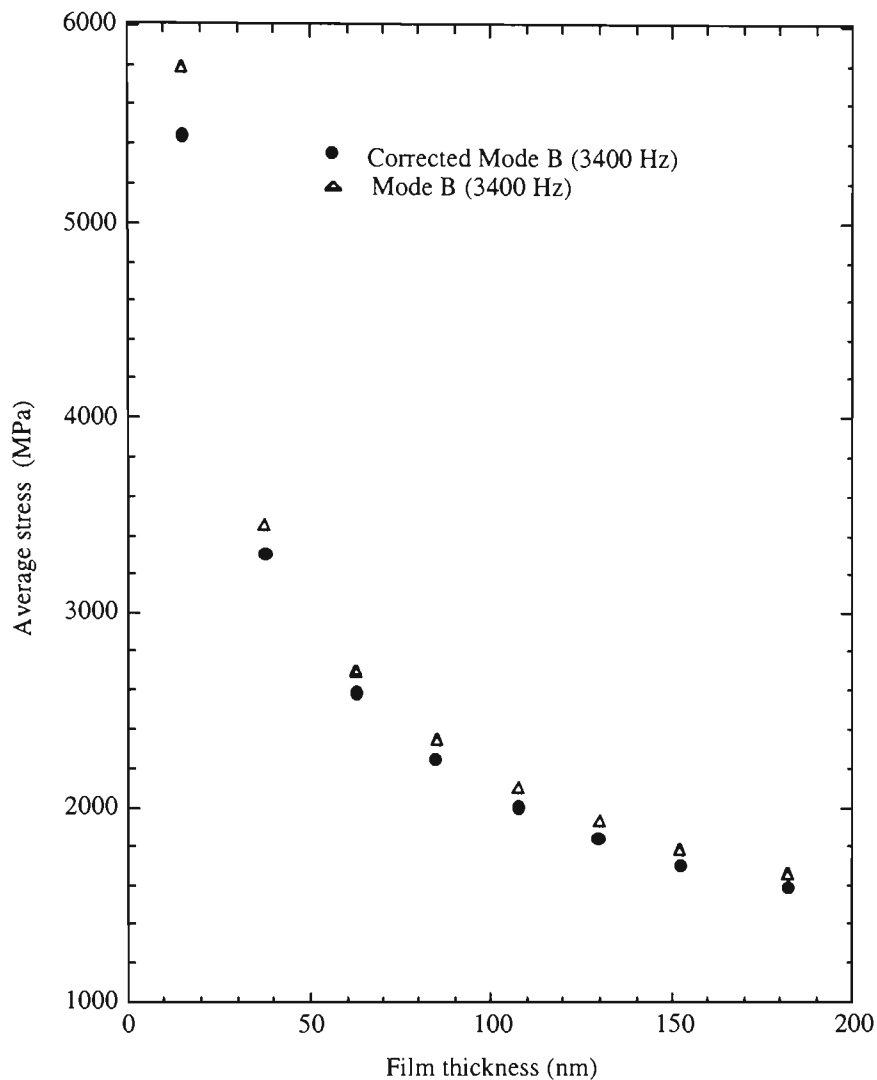


Figure 5.15 Stress as a function of film thickness for sequential deposition of a Cr film at room temperature in the vacuum system. The lower points (full circles) have been corrected using the $\psi^{1/2}$ factor.

magnitudes of the stresses measured in this work are somewhat higher than those reported by these other workers. Pulker (1984) gives a value for stress in Cr/glass films which ranges from 2300 MPa to about 1300 MPa at 100 nm. Klokholm and Berry (1968) give figures varying from about 1600 MPa down to 850 MPa at 100 nm. The figures obtained in this work are about 2000 MPa for a 100 nm Cr/glass film. These differences are probably a result of the deposition parameters, which are different for all three studies.

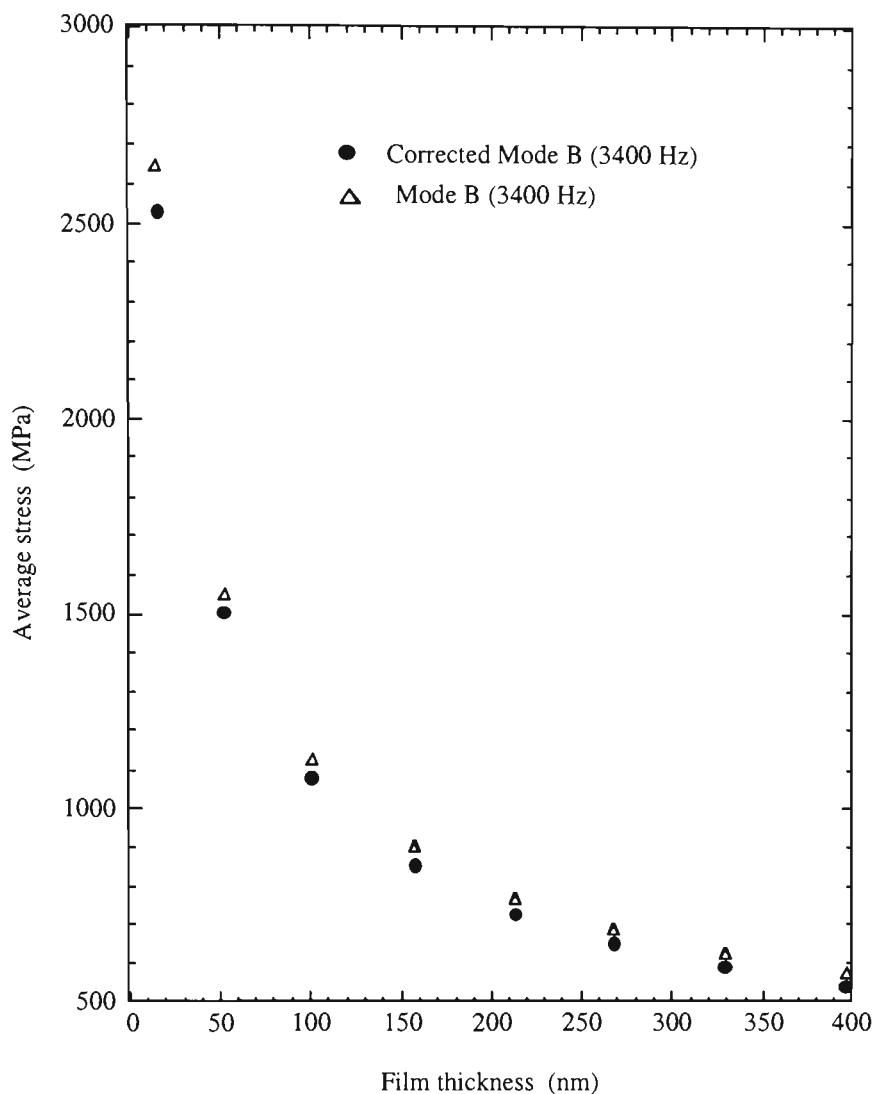


Figure 5.16 Stress as a function of film thickness for sequential deposition of an MgF_2 film at room temperature in the vacuum system. The lower points (full circles) have been corrected using $\psi^{1/2}$ factor.

Figure 5.18 shows the variation in stress in an MgF_2 film when exposed to the atmosphere while still inside the vacuum system. These measurements show a very rapid reduction in stress by about 40% in a few minutes followed by a slow approach to an equilibrium value over a period of 2 - 3 hours. This is in agreement with the data obtained by Pulker (1982) who observed that the stress in thin MgF_2 film is reduced between 40% and 100% due to water vapor absorption.

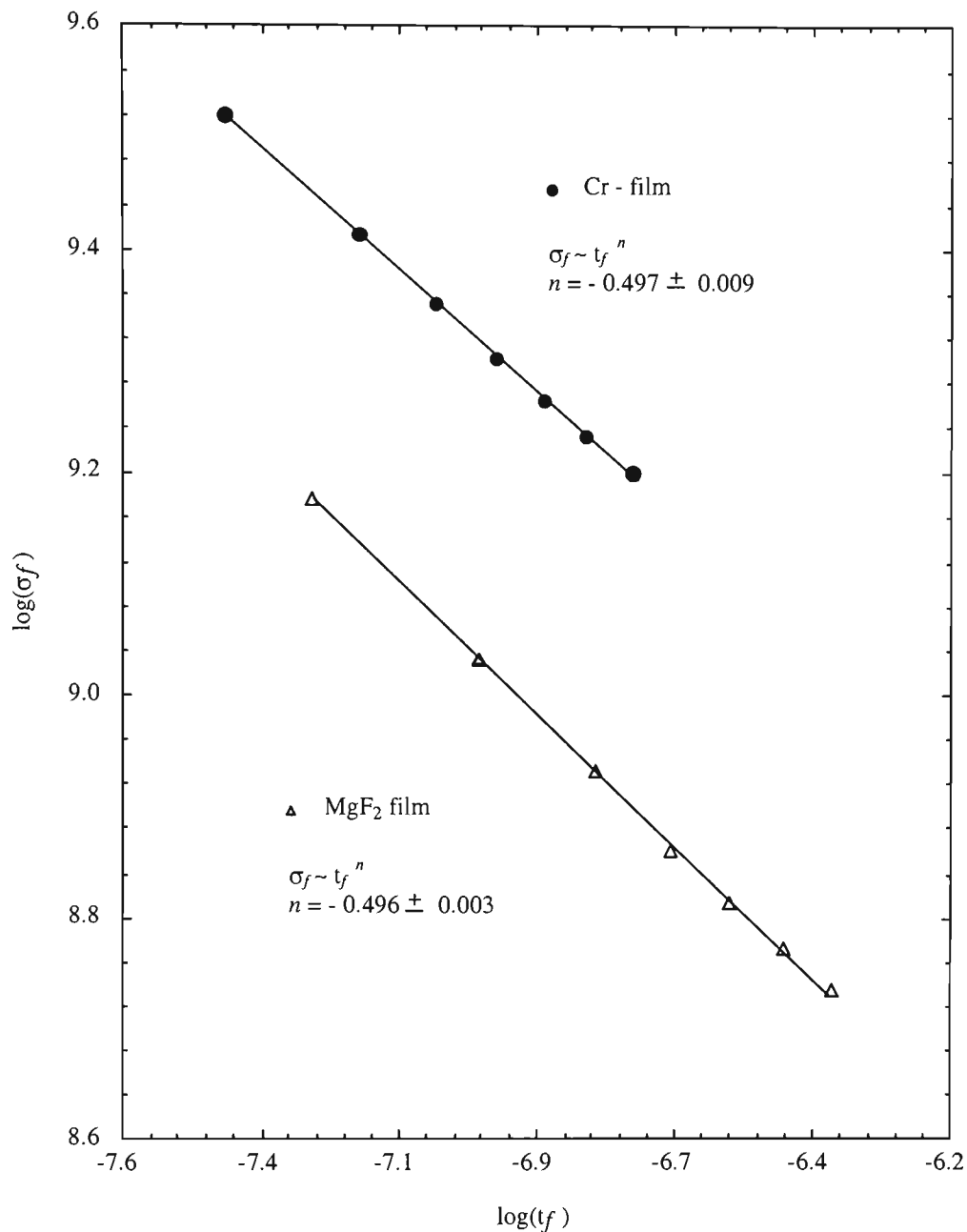


Figure 5.17 Variations of average stress with film thickness for sequential deposition of chromium and magnesium fluoride films in the vacuum system. The resonant frequency was corrected by factor $\psi^{1/2}$.

Also shown in figure 5.18 is a similar curve obtained after heating the previous film in vacuum for one hour at 150°C, then cooling back to ambient, followed by re-exposure to the atmosphere. Clearly non-reversible changes have occurred as a result of the initial heating and exposure to the atmosphere. Subsequently the film was reheated in vacuum and exposed to the atmosphere a third time. On this third occasion the variation of stress with exposure time closely followed the previous curve (second

exposure). Hence it appears that the structure of the film is not further affected by subsequent heating/cooling/exposure cycles after the first.

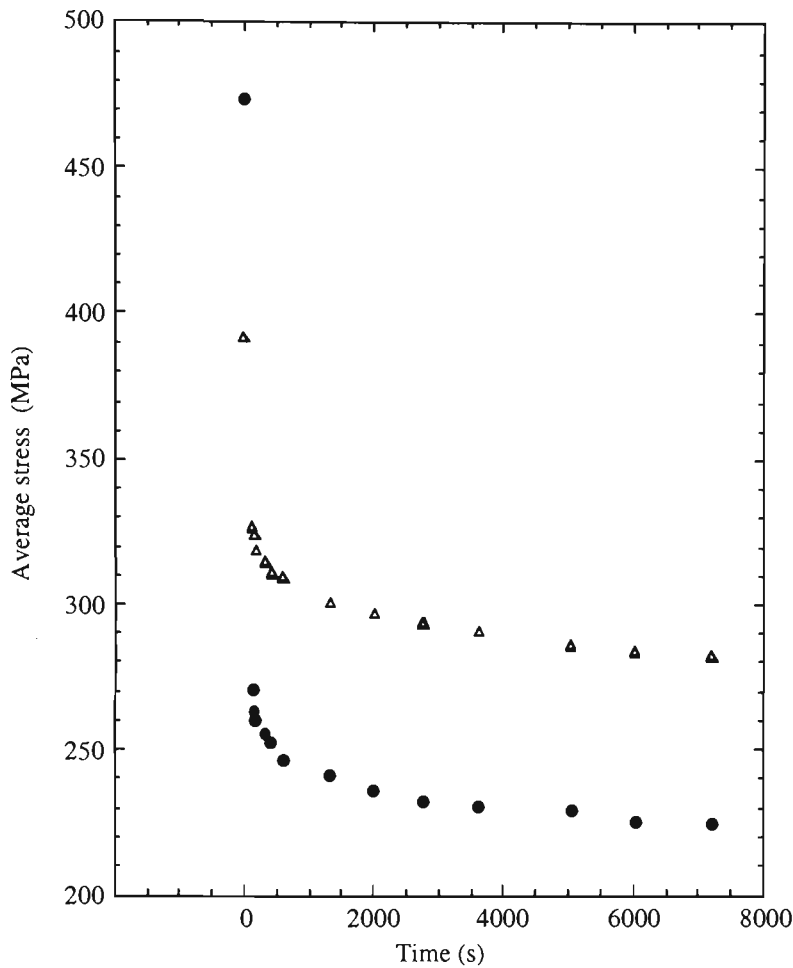


Figure 5.18 Stress variation produced by exposure of a 518 nm thick MgF_2 film to the atmosphere: ● - on exposure of a new film to the atmosphere; ▲ - on re-exposure of the previous film to the atmosphere after heating in vacuum at 150°C for 60 min.

5.6 Summary

In summary, a change in stress in a film deposited on a substrate gives rise to a change in curvature of the substrate. By using a thin glass test substrate, this curvature can be made relatively large and easy to measure. Curvature of the

substrate changes the characteristic resonant modal vibration frequencies. These modes can be excited thermoelastically using a low power laser diode and the modal frequencies measured remotely using a fibre optic interferometer. This method was initially tested using a chromium film consisting of a series of layers with the coated sample removed from the vacuum chamber for measurement after each layer. The chromium film in these atmosphere measurements was uniform over the substrate but non-homogeneous because of the presence of oxidation/contamination at the interface of intermediate layers. By deposition of an appropriate thickness of titanium film on the rear surface of the sample it was possible to measure the resonant frequency of the flat glass plate before coating the chromium film on the front side. Hence, the change in resonant frequency was determined more accurately than was possible by using the crude extrapolation to zero thickness used in the initial measurements. Finally, this technique was adapted for in situ measurements and experimental results for the chromium and magnesium fluoride films were presented. The effect of film thickness on resonant frequency changes was also considered and it was shown that this effect could be significant particularly for higher frequency resonant modes.

The results of this chapter have demonstrated that the combination of photo-thermoelastic vibration excitation and measurement of the modal frequency changes using a fibre interferometer, does represent a viable new technique which can be used for the measurement of stress in thin films. This measurement technique is broadly similar in difficulty of incorporation into a vacuum system to the current common technique of measurement of film thickness using a quartz crystal thickness

monitor. Hence it should be capable of finding significant applications when properly engineered instruments are commercially available.

Conclusion

6.1 Conclusion

The aim of this project was to develop an interferometric optical fibre sensing system which could measure the resonant vibrational frequencies of substrates coated with thin film materials and assess whether such modal frequency measurements could be used for the determination of stress in the films. The method developed used substrates in the form of thin circular disks which were supported by a rod fixed to the centre. Stress effects due to atomic mismatch between substrate and coating resulted in a curvature of the substrate/film structure which produced changes in the modal resonant frequencies. In order not to have the modal resonant frequencies affected by the excitation and measurement system, it was necessary to ensure that there was no mechanical contact between these systems and the vibrating structure. This was achieved by coupling the remote interferometric vibration detection system with remote photothermal excitation of the structure using a low power laser diode.

An actively-stabilised homodyne optical fibre interferometer was developed for this work. The interferometer was based on a 1523 nm He-Ne laser

and used a cylindrical PZT fibre stretcher in the reference arm for quadrature locking. Despite the losses associated with injection of the laser light into single mode fibre and the incorporation of an air path to the target surface, this interferometer achieved a NED of 0.16 nm in a 100 kHz bandwidth. When coupled with the photothermal excitation, this inteferometer allowed vibration frequency measurements to be made with excellent signal to noise ratios.

The differential equations for a flat uniform circular disk supported at its center were solved to obtain analytical expressions for the modal resonant frequencies. These solution were then extended to cover the case of a thin spherical shell – the shape of the structure after it begins to curve under stress. Finite element analysis was used to confirm the predictions of the analytical expressions. Expressions were also derived which related average film stress to the physical dimensions, elastic properties, and resonant frequencies of the flat and curved structures. To the knowledge of the author, these expressions are new and have not previously been reported in the literature.

Measurements were initially made using metallic (Cr) films. The variation of stress with thickness was determined by evaporating a series of Cr layers in a vacuum system and removing the structure after each deposited layer so that modal frequencies and curvature could be determined by measurements made in the atmosphere. These measurements suffered from difficulties associated with contamination of the layers while removed from the vacuum system. A further problem was encountered with the difficulty of determining the modal frequency before deposition when there was no coating to absorb the modulated LD excitation beam used to photothermally excite the vibrations. These problems were overcome by applying a very thin low-stress Ti layer to the rear surface of the substrate and by

modifying the system so that measurements could be made in situ during evaporation. Using this arrangement stress measurements were demonstrated for both metallic (Cr) and dielectric (MgF_2) films.

Substrate temperature rises during evaporation were shown to produce significant resonant frequency shifts, due principally to the temperature dependence of the elastic constants of the materials. These temperature effects represent a significant limitation to stress determination unless the temperature of the substrate remains constant during evaporation or else the substrate is allowed to cool back to ambient before modal frequency measurements are made. Measurements made in the vacuum system for both Cr and MgF_2 films showed that over the thickness ranges used, the average stress (and hence curvature) vary as the inverse square root of the film thickness. Changes in film stress on exposure to the atmosphere for MgF_2 films were demonstrated by admitting air to the vacuum system after deposition.

This work has added a new technique to ranges of techniques available for stress measurements in thin films. The experimental systems required for its implementation are reasonably simple and easily incorporated into a vacuum coating system. With feedback from interferometer to LD excitation, it was demonstrated that the system can be locked to resonance and the resonant frequency read directly from a frequency counter. While very accurate measurements of resonant frequencies are possible with the interferometer, in practice the accuracy of determination of stress changes are limited by the temperature variations of the structure during measurements. Absolute stress measurements are less accurate than measurements of changes in stress due principally to the difficulty in determination

of the resonant frequency of the flat glass plate prior to coating and the effect of dimensional-related frequency changes during coating.

6.2 Future work

The new stress measurement technique described in this thesis has been tested only with one metallic and one dielectric thin film deposited using resistive evaporation under vacuum conditions. For these films the thickness range covered was up to 400 nm. There is scope for further testing with a wider variety of single and multilayer films, deposition techniques and film thicknesses. For maximum benefit, such tests should be carried out under conditions where the optical technique can be compared to other established techniques such as curvature determination via interferometric displacement measurement.

In addition to basic studies such as those described above, it is a relatively simple matter to properly engineer an instrument which utilises feedback from interferometer to LD excitation to provide direct frequency readout. Such an instrument could be used in practical situations where existing techniques are proving difficult to apply or where their performance is less than fully satisfactory. One such situation would involve applications to the semiconductor industry to monitor stress during epitaxial growth or during metallisation coating applied to silicon or other substrates. For example, one large semiconductor company uses a process involving the deposition of Cr, Ni-V and Ag layers on thin silicon wafers for metallic contacts. Currently there is significant wastage during dicing and separation of these substrates as a result of stress-dependent curvature developed during

coating. The optical technique would be more compact, accurate and simple to apply than the existing optical lever stress monitor used in this process.

References

- Aberman, R. 1990, Measurements of the intrinsic stress in thin metal films, *Vacuum*, vol 41, no. 4-6, pp1279-1282.
- Bauer E and Popa H., 1984, *Thin Solid Films*, vol. 121, pp. 151.
- Beck U., Smith DT., Reiners G and Dapkunas SJ., 1998, Mechanical properties of SiO₂ and Si₃N₄ coatings, *Thin Solid Films*, vol. 332, no. 1-2, pp.164-171.
- Blackburn, H and Campbell, D.S. 1961, Stress in Evaporated Dielectric Films, in *Eight National Symposium on Vacuum Technology Transactions*, Pergamon Press, New York, pp. 943-946.
- Blevins, R.D. 1979, in *Formulas for Natural Frequency and Mode Shape*, eds Van Nostrand Reinhold Company, New York, pp. 291-334.
- Brenner, A and Senderoff, S., 1949, Calculation of stress in electrodeposits from the curvature of a plated strip, *J. Res. Nat. Bur. Stand.*, vol.42, pp. 105.
- Bromley, E.I., Randall, J.N., Flanders, D.C and Mountain, R.W. 1983, A technique for the determination of stress in thin films, *The Journal of Vacuum Science and Technology*, vol. B1, no. 4, pp. 1364-1366.
- Campbell, D. S. 1963, Stress in Thin Dielectric Films, *Electronics Reliability and Microminiaturization*, vol. 2, pp. 207-213.

- Cardinale GF., Howitt DG., Clift WM., Mccarty KF., Medlin DL., Mirkarimi PB and Moody NR., 1996, Micromachined silicon cantilever beams for thin-film stress measurement, *Thin Solid Films*, vol. 287, no. 1-2, pp. 214-219.
- Charpentier, P., Lepoutre, F and Bertrand, L. 1982, Photoacoustic measurements of thermal diffusivity description of the "drum effect", *Journal of Applied Physics*, vol. 53, no. 1, pp. 608-614.
- Cornella G., Lee SH., Nix WD and Bravman JC., 1997, An analysis technique for extraction of thin film stresses from x-ray data, *Applied Physics Letters*, pp. 71, no. 20, pp. 2949-2951.
- Crosbie, R.A., Dewhurst, R.J and Palmer, S.B. 1986, Flexural resonance measurements of clamped and partially clamped disks excited by nanosecond laser pulses, *Journal of Applied Physics*, vol. 59, no. 6, pp. 1843-1848.
- Davidenkov, N.N. 1961, Measurement of residual stresses in electrolytic deposits, *Sov. Phys.-Solid State*, vol. 2, pp. 2595.
- Digonet, M. J. F and Kim, B. Y. 1988, in *Fibre optic components*, eds John Dakin and Brian Culshaw, Artech House: London, vol. 2, pp 209-248.
- Egelhoff W. F. Jr and Jacob I., 1989, *Physics Review Letters*, vol. 62, pp. 921.
- Ennos, A.E. 1966, Stress Developed in optical Film Coatings, *Applied Optics*, vol. 5, no. 1, pp. 51-61.
- Ferguson, I. 1989, *Auger Microprobe Analysis*, eds Adam Hilger, Bristol and New York.
- Finegan, J.D and Hoffman, R.W. 1959, Stress Anisotropy in Evaporated Iron Films, *Journal of Applied Physics*, vol. 30, pp. 597-598.

- Finegan, J.D and Hoffman, R.W. 1961, Stress and Stress Anisotropy in Iron Films, in *Transaction of the Eight Vacuum Symposium and Second International Congress*, Pergamon Press, New York, pp. 935-942.
- Flinn, P.A. 1989, Principles and applications of wafer curvature techniques for stress measurements in thin films, *Materials Research Symposium Proceeding*, vol. 130, pp. 41-51.
- Flinn, P.A., Gardner, D.S and Nix, W.D. 1987, Measurement and Interpretation of Stress in Aluminium-Based Metallisation as a Function of Thermal History, *IEEE Transactions on Electron devices*, vol. ED-34, no. 3, pp. 689-698.
- Gibson, J.E. 1980, in *Thin Shells*, eds Pergamon Press: Oxford.
- Gilmore C and Sprague J. A., 1991, *Physics Review B*, vol. 44, pp. 8950.
- Glang, R., Holmwood, R.A and Rosenfeld, R.L. 1965, Determination of Stress in Films on Single Crystalline Silicon Substrates, *The Review of Scientific Instruments*, vol. 36, no. 1, pp. 7-10.
- Glass, J.A and Guenter, A.H. 1978, Laser induced damage in optical materials: Ninth ASTM symposium, *Applied Optics*, vol. 17, no. 15, pp. 2386-2411.
- Halliday, J.S., Rymer, T.B and Wright, K.H.R. 1954, An electron-diffraction examination of thin films of lithium fluoride and copper prepared by vacuum evaporation, *Proceedings of the Royal Society (London)*, vol. A225, pp. 548-563.
- Hariharan, P. 1994, *Basics of Interferometry*, eds McGraw-Hill, New York.

- Harper, B. D and Wu, C. P. 1990, A geometrically nonlinear model for predicting the intrinsic film stress by the bending-plate method, *International Journal of Solids Structures*, vol. 26, no. 5/6, pp. 511-525.
- Hoffman, R.W and Story, H.S. 1954, Stress Annealing in Copper Films, *Journal of Applied Physics*, vol. 24, pp. 193.
- Hoffman, R.W. 1966, The Mechanical Properties of Thin Condensed Films, in *Physics of Thin Films*, eds Hass G. and Thun R.E., Academic Press, New York, vol. 3, pp. 211-273.
- Honda N., Shoji F., Kidoguchi S., Hamada Y., Nagata M and Oura K., 1997, In situ stress measurements of sputter-deposited films, *Sensors & Actuators A-Physical*, vol. 62, no. 1-3, pp. 663-667.
- Hopmann, W.H. 1961, Frequencies of Vibration of Shallow Spherical Shells, *Journal of Applied Mechanics*, vol. 28, pp. 305-307.
- Hornauer, H., Patricos, J and Röhl, K. 1990, Sensor head for measurement of stress anisotropy in thin films, *Vacuum*, vol. 41, no. 4-6, pp. 1302-1304.
- Jackson, D. A., Priest, Dandridge, A and Tveten, A. B. 1980, Elimination of drift in a single-mode optical fibre interferometer using a piezoelectricity stretched coiled fibre, *Applied Optics*, vol. 19, no. 17, pp. 2926-2929.
- Kaye, G. W.C and Laby, T. H., 1973, in *Tables of physical and chemical constants*, eds Longman, pp. 33.
- Kern, W and Poutinen, D.A. 1970, Cleaning Solutions Based on Hydrogen Peroxide for use in Silicon Semiconductor Technology, *RCA Review*, vol. 6, pp. 187-206.

- Kinbara, A. 1961, Internal Stress in Gold Evaporated Thin Films, *Oyo Butsury*, vol. 30, pp. 441-445.
- Kittel, C. 1976, in *Introduction to solid state physics*, eds New York : Wiley.
- Klokholm, E and Berry, B.S. 1968, Intrinsic Stress in Evaporated Metal Films, *Journal of the Electrochemical Society*, vol. 115, no. 8, pp. 823-826.
- Klokholm, E. 1969, An apparatus for measuring stress in thin films, *The Review of Scientific Instruments*, vol. 40, no. 8, pp.1054-1058.
- Koch, R. 1994, The intrinsic stress of polycrystalline and epitaxial thin metal films, *Condensed Material*, vol.6, pp.9519-9550.
- Kylner C and Mattsson L., 1997, An optical instrument for overall stress and local stress relaxation analysis in thin metal, *Review of Scientific Instruments*, vol. 68, no. 1, Part 1, pp. 143-149.
- Leusink, G.J., Oosterlaken, G.C., Janssen, G.C.A.M and Radelaar, S. 1992, *In situ* sensitive measurement of stress in thin films, *The Review of Scientific Instruments*, vol. 63, no. 5, pp. 3143-3146.
- Luedtke W. D and Landman U., 1991, *Physics Review Letters*, vol. 44, pp. 5970.
- MacDonald, J.R. 1957, Stress in Evaporated Ferromagnetic Films, *Physical Review*, vol. 106, pp. 890-98.
- Macleod, H.A and Richmond, D. 1976, Moisture penetration patterns in thin films, *Thin Solid Films*, vol. 37, pp. 163-169.
- Maden, M.A., Jagota, A., Mazur, S and Farris, R.J. 1994, Vibrational Technique for Stress measurement in Films: I, Ideal Membrane Behaviour, *Journal of American Ceramic Society*, vol. 77, no. 3, pp. 625-635.

- Maissel, L.I and Glang, R. 1970, *Handbook of Thin Film Technology*, Chapter 12, (McGraw-Hill, New York).
- Malecki, I. 1969, *Physical foundations of technical acoustics*, (Oxford, New York, Pergamon Press).
- Malhotra SG., Rek ZU., Yalisove SM and Bilello JC., 1997, Analysis of thin film stress measurement techniques, *Thin Solid Films*, vol. 301, no. 1-2, pp. 45-54.
- Martin A., Osullivan P and Mathewson, 1998, Dielectric reliability measurements methods - A Review, *Microelectronics & Reliability*, vol. 38, no.1, pp. 37-72.
- Martiny, G. 1987, Analysis of a single mode optical fibre piezoceramic phase modulator, *Optical and Quantum Electronics*, vol. 19, pp. 179-190.
- Masters, C. B and Salamon, N. J. 1993, Geometrically nonlinear stress-deflection relations for thin film/substrate system, *International Journal of Engineering Science*, vol. 31, no. 6, pp. 915-925.
- McLachlan, N.W. 1951, in *Theory of vibrations*, eds Publications, Inc., New York, pp. 72-144.
- Morse, P.M and Ingard, K.U. 1968, in *Theoretical Acoustics*, eds New York: McGraw-Hill Book Company.
- Murbach, H.P and Wilman, H. 1953, The origin of Stress in Metal Layers Condensed from the Vapour in High Vacuum, *Proceedings of Physical Society (London)*, vol. B66, pp. 905-910.
- Neddermeyer H., 1990, *Critical Review of Solid State Materials of Science*, vol. 16, pp. 309.

- Neugebauer, C.A. 1964, Structure Disorder Phenomena in Thin Metal Films, in *Physics of Thin Films*, eds Hass G. and Thun R.E., Academic Press, New York, vol. 2, pp. 1-66.
- Neugebauer, C.A. 1959, The saturation magnetization of nickel films of thickness less than 100 in *Structure and Properties of Thin Films*, eds Neugebauer, C.A., Newkirk, J.W and Vermilyea, D.A., Wiley, New York, pp. 358-369.
- Nie, A.G. 1980, A method for the determination of the stress in, and Young's Modulus of Silicon Nitride Passivation Layers, *Solid State Technology*, vol. 23, pp. 81-84.
- Novice, M. A. 1962, Effect of atmospheric exposure on stress in evaporated silicon monoxide films, *British Journal of Applied Physics*, vol. 13, pp. 561-563.
- Nowacki, W. 1963, in *Dynamics of elastic systems*, eds Chapman & Hall Ltd. - London, pp. 260-270.
- Noyan IC., Huang TC and York BR., 1995, Residual stress strain analysis in thin films by x-ray diffraction (Review), *Critical Reviews in Solid State & Materials Sciences*, vol. 20, no. 2, pp. 125-177.
- Ohki, M, Shima, N and Shiosaki, T. 1992, Optical measurements of piezoelectric vibration in circular rod and disk ceramics, *Japanese Journal of Applied Physics*, vol. 11, pp. 3272-3275.
- Ohring, M. 1992, *The Materials Science of Thin Films*, eds San Diego, Academic Press, Inc..
- Opsal, J and Rosencwaig, A. 1982, Thermal-wave depth profiling: Theory, *Journal of Applied Physics*, vol. 53, no. 6, pp. 4240-4246.

- Pashley D. W and Stowell M. J., 1966, *Journal of Vacuum Technology*, vol. 3, pp. 156.
- Philp, W.R and Booth, D.J. 1994, Remote excitation and sensing of mechanical resonances in structures using laser diodes and an optical fibre interferometer *Measurement Science and Technology*, vol. 5, pp. 731-735.
- Pilkey, J. 1994, in *Formulas for stress, strain, and structural matrices*, eds New York: J. Wiley, pp.87-108.
- Prescott, J. 1961, in *Applied Elasticity*, eds New York: Dower, pp. 565-597.
- Priest, J.R and Caswell, H.L. 1961, Residual Stress in Silicon Monoxide Films, in *Transaction of the Eight Vacuum Symposium and Second International Congress*, eds Pergamon Press, New York, pp. 947-949.
- Pulker, H.K. 1982, Mechanical properties of optical films, *Thin solid films*, vol. 89, pp. 191-204).
- Pulker, H.K. 1984, in *Coatings on glass*, eds Amsterdam ; New York: Elsevier, pp 311-353.
- Reissner, E. 1946, On Vibrations of Shallow Spherical Shells, *Journal of Applied Physics*, vol. 17, pp. 1038-1342.
- Rosakis A.J., Singh R.P., Tsuji Y., Kolawa E and Moore N.R., 1998, Full field measurements of curvature using coherent gradient sensing - application to thin film characterization, *Thin Solid Films*, vol. 325, no.1-2, pp. 42-54.

- Sahu, P., Scarminio, J and Decker, F. 1990, A laser beam deflection system for measuring stress variations in thin film electrodes, *Journal of the Electrochemical Society*, vol. 137, no. 4, pp. 1150-1154.
- Scardi P., Polonioli P and Ferrari S., 1994, Residual stress in stabilized zirconia thin films prepared by rf magnetron sputtering, *Thin Solid Films*, vol. 253, no. 1-2, pp. 349-355.
- Schneider C. M., Bressler P., Schuster P., Kirschner J., de Miguel J. J and Miranda R., 1990,. *Physics Review Letters*, vol. 64, pp. 1059.
- Scruby, C. B and Drain, L. E. 1990, in *Laser Ultrasonic: Techniques and Applications*, eds Adam Hilger, Bristol.
- Shouyao, S and Jiu-Lin, Z. 1992, A fibre-optic sensor for the measurement of stress in optical coatings, *International Journal of Optoelectronics*, vol. 7, no. 1, pp. 129-132.
- Sinha, A.K., Levinstein, H.J and Smith, T.E. 1978, Thermal stresses and cracking resistance of dielectric films (SiN, Si₃N₄, and SiO₂), *Journal of Applied Physics*, vol. 49, no. 4, pp. 2423-2426.
- Soedel, W. 1973, A Natural Frequencies Analogy between Spherically Curved Panels and Flat Plates, *Journal of Sound and Vibrations*, vol. 29, no. 4, pp. 457-461.
- Stoney, G.G. 1909, The tension of Metallic Films deposited by Electrolysis, *Proceeding of the Royal Society London*, vol. A82, pp. 172-175.
- Story, H.S and Hoffman, R.W. 1957, Stress Annealing in Vacuum Deposited Copper Films, *Proceedings of Physical Society (London)*, vol. 70, pp. 950-960.

- Tanaka K., Akiniwa Y., Inoue K and Ohta H., 1998, X-ray measurement of residual stress in patterned aluminum thin films sputtered on silicon wafers, *JSME International Journal Series A-Solid Mechanics & Material Engineering*, vol. 41, no. 2, pp. 290-296.
- Thun, R.E. 1964, Structure of Thin Films, *Physics of Thin Films*, eds Hass G. and Thun R.E., Academic Press, New York, vol. 1, pp. 187-232.
- Turner, G and Aberman, R. 1990, On the mechanical properties of UHV-deposited Cr films and their dependence on substrate temperature, oxygen pressure and substrate material, *Vacuum*, vol. 41, no. 4-6, pp. 1300-1301.
- Timoshenko, S., Young, D.H. 1966, *Vibration Problems in Engineering*, D. Van Nostrand Company, Inc., New York.
- Timoshenko, S.P and Woinowsky-Krieger, S. 1959, *Theory of Plates and Shells*, eds McGraw Hill, New York.
- Tolansky, S. 1948, *Multiple beam Interferometry*, Oxford, Clarendon.
- Uchida H., Kiguchi T., Saiki A., Wakiya N., Ishizawa N., Shinozaki K and Mizutani N. 1999, Measurement technique for the evaluation of residual stress in epitaxial thin film by asymmetric X-ray diffraction, *Nippon Seramikkusu Kyokai Gakujutsu Ronbunshi-Journal of the Ceramic Society of Japan*, vol. 107, no. 7, pp. 606-610.
- Udd, E, 1991, *Fibre optic sensors: An introduction for engineers and scientists*, Jhon Wiley & Sons, Inc.
- Vandamme LKJ and Vankemenade AJ., 1997, Resistance noise measurement - a better diagnostic tool to detect stress and current induced degradation, *Microelectronics & Reliability*, vol. 37, no. 1, pp. 87-93.

- Vandrienuizen BP., Goosen JFL., French PJ and Wolffenbuttel RF., 1993, Comparison of techniques for measuring both compressive and tensile stress in thin films, *Sensors & Actuators A-Physical*, vol. 37-8, pp. 756-765.
- Veneables.J. A., Derrien J and Janssen A. P., 1980, *Surface Science*, vol. 95, pp. 411.
- Vinci RP and Vlassak JJ., 1996, Mechanical behavior of thin films (Review) *Annual Review of Materials Science*, vol. 26, pp. 431-462.
- Vreeland, Jr.T., Dommann, A., Tsai, C.J and Nicolet, M.A. 1989, X-Ray Diffraction Determination of Stress in Thin Films, *Materials Research Society Symposium Proceedings*, vol. 130, pp. 3-12.
- Walsh, D and Culshaw, B. 1991, Optically activated silicon microresonator transducers: an Assessment of Material Properties, *Sensors and Actuators A*, vol. 25-27, pp. 711-716.
- Watson, G.N. 1944, in *The Theory of Bessel functions*, eds Cambridge: Cambridge University Press.
- Winau, D., Koch, R and Rieder, K.H. 1992, Growth mode related intrinsic stress of thin nickel and iron films under the influence of oxygen, *Vacuum*, vol. 43, no. 5-7, pp. 525-527.
- Windischmann H and Gray KJ., 1995, Stress measurement of cvd diamond films, *Diamond & Related Materials*, vol. 4, no. 5-6, pp. 837-842.

Appendices

- A.1 Technical data for the glass substrate used in experiments
- A.2 Spectrographic analysis of the evaporants according to the manufacturer specification.
- A.3 List of figures
- A.4 List of tables
- A.5 List of symbols used in this thesis

A.1 Technical data for the glass substrate used in experiments

MENZEL glass substrates are in the visible spectral area free of absorption, optically clean and free of smears, streaks as well as other material defects. *MENZEL* cover slips meet strict standards concerning flatness and thickness-variation, e.g. this guarantees microtome sections are evenly covered.

MENZEL cover slips are resistant to water (hydraulic class 1) and fulfill all known standard requirements, particularly German Industrial Standard 12111. Specimens covered with *MENZEL* glass can be stored for long time periods for examinations or documentation.

MENZEL cover slips contain neither lead, cadmium or thallium compounds nor arsenic-oxide. If stimulated within the near UV-range, i.e. at $\lambda = 365$ nm (Hg) as in fluorescent microscopy, *MENZEL* cover glass does not show any fluorescence.

The average coefficients of thermal-expansion are: $(73-74) \times 10^{-7} \text{ K}^{-1}$ in the temperature range of $(20 - 300)^\circ\text{C}$.

The refractive indices are: $n = 1.5249$ for $\lambda = 546.1 \text{ nm}$

Density: $(2.51 \pm 0.1) \text{ kg/dm}^3$

Softening point: 732°C or 736°C .

A.2 Spectrographic analysis of the evaporants according to the manufacturer specification.

Chromium metal, pieces 3-6 mm, 99.99 % pure

Manufacturer: *CERAC Incorporated*

Element	Concentration (ppm)
Ca	<10
Fe	<3
Mg	<10
Si	<10

Magnesium fluoride, pieces 3-6 mm, 99.9 % pure

Manufacturer: *SIGMA ALDRICH PTY. LTD.*

Element	Concentration (ppm)
Ca	1500
Na	50
Mn	11
Fe	10
K	6
Sr	5
S	4
Si	4
Al	3
Cr	2
P	2
Cu	1
All others	<1

Titanium metal

Manufacturer: *PURE TECH Inc.*

Element	Concentration (ppm)
Ca	28
Na	3
Fe	390
K	1
Mo	5
S	150
Si	10.5
Al	141
Cr	78
P	1
Cu	5

Titanium plate with diameter of 50 mm, thickness of 3 mm and purity of 99.99 % was used for magnetron sputtering system.

A.3 List of figures

Chapter 2

- Figure 2.1** (a) Residual tensile stress in a thin film. (b) Residual compressive stress in a thin film. F_i are stress-induced forces and M is induced bending moment. 2-10

Chapter 3

- Figure 3.1** Representation of the first 3 natural modes of vibration of a circular plate clamped at the center. The frequencies of vibration do not form a harmonic series. 3-13
- Figure 3.2** Representation of the 4th, 5th and 6th natural modes of vibration of a circular plate clamped at the center. 3-14
- Figure 3.3** Representation of the 7th, 8th and 9th natural modes of vibration of a circular plate clamped at the center. 3-15
- Figure 3.4** The sample used to measure the frequency of flat plate. 3-16
- Figure 3.5** Isometric view of the FEM meshing of the plate and shells. 3-21
- Figure 3.6** Variation of resonant frequencies for modes of about 2.3 kHz, 3.4 kHz and 4.7 kHz with inverse radius of curvature by FEM (open points) and theoretical calculations using equation 3.48 (solid points). 3-23
- Figure 3.7** Stress components in a solid. 3-25
- Figure 3.8** Internal forces and stresses in a solid. 3-26
- Figure 3.9** (a) Tensile force applied to a plate. (b) Distortion in a plate due to applied shear stress. 3-28
- Figure 3.10** Stress analysis of film-substrate structure: (a) composite structure; (b) elastic bending of structure under applied end moment; (c) an element of cross section of substrate/film structure. 3-34

Chapter 4

Figure 4.1.	High vacuum system. (1) Bell-jar; (2)High-vacuum gage; (3) Diffusion pump;(4) Mechanical pump; (5) Roughing valve; (6) High-vacuum isolation valve; (7) Backing valve; (8) Exhaust line; (9) Gauge; (10) Fore-line; (11) Baffle; (12) Evaporation boat; (13) High current leads; (14) Thickness sensor; (15, 16) Stationary aluminium plate; (17) Slot; (18) Sample holder; (19) Rotating plate; (20) Base plate; (21) Vacuum release valve; (22) Glass substrate; (23) Rotation shaft.	4-4
Figure 4.2.	Aluminium rotation substrate holder. The slot (17) is to allow deposition on the crystal monitor.	4-6
Figure 4.3.	The substrate used in experiments.	4-8
Figure 4.4.	The jig used to glue the metal rod to the centre of the substrate.	4-9
Figure 4.5.	The holder used to hold the sample during deposition of thin film and measurement.	4-11
Figure 4.6.	Schematic diagram of optical lever method used to measure the radius of the curved sample.	4-12
Figure 4.7.	a) Angstromer-scope interferogram. ΔL is fringe spacing and L is fringe offset. b) Schematic of optical apparatus for the measurement of the thickness of thin film from multiple-beam Fizeau fringes. An opaque Ag film is deposited over a step in thin film.	4-15
Figure 4.8.	Calibration curve for the quartz crystal thickness monitor.	4-17
Figure 4.9.	Schematic diagram of the experimental set-up used to excite and detect vibration in glass wafer coated with a thin film.	4-18
Figure 4.10.	Schematic diagram of the fibre interferometer used to monitor surface displacements in the wafer.	4-20
Figure 4.11.	Interferometer output.	4-24
Figure 4.12.	Interferometer output for $V < 1$	4-24
Figure 4.13.	Small - signal sensitivity versus phase difference between the two arms of the interferometer.	4-26

Figure 4.14.	Signal fading problem in fibre interferometer.	4-26
Figure 4.15.	Experimental set-up in more details.	4-29
Figure 4.16.	Electronics circuit to detect optical signal from interferometer and to drive PZT.	4-33
Figure 4.17.	Schematic diagram of evaporation plant with experimental setup for in situ measurement of stress in thin films; (1) Glass substrate. (2) Head of film thickness sensor; (3) Shutter.	4-38
Figure 4.18.	Typical output of the interferometer when the resonance at about 3400 Hz was excited. During these measurements all pumps were running.	4-39

Chapter 5

Figure 5.1	The Auger nanoprobe depth-profiles for chromium, oxygen and carbon. The independently measure film thickness is displayed on the diagram. (a) Atomic concentration of Cr, (b) atomic concentration of carbon and oxygen impurities.	5-5
Figure 5.2	Variation of radius of substrate/film curvature with total deposited film thickness for a chromium film. The measurements were made in the atmosphere. The radius of the curvature was measured using lever method.	5-9
Figure 5.3	Measured variation of resonant frequency shift with the inverse radius of curvature measured using lever method for some different vibrational modes. The data was obtained after each deposited chromium film layer was exposed to the atmosphere. The lines are a guide to the eye.	5-10
Figure 5.4	The resonant frequency shift versus the product of thickness and stress determined via equation 3.66 for successive deposition of the chromium film measured in the atmosphere.	5-11
Figure 5.5	Stress as a function of film thickness for Cr films deposited on a glass substrate. The stress has been determined from the curvature of the glass plate using equation 3.66 and is measured in the atmosphere.	5-12
Figure 5.6	Variation of radius of substrate curvature, measured using lever method, with Cr film thickness. The measurements were made	

	by removing the sample from the vacuum system after each successive layer of Cr was deposited. Samples were coated with an initial 20 nm layer of Ti in order to measure the resonant frequency before Cr deposition.	5-15
Figure 5.7	Typical measured variation of resonant frequency shift with the inverse radius of substrate curvature (obtained using the lever method) for some vibrational modes of the samples coated with titanium on the rear surface. The measurements were taken in the atmosphere after deposition of each chromium layer. The lines are merely a guide to the eye.	5-16
Figure 5.8	Stress as a function of film thickness for Cr films coated on a glass substrate with titanium film on the rear surface. The measurements were made in the atmosphere.	5-17
Figure 5.9	Resonant frequency shift versus the product of thickness and stress determined via Equation 3.66 for a sample coated with titanium on the rear surface. The measurements were made for chromium films in the atmosphere.	5-18
Figure 5.10	<i>In situ</i> measured variation of resonant frequency shift of the glass sample coated with titanium on rear surface versus temperature. The temperature measurements were made using a thermocouple near front substrate surface.	5-21
Figure 5.11	Measured variation of resonant frequency shift with film thickness during the deposition of chromium. Under these conditions temperature changes also occur.	5-23
Figure 5.12	<i>In situ</i> measured variation of resonant frequency shift during the deposition of MgF ₂ . Under these conditions temperature changes also occur.	5-24
Figure 5.13	<i>In situ</i> measured variation of resonant frequency shift with film thickness of chromium for sequential deposition of layers. The substrate was allowed to cool back to room temperature before resonant frequency measurements are made. The lower line for each mode shows the frequency shift after correction by factor $\psi^{1/2}$	5-27
Figure 5.14	<i>In situ</i> measured variation of resonant frequency shift with film thickness of magnesium fluoride for sequential deposition (constant temperature for measurement The lower line for each mode shows the frequency shift after being correction by factor $\psi^{1/2}$	5-28

Figure 5.15	Stress as a function of film thickness for sequential deposition of Cr film at room temperature in the vacuum system. The lower points (full circles) have been corrected using the factor $\psi^{1/2}$	5-30
Figure 5.16	Stress as a function of film thickness for sequential deposition of MgF ₂ film at room temperature in the vacuum system. The lower points (full circles) have been corrected using $\psi^{1/2}$ factor.	5-31
Figure 5.17	Variations of average stress with film thickness for sequential deposition of chromium and magnesium fluoride films in the vacuum system. The resonant frequency was corrected by factor $\psi^{1/2}$	5-32
Figure 5.18	Stress variation produced by exposure of 518 nm thick MgF ₂ film to the atmosphere: • - on exposure a new film to the atmosphere; Δ - on re-exposure of the previous film to the atmosphere after heating in vacuum at 150 °C for 60 min.	5-33

A.4 List of Tables

Chapter 2

Table 2.1	Sensitivity of stress-measuring techniques after Hoffman (1966) and Koch (1994)..	2.22
------------------	---	------

Chapter 3

Table 3.1	Calculated value for natural resonant frequency for flat circular glass plate clamped in the center.	3-16
Table 3.2	The measured resonant frequencies of a flat circular glass plate in air and in vacuum (10^5 Pa).	3-17
Table 3.3	Comparison between calculated and measured resonant frequencies of a flat circular glass plate in vacuum (10^5 Pa)).	3-17
Table 3.4	Comparison of calculated resonant frequencies, using equation 3.40, for a flat glass plate and data obtained using FEM.	3-18
Table 3.5	Comparison of experimental results of resonant frequencies for a flat glass, obtained in vacuum of 10^5 pa, for a flat glass plate and data obtained using FEM.	3-19
Table 3.6	Comparison of calculated resonant frequencies, using equation 3.48 for a curved glass plate, clamped in the center, and data obtained using FEM. The frequency shifts shown are the differences in frequency between the curved and flat plates. The resonant frequency of flat glass was obtained using FEM method.	3-22
Table 3.7	Calculated factor Ψ using equation 3.91 for film thicknesses up to 200 nm for chromium and 400 nm for magnesium fluoride.	3-42

Chapter 4

Table 4.1 A summary of characteristics and performance of the active homodyne interferometer used to measure the changes of resonant frequencies which are related to the changes in the stress developed in thin films.	4-35
--	------

Chapter 5

Table 5.1 Measured resonant frequencies of the first 8 vibration modes (f_n) as a function of film thickness (t_f). The frequency shifts from the uncoated values (Δf_n) are also given as are the measured radius of curvature (lever method) and the calculated average stress (σ). This data was obtained by removing the sample from the vacuum chamber after each coating layer and making the measurements in air.	5-8
Table 5.2 Measured and corrected resonant frequency shift for Cr thin film for three different resonant modes.	5-26
Table 5.3 Measured and corrected resonant frequency shift for MgF ₂ thin film for three different resonant modes.	5-26

A.5 List of symbols used in this Thesis

Chapter 2

Φ_f	free surface energy
$\Delta\mu$	chemical potential
k	Boltzmann's constant
T	substrate temperature
v	the volume of a single film atom
P	vapour pressures of the nuclei
P_∞	vapour pressures of the bulk phase
Φ^*	specific free interface energy
β	free energy of adhesion
F	stress-induced force
M	stress-induced bending moment
σ_{tot}	total stress
$\sigma_{therm.}$	thermal stress
$\sigma_{intr.}$	intrinsic (residual) stress
T_1, T_2	temperature before and after deposition of a film
E_f, E_s	Young's modulus of elasticity for the thin film and substrate
ν_f, ν_s	Poisson's ratio for the thin film and substrate
α_s, α_f	coefficient of thermal expansion of the film and the substrate

σ_f	stress in the thin film
δ	deflection of the cantilever beam substrate
l	length of the cantilever beam
a	radius of the membrane and the plate
t_s, t_f	thickness of the substrate and the film
$J_m(x)$	Bessel function of order m
μ_{mn}	n -th root of $J_m(x)$
R	radius of the substrate/film composite
L	distance travelled by reflected beam; fibre length
Δx	distance from the point where the beam hits the sample to the centre of the sample
Δd	resulting translation of the reflected beam on the screen
R_0	radius of the substrate before deposition of the film
R	radius of the substrate after deposition of the film
a_0, a	lattice constant of the unstressed bulk material and the film
$f_{mn(s)}, f_{mn(p)}$	natural frequencies of the mn mode of the shell and the plate
ρ	density of the material

Chapter 3

η	normal surface displacement
M_1, M_2	bending moments
F	shear force per unit length

h	half-thickness of the plate
a	radius of flat plate
r	radial distance from center of plate
J_m	Bessel function of order m
f_{mn}	frequency of vibration
mn	frequency mode (m -number of diametrical nodal lines; n -number of circular nodes)
$\Gamma(m+1)$	gamma function of $(m+1)$
Z_m	Neumann's form of the m th order Bessel function of the second kind
γ	Euler's constant
ΔA	area element
$\sigma_x, \sigma_y, \sigma_z$	normal stress
$\tau_{xy}, \tau_{yx}, \tau_{zy}, \tau_{yz}, \tau_{zx}, \tau_{xz}$	shear stresses.
V_y, V_z	shear forces
$\epsilon_x, \epsilon_y, \epsilon_z$	strains
$\gamma_{yx}, \gamma_{xz}, \gamma_{yz}$	shear strains
G	shear modulus (change of shape)
K	bulk modulus
z	distance from the neutral axis

Chapter 4

L	distance from sample to screen
$\Delta\phi$	differential phase shift
ϕ_s, ϕ_r	the phase retardance of the signal and reference arms
E_1	amplitude of the optical field in signal arm of the interferometer
E_2	amplitude of the optical field in the reference arm of the interferometer
E_0	amplitude of the optical source field
$k_{i(t \text{ or } c)}$	coupler amplitude coefficient for i^{th} directional coupler (subscript t denotes the transmitted beam in the coupler and c is the coupled beam)
α_s, α_r	losses in signal and reference arms of the interferometer
τ_s, τ_r	propagation times from the source to the detectors via the signal and reference arms
I_1, I_2	intensity of the complementary outputs of the interferometer
I_0	optical source intensity
$\langle \dots \rangle$	time average
γ	degree of coherence of the laser
$s(t)$	output signal from the interferometer
$A(t)$	phase shift induced by the piezoelectric phase shifter
ϕ_{nr}, ϕ_{ns}	noise generated phase shifts in reference and signal arm
n	refractive index
Δn	variations of the refractive index
Δl	variations of the fibre length
λ	wavelength of laser beam in the vacuum

d_{PZT}	piezoelectric coefficient
V	applied voltage
N	number of turns of the fibre
Δn	variation of refractive index when the fibre is stretched
V_0	amplitude of the interference
V_{DC}	DC bias of PZMS
η	displacement
η_N	noise equivalent displacement
$\langle V_N^2 \rangle$	mean square noise at the output of the detector

Publications

Askraba, S., Tran, D and Booth, D.J., 1998, Study of vibration of thin shallow spherical shells by laser pulse excitation and interferometry, IMAC, Santa Barbara, CA, USA.

Askraba, S., 1997, *In situ* measurements of stress variations in thin films, *Proceeding VSA '97, The 4TH Vacuum Society of Australia* pp. P2.1.

Askraba, S. Cussen, L.D and Szajman J. 1996, A novel Technique to Measure Stress in thin metallic films, *Journal of Measurement Science and Technology*, vol. 7, pp. 939-943.

Askraba, S., Cussen, L.D and Szajman J. 1995, A new Technique for Measurement of stress in thin films, *Proceeding VSA '95, The 3RD Vacuum Society of Australia* pp. 13-15.